

THERMODYNAMIC STUDIES OF PHYSISORPTION USING THE LANGMUIR
ADSORPTION MODEL

by

Dalton Lennis William Compton

A dissertation submitted in partial fulfillment
of the requirements for the degree

of

Doctor of Philosophy

in

Chemistry

MONTANA STATE UNIVERSITY
Bozeman, Montana

May 2025

©COPYRIGHT

by

Dalton Lennis William Compton

2025

All Rights Reserved

DEDICATION

I dedicate this work to God, my family, my partner Katy, and my friends.

To my family, every one of you has impacted and guided my life in an unforgettable way. Brad, my father, your unwavering strength, love, and wisdom has shaped me into the man I am today. Lynnea, my mother, your unconditional love and guidance have shown me to always follow my heart and chase my dreams. I know at times I have not been the easiest to teach but I promise I was always listening, and those lessons still resonate with me today. Adam, my brother, you are one of my inspirations with your passion, drive, and willingness to always take chances and live life to the fullest. I know we may butt heads at times, but I know you will always be by my side when I need you and I will always be there for you whenever. I am grateful for all the sacrifices you all have made to support me and give our family the best of life.

To my partner, Katy, your unwavering love, support, and passion has brought an incredible amount of happiness and faith to my life. In this crazy journey we call life, you have been my safe haven by my side supporting me and facing life's challenges head on. I know I can be stubborn and difficult at times, but your unwavering persistence has taught me how to truly open up and be myself. I cannot wait to experience all the crazy adventures that God has in store for us, and I will always remember your love, passion, and faith.

To my friends, I want to say thank you for always being there when I have needed you. Through the good times and the bad we have continued to support and push one another to never give up. I will never forget all the adventures, lessons, and memories that we have made.

Every one of you has played a pivotal role in guiding me and shaping me into the man I am today. I will be forever grateful to all of you for your love, support and guidance that you have given me. This dissertation is dedicated to you all!!!

ACKNOWLEDGEMENTS

I would like to thank first my advisor, Nick Stadie, for his mentorship and guidance over the years. Your passion and curiosity of science continues to push all of us in our group to be the best scientists we can be. You encourage us to explore all our wildest experiments and allow us to work through complications on our own, allowing us to grow both personally and professionally. The true passion you have for gas adsorption and the fundamentals of science is an inspiration to me to strive on my own. Thank you for constantly pushing me to be truthful in all our findings, for taking the road less traveled and the all the lessons you have taught me in my professional life.

I want to thank my committee next, Dr. Rob Walker, Dr. Erik Grumstrup, and Dr. Ryan Anderson, for their support and insight along this journey. Their vast knowledge and guidance were paramount in developing my scientific process and technique.

To all my lab mates, thank you, as we supported each other and pushed each other to new heights and scientific discoveries. We are always there for one another when things may not be going as planned in the lab, but we're able to aid each other and push through the difficulties.

Lastly, I would like to thank my first mentor, Dr. Dale Russell, who truly created and fostered a burning passion for chemistry. You showed me the excitement of analytical chemistry and enlightened me on the true details and discovery of the scientific process. Thank you for teaching me the joys of chemistry and encouraging me to be the scientist I am today.

TABLE OF CONTENTS

1. INTRODUCTION	1
Overview.....	1
Objectives.....	4
Modern Energy Landscape	4
Hydrogen Storage for Clean Energy.....	5
Methane Storage and Energy	12
Summary of Introduction and Energy Sources.....	15
References.....	15
2. ADSORPTION THEORY AND THERMODYNAMICS	18
Physical Adsorption.....	18
Chemical Adsorption.....	21
Gas Adsorption Models.....	21
Langmuir Model	22
Freundlich and Langmuir-Freundlich Model.....	27
Hill Model.....	28
Gibbs Surface Excess.....	28
Adsorption Thermodynamics.....	31
Isosteric Enthalpy of Adsorption.....	31
Isoexcess Enthalpy of Adsorption.....	33
Experimental Adsorption Fitting.....	34
Linear Interpolation.....	36
Generalized Langmuir Fitting.....	37
Adsorption Instrumentation	40
References.....	42
3. THE TEMPERATURE DEPENDENCE OF THE LANGMUIR ADSORPTION MODEL FOR A SINGLE SITE METAL-ORGANIC FRAMEWORK.....	44
Contribution of Authors and Co-Authors.....	44
Manuscript Information	45
Abstract.....	46
Introduction.....	46
Theory	49
Gibbs Excess Adsorption	49
Langmuir Theory	50
Langmuir Pre-Factor.....	51
Experimental Methods.....	54
Materials Synthesis.....	54

TABLE OF CONTENTS CONTINUED

Materials Characterization.....	55
Hydrogen Adsorption Measurements.....	55
Structure Analysis	55
Results and Discussion.....	56
Model System Selection.....	56
Hydrogen Adsorption Uptake	57
Thermodynamic Analysis	60
Average Temperature Isothermic Heat	63
Conclusions.....	66
Associated Content	67
Acknowledgements.....	67
Supporting Information.....	67
Absolute Adsorption Approximation:	67
Clausius-Clapeyron Approximation:.....	68
Powder X-Ray Diffraction Analysis:	68
Cryostat Temperature Calibration:.....	69
Langmuir Adsorption Theory:	70
Adsorption Site Descriptions and A[T]:.....	72
Fixed (i.e., “model -2.5”).....	72
3D Ideal Gas (i.e., “model -1”).....	73
Einstein Adsorbed Phase (i.e., “model +0.5”)	74
2D Ideal Gas with z-Oscillation (i.e., “model -0.5”)	75
Nomenclature:.....	76
Thermal deBroglie Wavelength:	77
References.....	79
4. LIMITS OF LANGMUIR MODELING OF SUPERCRITICAL ADSORPTION EQUILIBRIA: METHANE ON MOF-5 AS A CASE STUDY	81
Contribution of Authors and Co-Authors.....	81
Manuscript Information	82
Abstract.....	83
Introduction.....	83
Theory	86
Experimental Methods.....	89
Materials.....	89
Materials Characterization.....	89
Methane Adsorption Measurements.....	90
Methane Adsorption Modeling.....	90
Structure Analysis	91
Results and Discussion.....	91
Crystalline Adsorbent MOF-5.....	91

TABLE OF CONTENTS CONTINUED

Methane Adsorption on MOF-5.....	93
Supercritical Adsorption Equilibria Fitting.....	95
Fitting Parameter Correlation.....	99
Subcritical Adsorption Equilibria Fitting.....	100
Isosteric Heat of Adsorption	102
Conclusion	106
Associated Content	107
Acknowledgements.....	107
Supporting Information.....	108
Absolute vs. Excess Adsorption:.....	108
Powder X-Ray Diffraction Analysis:	109
Nitrogen Adsorption Analysis:.....	110
Best-Fit Parameters for Supercritical SL-4L Models:	111
Best-Fit Parameters for Subcritical SL Model:	117
Plots of Supercritical Adsorption fitting Experiments:	118
A/E Parameter Correlation Analysis:.....	124
Plots of Subcritical Methane Adsorption Fitting Experiments:	125
References.....	126
5. CONFINEMENT EFFECTS ON ISOSTERIC HEAT OF METHANE ADSORPTION ON POROUS CARBONS	129
Contribution of Authors and Co-Authors.....	129
Manuscript Information	131
Abstract.....	132
Introduction.....	132
Experimental Methods.....	137
Materials Synthesis	137
Materials Characterization.....	137
Adsorption Modelling.....	138
Computational Methods.....	138
Results and Discussions.....	138
Model System Selection.....	138
Methane Adsorption Uptake	140
Isosteric Heat of Adsorption	145
Binding Site Environments.....	147
Mechanisms of Binding.....	150
Conclusions.....	152
Associated Content	153
Acknowledgements.....	153
References.....	153

TABLE OF CONTENTS CONTINUED

6. CONCLUSIONS.....	158
Summary of Discoveries.....	158
Objective 1:.....	158
Objective 2:.....	160
Objective 3:.....	161
Future Work	162
Interactions/Cooperativity in the Langmuir Model	163
Error Analysis of the Fitting Parameters.....	163
Schwartzite as a Methane Storage Material.....	164
References.....	164
REFERENCES CITED.....	166

LIST OF TABLES

Table	Page
1. Table 1. Six important adsorption models explored herein, and their temperature dependence of the pre-exponential factor in the Langmuir constant, high-temperature limit heat capacity, and number of degrees of freedom. Further details are provided in Table S1.....	54
2. Table 2. Best-fit parameters for six models of H ₂ adsorption on Ni ₃ (pzdc) ₂ (ade) ₂ (H ₂ O) ₄ according to SL equations with different T-dependence of the pre-exponential factor, AT	63
3. Table S1. Partition functions and T-dependence of the adsorption equation for single-site Langmuir models of ideal gases, depending on the number and potential form of the external degrees of freedom in the adsorbed state. Abbreviations: DF = delta function, SP = square potential, QP = quadratic potential. Variables in red are fitting constants of the resulting model.....	78
4. Table 1. Summarized properties of CH ₄ adsorption on MOF-5 , per past reports ^{18,19}	93
5. Table 2. Best-fit global Langmuir model parameters for single- (SL) to four- (4L) site Langmuir models of CH ₄ adsorption on MOF-5 under “blind” fitting conditions (where no parameters were fixed).	101
6. Table 3. Best-fit global Langmuir model parameters for a “fixed” four-site Langmuir (4L) model of CH ₄ adsorption on MOF-5 (where $ntot$, $Vmax$, αi , and Ei were fixed).....	102
7. Table S1. Best-fit global Langmuir model parameters for single- (SL) to four- (4L) site Langmuir models of CH ₄ adsorption on MOF-5 under “blind* exp.” fitting conditions (where only $Vmax = 1.47 \text{ mL g}^{-1}$ was fixed).....	111
8. Table S2. Best-fit global Langmuir model parameters for single- (SL) to four- (4L) site Langmuir models of CH ₄ adsorption on MOF-5 under “loose exp.” fitting conditions (where only $nmax = 36.1 \text{ mmol g}^{-1}$ and $Vmax = 1.47 \text{ mL g}^{-1}$ were fixed).....	112
9. Table S3. Best-fit global Langmuir model parameters four-site Langmuir (4L) models of CH ₄ adsorption on MOF-5 under “tight α exp.” (where $nmax$, $Vmax$, and αi were fixed), “tight E exp.” (where $nmax$, $Vmax$, and Ei were fixed), and “fixed exp.” (where $nmax$, $Vmax$, αi , and Ei were fixed) fitting conditions.....	113

LIST OF TABLES CONTINUED

Table	Page
10. Table S4. Best-fit global Langmuir model parameters for single- (SL) to four- (4L) site Langmuir models of CH ₄ adsorption on MOF-5 under “blind* com.” fitting conditions (where only $V_{max} = 1.30 \text{ mL g}^{-1}$ was fixed).....	114
11. Table S5. Best-fit global Langmuir model parameters for single- (SL) to four- (4L) site Langmuir models of CH ₄ adsorption on MOF-5 under “loose com.” fitting conditions (where only $n_{max} = 30.2 \text{ mmol g}^{-1}$ and $V_{max} = 1.30 \text{ mL g}^{-1}$ were fixed).....	115
12. Table S6. Best-fit global Langmuir model parameters four-site Langmuir (4L) models of CH ₄ adsorption on MOF-5 under “tight α com.” (where n_{max} , V_{max} , and α_i were fixed), “tight E com.” (where n_{max} , V_{max} , and E_i were fixed), and “fixed com.” (where n_{max} , V_{max} , α_i , and E_i were fixed) fitting conditions.....	116
13. Table S7. Best-fit global Langmuir model parameters for single- (SL) site Langmuir model of CH ₄ adsorption on MOF-5 under subcritical conditions	117
14. Table 1. Textural properties of the five model materials determined via N ₂ adsorption at 77 K.....	143
15. Table 2. Best-fit parameters for a double-site Langmuir model fit (with a $T^{-1/2}$ temperature dependence of the Langmuir constant) to the five model materials.	144
16. Table 3. Desorption energies (ΔE^{QM}), BSSE-corrected energies (ΔE^{QM*}), BSSE/ZPE-corrected energies (ΔE^{ZPE*}), and standard enthalpies ($\Delta_{des}H^\circ$) for Adsorbent \times nCH ₄ \rightarrow Adsorbent + nCH ₄ calculated using the MN15/6-311++G** level of theory (in units of kJ mol ⁻¹).	148

LIST OF FIGURES

Figure	Page
1. Figure 1: Gravimetric and volumetric energy density of hydrogen compared to traditional fuels. These values are based on the lower heating values of each fuel. ^{6,7}	7
2. Figure 2. Phase diagram of hydrogen (H ₂) calculated using standard reference data. ¹¹ Ambient pressure and temperature lines are highlighted.....	9
3. Figure 3. Components of a commercial high pressure hydrogen storage tank. This figure was adapted from elsewhere. ⁹	10
4. Figure 4. Strategies for hydrogen storage.....	12
5. Figure 5. Phase diagram of methane calculated using standard reference data. ¹¹ Ambient pressure and temperature lines are highlighted.....	14
6. Figure 1. The Lennard-Jones 6-12 potential of a gas molecule on an adsorbent surface, with a binding energy of V_0 and equilibrium binding distance of r_0	20
7. Figure 2. Lennard-Jones potential wells of two independent binding sites opposite one another inside a pore. As the pore size narrows (from a-d), the wells get closer to the unique distance (d) where there is overlap between the individual wells to create one singular well with higher binding energy.....	21
8. Figure 3. Visual representations of the adsorbate's degrees of freedom when in the adsorbed phase, the underlying partition functions, and the temperature dependence of the Langmuir constant. The three spatial partition functions are: delta function (DF), square potential (SP), and quadratic potential (QP). This figure was adapted from elsewhere. ¹⁰	26
9. Figure 4. Representation of absolute and excess adsorption along an adsorption isotherm. The excess (blue), reference (yellow), and absolute (combined, green) adsorbed quantities are shown at five pressures P_1 - P_5 . The bulk fluid (gray) is shown as a crystal to emphasize constant density and geographical location. This figure was adapted from elsewhere. ¹⁹	31
10. Figure 5. Excess methane adsorption on MOF-5 between 243–328 K and 0–100 bar.....	36

LIST OF FIGURES CONTINUED

Figure	Page
11. Figure 6. (a) Linear interpolation of the experimental excess adsorption of methane on MOF-5, and corresponding (b) van't Hoff plot and (c) isoexcess enthalpy of adsorption.....	37
12. Figure 7. (a) . Equilibrium excess uptake (circles) of CH ₄ on MOF-5 between 243-328 K and 0-100 bar, fitted to a double-site Langmuir model. (b) Isostatic enthalpy of adsorption of CH ₄ on MOF-5 between 243-328 K and 0-100 bar based on a double-site Langmuir model.	39
13. Figure 8. (a) Custom high-pressure volumetric Sieverts apparatus used for high-pressure (1-120 bar) adsorption measurements. (b) Commercial high-resolution volumetric Sieverts apparatus used for microstructural properties and low pressure (<1 bar) adsorption measurements.....	41
14. Figure 1. (a-c) Crystal structure of the single-site MOF (Ni ₃ (pzdc) ₂ (ade) ₂ (H ₂ O) ₄) showing the one-dimensional channels in yellow that are perpendicular to the one-dimensional Ni-pzdc-ade chains. (d) N ₂ adsorption/desorption isotherms at ~77 K showing its NLDFT pore size of ~7 Å and BET surface area of 195 m ² g ⁻¹	57
15. Figure 2. Equilibrium excess adsorption uptake of H ₂ on Ni ₃ (pzdc) ₂ (ade) ₂ (H ₂ O) ₄ between 70-100 K and 0-1 bar with: (a) normal and (b) logarithmic pressure axes.....	58
16. Figure 3. Equilibrium excess uptake (circles) of H ₂ on Ni ₃ (pzdc) ₂ (ade) ₂ (H ₂ O) ₄ between 70-100 K and 0-1 bar fitted by a series of SL equations (lines) with varying temperature dependencies: $AT \propto (a) T - 2.5$ to (f) $T0$. Goodness of fit (RMSE) is indicated. Isotherm temperature is indicated by color from red (70 K) to blue (100 K).....	59
17. Figure 4. Isostatic enthalpy of adsorption of H ₂ on Ni ₃ (pzdc) ₂ (ade) ₂ (H ₂ O) ₄ between 70-100 K and 0-1 bar based on a series of SL equations with varying temperature dependencies: $AT \propto (a) T - 2.5$ to (f) $T0$. Isotherm temperature is indicated by color from red (70 K) to blue (100 K).....	65
18. Figure 5. Isostatic enthalpy of adsorption of H ₂ on Ni ₃ (pzdc) ₂ (ade) ₂ (H ₂ O) ₄ at 82 K and 0-1 bar based on a series of SL equations with varying temperature dependencies: $AT \propto T - 2.5$ to $T0$	65

LIST OF FIGURES CONTINUED

Figure	Page
19. Figure S1. XRD pattern of $\text{Ni}_3(\text{pzdc})_2(\text{ade})_2(\text{H}_2\text{O})_4$ and $\text{Ni}_3(\text{pzdc})_2(\text{ade})_2(\text{H}_2\text{O})_4 \cdot 2.18\text{H}_2\text{O}$ compared to a simulated pattern (based on the single-crystal XRD structure of $\text{Ni}_3(\text{pzdc})_2(\text{ade})_2(\text{H}_2\text{O})_4 \cdot 2.18\text{H}_2\text{O}^{[\text{S1}]}$).	69
20. Figure S2. Equilibrium excess adsorption uptake of H_2 on $\text{Ni}_3(\text{pzdc})_2(\text{ade})_2(\text{H}_2\text{O})_4$ in a liquid nitrogen bath (N_2 boils at 75.9 K in Bozeman, Montana) and at the same set-point using a cryostat (75.9 K).....	69
21. Figure 1. Crystal structure of MOF-5 showing (a) two cage types within its repeating 3D checkerboard structure and (b-f) four CH_4 binding sites identified by past neutron diffraction studies: ¹⁸ cup sites are shown in yellow, oxide sites in green, hex sites in teal, and selected cavity sites in dark blue. Zinc is shown in gray, carbon in black, and oxygen in red (hydrogen is omitted for clarity).....	93
22. Figure 2. Equilibrium excess adsorption uptake of CH_4 on MOF-5 between (a-b) 243-328 K and 0-100 bar and (c-d) 95-112 K and 0-1 bar.	95
23. Figure 3. Equilibrium excess uptake (circles) of CH_4 on MOF-5 between 243-328 K and 0-100 bar fitted to a series of “blind” Langmuir models (lines) with varying complexity: (a) SL, (b) 2L, (c) 3L, and (d) 4L. For comparison, representative fits to (e) a more constrained “loose” 3L model and (f) a “fixed” 4L model are shown. Goodness of fit (RMSE) is indicated.	98
24. Figure 4. Isothermic heat of adsorption of CH_4 on MOF-5 between 243-328 K and 0-100 bar based on a series of “blind” Langmuir models with varying complexity: (a) SL, (b) 2L, (c) 3L, and (d) 4L. For comparison, the same results based on (e) a more constrained “loose” 3L model and (f) a “fixed” 4L model are shown. Temperature is indicated by color from 243 K (blue) to 328 K (yellow).....	105
25. Figure 5. Isothermic heat of adsorption of CH_4 on MOF-5 at 279 K and 0-100 bar based on all fitting experiments in this study. Model type and fitting method are indicated by color.....	106
26. Figure S1. XRD pattern of MOF-5 powder studied in this work compared to a simulated pattern.	109
27. Figure S2. Equilibrium N_2 adsorption/desorption isotherms at ~77 K and the corresponding NLDFT pore size distribution.	110

LIST OF FIGURES CONTINUED

Figure	Page
28. Figure S3. Equilibrium excess uptake (circles) of CH ₄ on MOF-5 between 243-328 K and 0-100 bar fitted by a series of “blind* exp.” ($V_{max} = 1.47 \text{ mmol g}^{-1}$) Langmuir models (lines) with varying complexity: (a) SL, (b) 2L, (c) 3L, and (d) 4L.....	118
29. Figure S4. Equilibrium excess uptake (circles) of CH ₄ on MOF-5 between 243-328 K and 0-100 bar fitted by a series of “loose exp.” ($n_{max} = 36.1 \text{ mmol g}^{-1}$ and $V_{max} = 1.47 \text{ mmol g}^{-1}$) Langmuir models (lines) with varying complexity: (a) SL, (b) 2L, (c) 3L, and (d) 4L.....	119
30. Figure S5. Equilibrium excess uptake (circles) of CH ₄ on MOF-5 between 243-328 K and 0-100 bar fitted by a series of (a) “tight α exp.” (where n_{max} , V_{max} , and α_i were fixed), (b) “tight E exp.” (where n_{max} , V_{max} , and E_i were fixed), and (c) “fixed exp.” (where n_{max} , V_{max} , α_i , and E_i were fixed).	120
31. Figure S6. Equilibrium excess uptake (circles) of CH ₄ on MOF-5 between 243-328 K and 0-100 bar fitted by a series of “blind* com.” ($V_{max} = 1.30 \text{ mmol g}^{-1}$) Langmuir models (lines) with varying complexity: (a) SL, (b) 2L, (c) 3L, and (d) 4L.....	121
32. Figure S7. Equilibrium excess uptake (circles) of CH ₄ on MOF-5 between 243-328 K and 0-100 bar fitted by a series of “loose com.” ($n_{max} = 31.2 \text{ mmol g}^{-1}$ and $V_{max} = 1.30 \text{ mmol g}^{-1}$) Langmuir models (lines) with varying complexity: (a) SL, (b) 2L, (c) 3L, and (d) 4L.	122
33. Figure S8. Equilibrium excess uptake (circles) of CH ₄ on MOF-5 between 243-328 K and 0-100 bar fitted by a series of (a) “tight α com.” (where n_{max} , V_{max} , and α_i were fixed), (b) “tight E com.” (where n_{max} , V_{max} , and E_i were fixed), and (c) “fixed com.” (where n_{max} , V_{max} , α_i , and E_i were fixed).	123
34. Figure S9. Isothermic heat of adsorption of CH ₄ on MOF-5 at 279 K and 0-100 bar based on all fitting experiments in this study (where $n_{max} = 31.2 \text{ mmol g}^{-1}$ and $V_{max} = 1.30 \text{ mmol g}^{-1}$). Model type and fitting method are indicated by color.....	123

LIST OF FIGURES CONTINUED

Figure	Page
35. Figure S10. Logarithmic correlation between A_i and E_i of all the Langmuir fits from both computational set values and experimental set values. Points in grey have been omitted from the correlation fit due to them being deemed outliers by visual inspection.....	124
36. Figure S11. Equilibrium excess uptake (circles) of CH_4 on MOF-5 between 95-112 K and 0-0.01 bar globally fitted by a single-site Langmuir model with a temperature dependence of $T^{-0.5}$ (lines).....	125
37. Figure S12. Equilibrium excess uptake (circles) of CH_4 on MOF-5 between 95-112 K and 0-0.01 bar compared to extrapolated 4L “blind fit” of the supercritical equilibria (lines).	125
38. Figure 1. Materials characterization of five model porous materials: pDCX, PAF-1, MSC-30, GMS, and ZTC. (a-e) Primary structural units, (f) XRD patterns, and (g) N_2 -accessible pore-size distribution.....	142
39. Figure 2. Equilibrium excess uptake (circles) of CH_4 on (a) pDCX, (b) PAF-1, (c) MSC-30, (d) GMS, and (e) ZTC between 238-328 K up to 10 MPa, fitted by a double-site Langmuir model. (f) Comparison of all materials at 298 K.	143
40. Figure 3. Isothermic enthalpy of CH_4 adsorption on (a) pDCX, (b) PAF-1, (c) MSC-30, (d) GMS, and (e) ZTC between 238-328 K and up to 10 MPa. (f) Comparison of all materials at 298 K.	146
41. Figure 4. Binding structures and energies of 1L, 2L, and 3L adsorption interactions on flat, open carbon surfaces of increasing ring number: (a) benzene, (b) naphthalene, and (c) methyldene phenalene (MPh), respectively. The level of theory is MN15/6-311++G** and the BSSE- and ZPE-corrected SCF energy difference upon dissociation is indicated ($\Delta_{\text{des}}H^\circ$). Carbon is shown in black, hydrogen in white, and ring centroid interactions (as a guide to the eye) in yellow.....	148
42. Figure 5. Binding structures and energies of 2L–2L, 3L–MMA–3L, and 3L–MMS–3L adsorption interactions in optimized scenarios: (a) within a single-width slit pore, (b) within a double-width slit pore, and (c) on an open surface, respectively. The level of theory is MN15/6-311++G** and the standard enthalpy difference upon dissociation is indicated ($\Delta_{\text{des}}H^\circ$). Carbon is shown in black, hydrogen in white, ring centroid interactions (as a guide to the eye) in yellow, and methane–methane interactions (as a guide to the eye) in green/red.....	150

ABSTRACT

The simplest possible physical models of adsorption were developed by Irving Langmuir and provides a foundational framework for understanding gas adsorption on adsorbent surfaces. These models are extensively used to fit adsorption equilibria (experimental and computational) in order to discover thermodynamic and physical properties of the adsorption system. Even with the simplest variant, the single-site Langmuir model, these models can accurately describe a vast range of different adsorbate gases and adsorbents, but there is still the question of how meaningful the resulting physical and thermodynamic properties are. The Langmuir models can be elegantly derived using first-principles statistical mechanics where one can account for the individual degrees of freedom in the adsorbed phase. As the gas adsorbate transitions from the free bulk phase to the adsorbed phase at a binding site, it can have different degrees of freedom, leading to different temperature dependencies of the Langmuir constant. To assess which description is experimentally validated, we measured hydrogen adsorption equilibria on $[\text{Ni}_3(\text{pzdc})_2(\text{ade})_2(\text{H}_2\text{O})_4]$ and fit them to a wide array of single-site Langmuir models. Interestingly, all of the models were found to be validated, but the average temperature isosteric enthalpy of adsorption was determined to be a reliable common metric among them. In a second study, methane adsorption was measured on MOF-5, a more complicated system with four different binding sites spanning a wide range of binding energies. In this work, we fit the measured adsorption equilibria to a wide array of multi-site Langmuir models to determine the binding energy of the four different binding sites using only experimental methane adsorption equilibria. These results show the important limits of this method, especially at supercritical conditions. Lastly, methane adsorption was measured on a set of five model porous carbons to determine the effects of confinement and binding site environments on the isosteric enthalpy of adsorption. The comparison between zeolite-templated carbon and graphene mesosponge is emphasized, highlighting that the increasing isosteric enthalpy of adsorption in zeolite templated carbon is due to uniform confinement and the presence of three-ring binding sites.

CHAPTER ONE

INTRODUCTION

Overview

The investigations detailed in this dissertation address fundamental aspects of the Langmuir adsorption model, the simplest possible model of gas-solid adsorption phenomena. These investigations aim to provide a better understanding of the limits on and guiding principles of adsorptive hydrogen and methane storage on porous materials. The primary focus of the early investigations is focused on critically evaluating Langmuir adsorption modeling as a tool for understanding real-world adsorption systems. Additionally, they seek to better elucidate how the specific Langmuir models and their individual sub-variants affect the structural and thermodynamic properties extracted from the analysis. The last investigation details the effect of adsorption site environments and confinement on gas adsorption thermodynamics in practical systems of interest for methane capture, storage, and delivery.

A variety of adsorption models and modelling methods are described throughout adsorption literature. The resulting physical and thermodynamic properties obtained from such analyses are heavily reliant on the model and method used, leading to a disparity in outcomes in the literature. This causes complications when reporting “record” materials as well as gives misleading guidance for developing new gas capture/storage materials. Our primary goal is to show the drawbacks and limitations of different modeling practices and provide a guide to best practices in modeling experimental adsorption measurements. Chapter 1 presents the key

objectives of this work and provides an overview of the past and present state of hydrogen and methane storage.

Chapter 2 establishes the need for a fundamental and critical analysis of adsorption modeling and the implications of specific practices. The single-site Langmuir adsorption model is systematically derived using first-principles statistical mechanics while varying the degrees of freedom of the binding site. The derivation of the enthalpy of adsorption is also shown, along with modelling of supercritical gas adsorption equilibria using different approaches. The resulting isosteric and isoexcess enthalpy of adsorption, key thermodynamic metrics of adsorption systems, are demonstrated and compared. Lastly, the instrumentation used to measure adsorption equilibria is described.

Chapter 3 describes a methodological study of the temperature dependence of the Langmuir constant in the Langmuir adsorption model, using hydrogen adsorption on a model single-site metal-organic framework (MOF). Hydrogen (H_2) is an ideal candidate adsorbate for this investigation, as it is one of the weakest interacting molecular adsorbates, effecting only a minimal perturbation to the porous adsorbent's structure. A set of carefully measured hydrogen adsorption isotherms was fitted to a series of Langmuir models with a systematically varied temperature dependence of the Langmuir constant. The effects on the deduced binding energy and isosteric enthalpy of adsorption are discussed. The main outcome of this work is that the binding energy could not be determined unambiguously, but the average temperature isosteric enthalpy of adsorption was found to be a robust deliverable across all methods used.

Chapter 4 builds on these findings and turns to methane (CH_4) adsorption on a more complex MOF with four well-known binding sites. Supercritical and subcritical methane

adsorption isotherms were measured and fitted to a series of site-specific (single-site to four-site) Langmuir models. The resulting best-fit parameters from each model were then compared to previously established experimental and computational results. The limitations of the Langmuir adsorption model in accurately identifying these different binding site energies and the isosteric enthalpy of adsorption were thoroughly explored. Similar to the findings presented in Chapter 3, the isosteric enthalpy was found to be a robust deliverable across all methods employed.

Chapter 5 reports on the culmination of studies of supercritical methane adsorption on a series of five model porous carbons with complementary properties. The five materials investigated were: a porous organic polymer (p-DCX), a porous aromatic framework (PAF-1), an activated carbon (MSC-30), graphene mesosponge (GMS), and zeolite-templated carbon (ZTC). These materials have systematically different chemical environments based on one-ring or three-ring moieties, permitting isolation of the effects of binding site type, homogeneity, and confinement on the isosteric enthalpy of adsorption. Pairing these experimental isotherms with a series of computational results provides new insights into methane-carbon interactions, and the results yielded new guidelines for optimal materials design to increase methane storage performance.

Chapter 6 integrates these studies as a cohesive body of work, highlighting the connections between and motivations behind each distinct hypothesis. We also suggest future experiments that can provide further insight into gas-solid adsorption modeling and propose how these results could guide future endeavors to design and study adsorptive energy storage materials.

Objectives

Our objectives for this work are to:

1. determine the temperature dependence of the Langmuir constant of the single-site Langmuir model and its effects on the isosteric enthalpy of adsorption.
2. use the Langmuir model to accurately predict the number of site types and corresponding binding energies on a crystalline multi-site material.
3. use the insights gained above to provide guidelines for methane adsorption on porous carbons (a system of high interest for practical energy storage applications) with a complex landscape of binding environments.

These objectives are addressed by collecting and systematically analyzing a multitude of gas adsorption isotherms on porous carbons and MOFs, and will be critically reviewed in Chapter 6. Our fundamental curiosity about adsorption mechanisms has driven us to find model materials that provide a deeper understanding of adsorption phenomena and offer insights into future materials design. When choosing model materials, we considered a range of variables, including crystallinity, particle size, pore size, binding site geometry and chemistry, total number of binding sites, and material purity.

Nitrogen (N_2) adsorption is the primary characterization technique for determining the textural and structural properties of porous materials because it is a small probe molecule with an easily available and safe liquid bath at ambient pressure (making the measurement of subcritical adsorption very routine). It is used to determine the pore-size distribution, surface area, total pore volume, and overall quality of the material (by comparison of these properties to known or expected values). X-ray diffraction (XRD) was used to reveal and verify the underlying crystal

structure of the materials, providing the unit cell size, crystallite size, and phase purity. Jolting volumetry was used to compact loose powder samples to determine the true bulk density of adsorbent powders for calculating the volumetrics of adsorption uptake. High-pressure gas adsorption (typically H_2 and CH_4) was measured to reveal the thermodynamics and upper limits of gas storage under temperatures of interest for applications. Finally, the measured adsorption equilibria were analyzed using a custom Python package (Realist, v.0.314¹) to determine best fits to each model explored. The information accumulated from these characterization techniques provided the basis for all new insights into modeling gas adsorption equilibria and subsequent guidelines for methane storage on porous carbons reported herein.

Modern Energy Landscape

The continual evolution of society has led to a growing demand for energy, driving the need for abundant, energy-dense fuels. The appetite for these fuels presents many challenges, such as occasional catastrophic failure of storage and handling methods well as the diminishing quantities of traditional fuels. Over the past 125 years, the Earth's global temperature has risen by about 1.1°C due to the burning of fossil fuels by humans, leading to a recent push toward the use of cleaner fuels.² Currently, approximately 85% of the world's energy consumption is met by burning fossil fuels: 23%, 26%, and 32% from natural gas, coal, and oil, respectively.³ The extraction and burning of these fossil fuels have contributed to major environmental impacts across the world. Waterways, land, and air are being polluted (e.g., by SO_x and NO_x emissions), and the climate is subjected to warming by the emission of greenhouse gases (e.g., CO_2 and CH_4). There are alternative methods to generate useful energy apart from burning traditional fuels, such as by harnessing wind, nuclear, solar, or hydrothermal generation methods. These alternative energy

systems provide opportunities to mitigate the current climate crisis without being reliant on a single energy carrier but still require further research to facilitate the transition.

Discussions on alternative fuels are primarily focused on changing the method of energy production on a large scale (e.g., at the city or state level); fewer address how to meet mobile energy demands from vehicles/transportation. About a quarter of the world's total CO₂ emissions come from the burning of mobile energy fuels, with approximately 75% of those CO₂ emissions coming from road vehicles (passenger and freight vehicles).⁴ There is a global need to identify new fuels, advance the knowledge of renewable energy sources, and transition away from gasoline and diesel to cleaner and more efficient mobility fuels. In this work, we focus on the two mobility fuels of greatest interest: hydrogen and methane, both of which can be significantly densified for storage via adsorption. We take a deeper look at the thermodynamics of adsorption for hydrogen and methane and how we can use this knowledge to improve the development and implementation of cleaner fuels for mobility applications.

Hydrogen Storage for Clean Energy

There has been significant interest over recent decades in finding suitable alternative energy carriers to traditional fuels (especially petroleum-based liquids and coal).⁵ Hydrogen is an ideal candidate to replace these traditional fuels since it has the highest gravimetric energy density of any chemical fuel (shown in Figure 1), and its combustion does not produce carbon dioxide. The chemical energy stored within molecular hydrogen (H₂) can be effectively converted into mechanical energy or electrical energy through combustion within an engine or oxidation within a fuel cell.

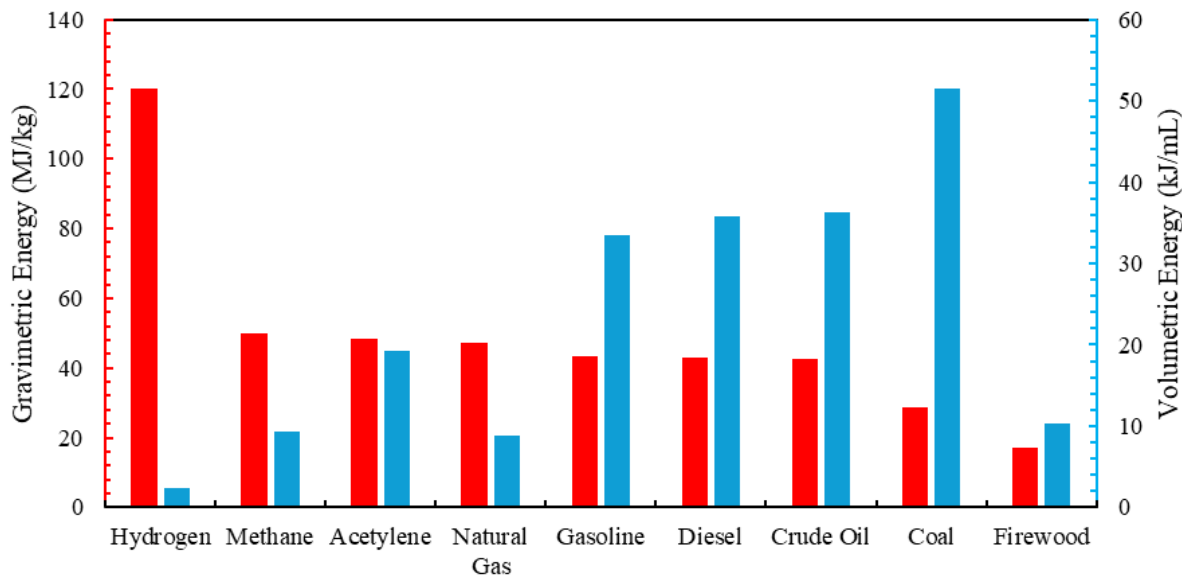


Figure 1: Gravimetric and volumetric energy density of hydrogen compared to traditional fuels. These values are based on the lower heating values of each fuel.^{6,7}

Unfortunately, hydrogen exhibits one of the lowest volumetric energy densities among chemical fuels, due to the low density of even compressed forms (hydrogen is a gas at ambient conditions). Owing to the weak van der Waals forces between hydrogen molecules, liquefaction occurs only at very low temperatures (Figure 2), necessitating the use of very high pressures to achieve reasonable densities for storage. Interestingly, there is more hydrogen per volume in gasoline or water at standard temperature and pressure (STP) than in pure liquid hydrogen at 20 K.¹² Most conventional fuels used for transportation purposes are either liquids (e.g., gasoline) or compressed gases (e.g., propane) with boiling points near ambient temperature.

High pressures or cryogenic temperatures are generally required for hydrogen storage in transportation applications; however, due to safety and cost challenges associated with cryogenic

storage, high-pressure tanks are the preferred method.⁸ The state-of-the-art compression cylinders are primarily constructed from a metal or plastic inner liner that is fully wrapped with carbon fiber or a composite material^{8,9} (Figure 3). With approximately 16,500 motor vehicle accidents occurring daily in the United States, hydrogen storage cylinders must be capable of withstanding the forces from vehicular impacts. Multiple production pathways exist for synthesizing hydrogen, such as electrolysis of water or reforming natural gas into hydrogen and carbon dioxide.¹⁰ These methods have markedly different amounts carbon emissions associated with them, and carbon-reduced routes are also possible depending on the handling of emitted CO₂ following production (e.g., by combining carbon capture with steam reforming).

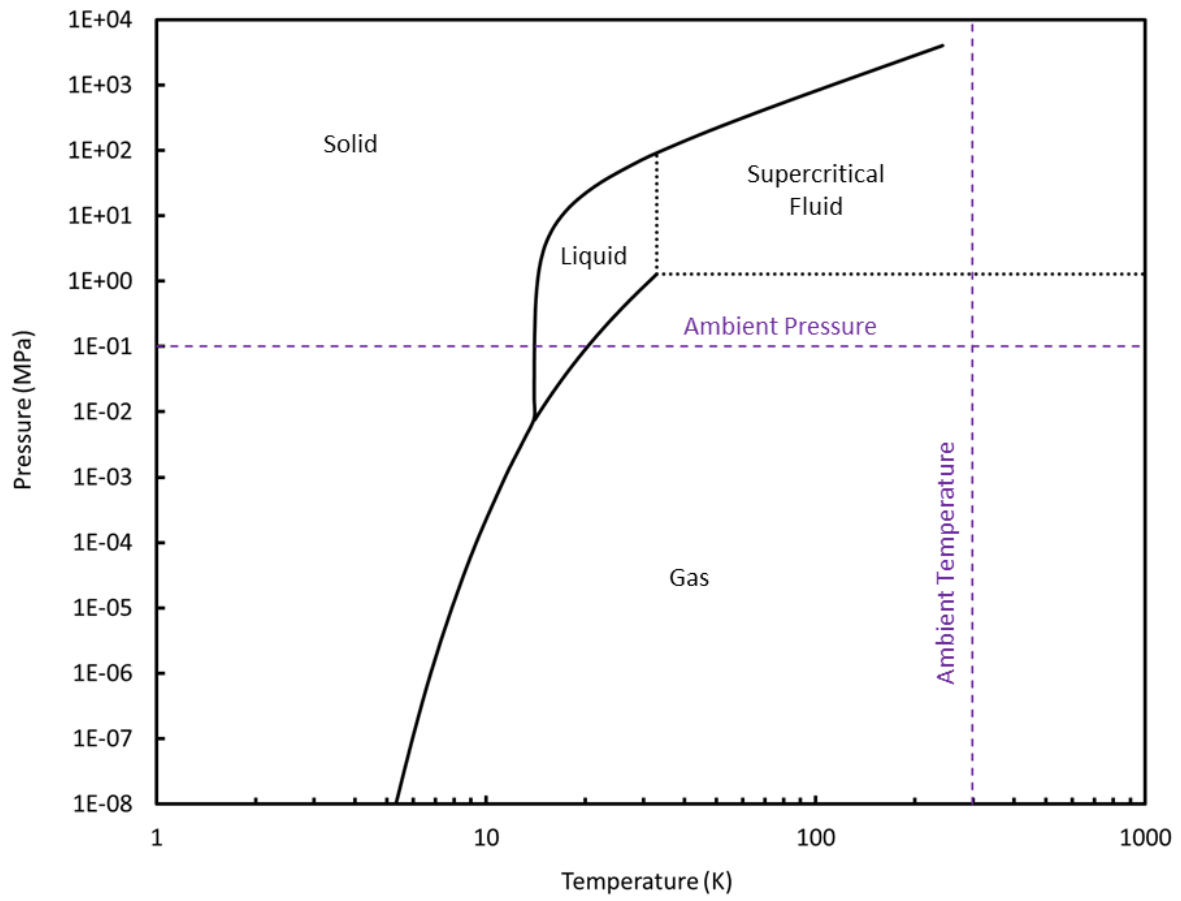


Figure 2. Phase diagram of hydrogen (H_2) calculated using standard reference data.¹¹ Ambient pressure and temperature lines are highlighted.

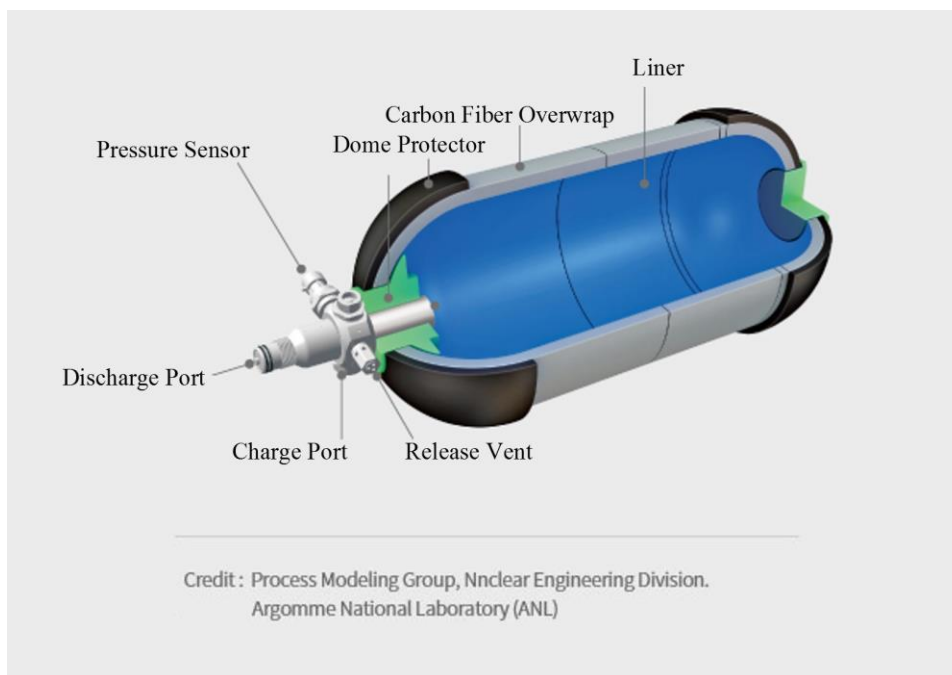
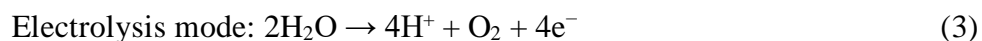


Figure 3. Components of a commercial high pressure hydrogen storage tank. This figure was adapted from elsewhere.⁹

Nevertheless, due to its exceptionally high gravimetric energy density, hydrogen has attracted a lot of interest as a renewable, clean fuel for large grid-scale backup energy systems and as an ultimate final step in the transition away from traditional fossil fuels. Reversible fuel cells, novel adsorbent materials, and metal hydrides have been extensively studied to improve the viability of hydrogen as an alternative fuel. In particular, reversible fuel cells have been investigated as potential backup systems to large installations of renewable energy systems (solar- and wind-based) which are subject to fluctuations in energy output.¹³ A reversible fuel cell operates in two modes to recycle the hydrogen and water produced:



In addition to simple compression and liquefaction, hydrogen can be stored using various materials, which are classified into two main categories: absorbents and adsorbents. A summary of different forms of hydrogen storage is shown in Figure 4. Gas absorption occurs when the bulk gas molecules penetrate beyond an interface, leading to the formation of interstitial or chemical hydride bonds. Metal hydrides have shown reversible gas absorption at ambient temperature; however, these materials typically exhibit low gravimetric uptake capacity (despite often densifying hydrogen in more compact arrangements than even solid hydrogen) and slow kinetics. In contrast, chemical or complex hydrides can offer high gravimetric storage capacities but require elevated temperatures and/or pressures to achieve reversibility.¹⁴ To date, the ideal absorptive material that has a high storage capacity and reversibility at near ambient conditions has yet to be discovered.

Adsorption is defined as the favorable interaction of an adsorbate (e.g., a gas) and an adsorbent surface (e.g., a porous carbon), driven by van der Waals forces between the two. This interaction results in the densification of the adsorbate into a film-like phase on the surface of the adsorbent, with a density approaching that of the pure liquid. Unlike absorption, which involves dissociation and bulk diffusion, hydrogen adsorption is purely a surface phenomenon that can occur through either a dissociative mechanism (i.e., chemisorption) or a non-dissociative mechanism (i.e., pure physisorption). As a surface interaction, adsorption capacity is highly dependent on the porous topology, chemical composition, and proximity of the binding sites within the material. Current adsorbents include but are not limited to metal-organic frameworks (MOFs), covalent-organic frameworks (COFs), zeolites, and porous carbonaceous materials. Carbonaceous materials and COFs are particularly attractive adsorbents due to their lightweight

nature, comprised of highly abundant elements, straightforward synthesis, and the tunability of their pore sizes and topologies.^{15,16} MOFs are desirable for their tunability in chemical composition, high crystallinity, high density, and highly ordered porous networks that can be designed a priori.¹⁷ Currently, the leading materials for volumetric hydrogen uptake are MOFs: MOF-5¹⁸ (at low temperatures, and under temperature-pressure swing conditions) and $\text{Ni}_2(\text{m-dobdc})$ ¹⁹ (at ambient temperature).

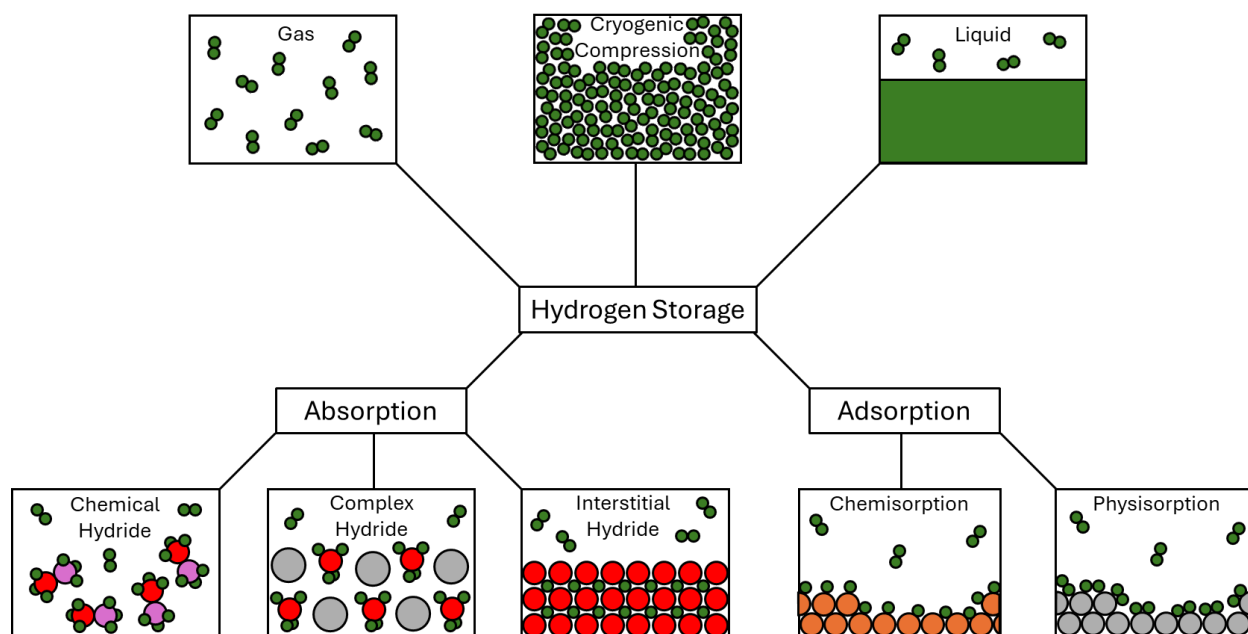
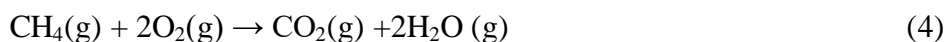


Figure 4. Strategies for hydrogen storage.

Methane Storage and Energy

While hydrogen is considered the ideal mobility fuel from the perspective of carbon emissions, its implementation is not without significant challenges. Until hydrogen can be produced renewably and economically, alternative fuels are needed as transitional solutions to reduce the dependence on traditional fuels. Natural gas, composed of primarily methane (~95%),

stands as the primary candidate fuel after hydrogen for mobility applications.²⁰ The combustion of natural gas produces less greenhouse gases, particulate matter, and toxic byproducts per unit energy than petroleum-based liquids or coal. Methane can be produced from both natural and renewable sources, referred to as biomethane or biogas, offering a more cost-effective solution than the synthesis of long-chain hydrocarbon fuels.²¹ Additionally, natural gas is an abundant natural resource in North America.²¹ Methane also boasts a higher gravimetric energy density⁶ (50 MJ kg⁻¹) than either diesel or gasoline and generates less CO₂ per unit energy due to its molecular structure:



Methane exhibits distinct advantages in terms of its storage compared to hydrogen, as reflected by the differences in their phase diagrams (Figure 5). Methane liquefies at 111 K under ambient pressure; however, storage of natural gas as a liquid (referred to as LNG) is still too energy-intensive for mobility uses. Instead, compressed natural gas (CNG) vehicles are currently commercially available. Similarly to hydrogen, methane has a lower volumetric energy density than gasoline or diesel, resulting in CNG vehicles having a shorter driving range. In most cases, the required storage tanks required occupy a significant portion of the vehicle's usable space, posing additional design and efficiency challenges.

Adsorbed natural gas (ANG) offers a promising approach to achieving liquid-like methane densities by exploiting adsorbed methane on the surface of a porous material. This method results in high methane densities at temperatures higher than LNG and at pressures lower than CNG. Porous carbon materials have shown modest methane uptake advantages over pure compression; however, their low packing densities and limited structural tunability has

historically limited their practical applications. MOFs currently hold the records for the highest volumetric uptake of methane: e.g., HKUST-1²², HKUST-1 monoliths²³, and Ni-MOF-74²².

Despite these records, the practical applications of MOFs as natural gas storage media are limited due to their poor chemical and mechanical stability. The metal oxo- or nitrido- nodes within MOF frameworks create hydrophilic sites that, upon exposure to water (present in most natural gas streams), can become deactivated or lead to the decomposition of the structure.

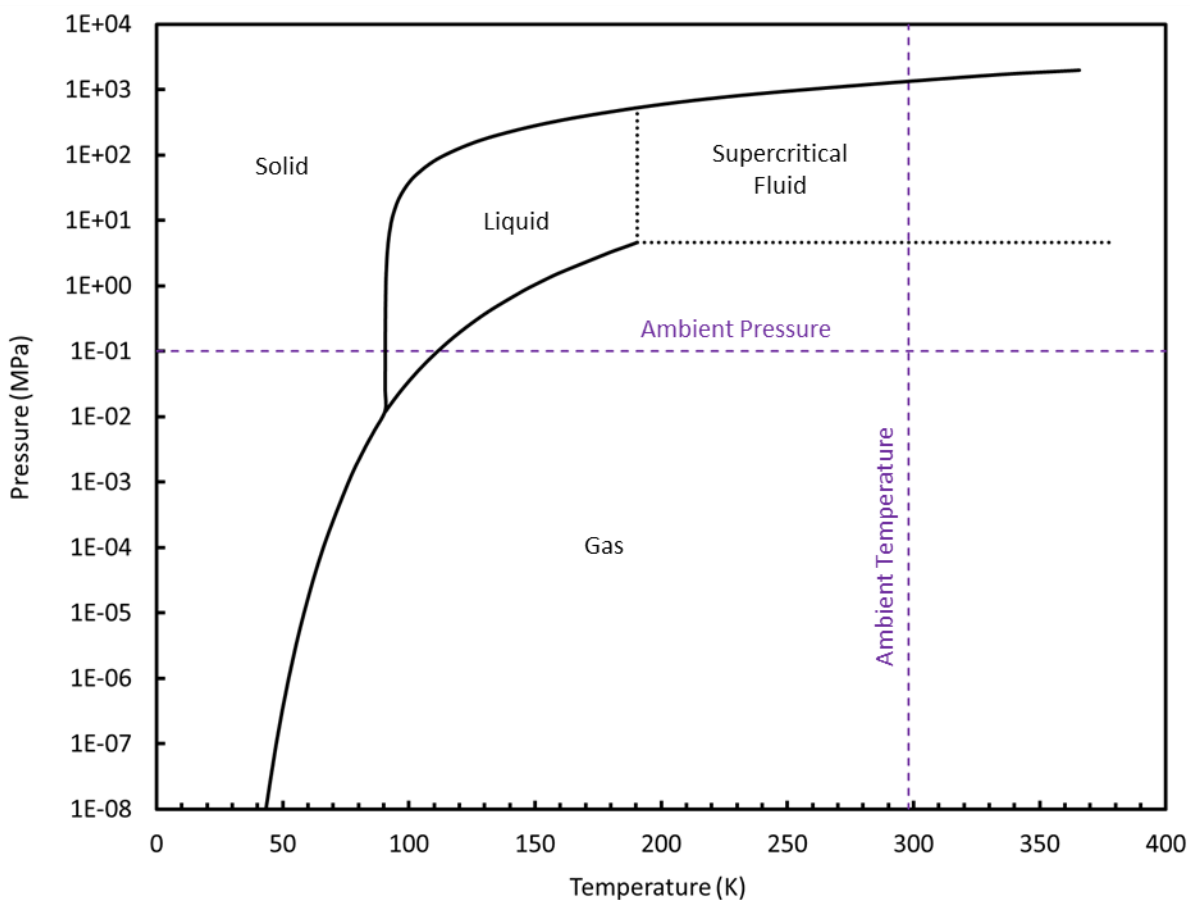


Figure 5. Phase diagram of methane calculated using standard reference data.¹¹ Ambient pressure and temperature lines are highlighted.

Summary of Introduction and Energy Sources

Hydrogen and methane are widely regarded as important mobility fuels; however, their relatively low energy densities compared to traditional fuels present significant challenges. By using well-designed porous materials that leverage favorable adsorption interactions, it is possible to replace traditional fuels (e.g., coal and liquid hydrocarbons) with cleaner alternatives in storage applications. However, despite extensive research, the “golden ticket” adsorbent for hydrogen and methane remains elusive within the adsorption community. Through the careful measurement and modeling of experimental adsorption isotherms, a more comprehensive understanding of the storage capacities and thermodynamic properties of materials can be achieved. This thesis investigates the fundamentals of Langmuir adsorption theory, and uses a rigorous fitting methodology to analyze hydrogen and methane adsorption on model materials. The objective of these efforts is to establish clear guidelines for advancing adsorptive energy storage techniques toward practical implementation.

References

- (1) Quine, C. M. REal Adsorption Langmuir Isotherms for Sorption Theory: REALIST. *Github*. <https://github.com/cullenmq/REALIST> (accessed 2025-03-30).
- (2) Tollefson, J. IPCC Climate Report: Earth Is Warmer Than It’s Been in 125,000 Years. *Nature* **2021**, 596 (7871), 171–172.
- (3) Our World in Data. *Energy consumption by source, World*, 2024. <https://ourworldindata.org/grapher/energy-consumption-by-source-and-country> (accessed 2025-03-01).
- (4) Our World in Data. *Cars, planes, trains: where do CO2 emissions from transport come from?*, 2020 <https://ourworldindata.org/co2-emissions-from-transport> (accessed 2025-03-01).

- (5) *IPCC wraps up its most in-depth assessment of climate change*. CarbonBrief 2023. <https://www.carbonbrief.org/qa-ipcc-wraps-up-its-most-in-depth-assessment-of-climate-change/> (accessed 2025-03-01).
- (6) Demirbas, A. Effects of Moisture and Hydrogen Content on the Heating Value of Fuels. *Energy Sources, Part A* **2007**, 29 (7), 649-655. DOI: 10.1080/009083190957801.
- (7) *NIST Chemistry WebBook*; National Institute of Standards and Technology. <https://webbook.nist.gov/chemistry/> (accessed 04/19/25).
- (8) Xie, Z.; Jin, Q.; Su, G.; Lu, W. A Review of Hydrogen Storage and Transportation: Progresses and Challenges. *Energies* **2024**, 17 (16), 4070. DOI: 10.3390/en17164070.
- (9) Doosan Mobility. *Hydrogen Tank*. <https://www.doosanmobility.com/en/products/hydrogen-tank> (accessed 2024-11-18).
- (10) *Hydrogen decarbonization pathways A life-cycle assessment*; Hydrogen Council, 2021. https://hydrogencouncil.com/wp-content/uploads/2021/01/Hydrogen-Council-Report_Decarbonization-Pathways_Part-1-Lifecycle-Assessment.pdf.
- (11) Lemmon, E.; Huber, M.; McLinden, M. *NIST Standard Reference Database 23: Reference Fluid Thermodynamic and Transport Properties-REFPROP, Version 9.1*; National Institute of Standards and Technology, 2013. <https://www.nist.gov/publications/nist-standard-reference-database-23-reference-fluid-thermodynamic-and-transport>.
- (12) Stadie, N. P. Synthesis and Thermodynamic Studies of Physisorptive Energy Storage Materials. Ph.D. Dissertation, California Institute of Technology, Pasadena CA, 2013. <http://thesis.library.caltech.edu/7198/>.
- (13) Mayyas, A.; Wei, M.; Levis, G. Hydrogen as a long-term, large-scale energy storage solution when coupled with renewable energy sources or grids with dynamic electricity pricing schemes. *Int. J. Hydrogen Energy* **2020**, 45 (33), 16311-16325. DOI: 10.1016/j.ijhydene.2020.04.163.
- (14) Rusman, N.A.A.; Dahari, M. A review on the current progress of metal hydrides material for solid-state hydrogen storage applications. *Int. J. Hydrogen Energy* **2016**, 41 (28), 12108-12126. DOI: 10.1016/j.ijhydene.2016.05.244.
- (15) Panella, B.; Hirscher, M.; Roth, S. Hydrogen adsorption in different carbon nanostructures. *Carbon* **2005**, 43 (10), 2209-2214. DOI: 10.1016/j.carbon.2005.03.037.
- (16) Klontzas, E.; Tylanakis, E.; Froudakis, G. E. Designing 3D COFs with Enhanced Hydrogen Storage Capacity. *Nano Lett.* **2010**, 10 (2), 452-454. DOI:10.1021/nl903068a.

- (17) Ahmed, A.; Liu, Y.; Purewal, J.; Tran, L. D.; Wong-Foy, A. G.; Veenstra, M.; Matzger, A. J.; Siegel, D. J. Balancing gravimetric and volumetric hydrogen density in MOFs. *Energy Environ. Sci.* **2017**, *11*, 2459-2471. DOI: 10.1039/C7EE02477K.
- (18) Ahmed, A.; Seth, S.; Purewal, J.; Wong-Foy, A. G.; Veenstra, M.; Matzger, A. J.; Siegel, D. J. Exceptional hydrogen storage achieved by screening nearly half a million metal-organic frameworks. *Nat. Commun.* **2019**, *10*, 1568. DOI: 10.1038/s41467-019-09365-w.
- (19) Kapelewski, M. T.; Runcevski, T.; Tarver, J. D.; Jiang, H. Z. H.; Hurst, K. E.; Parilla, P. A.; Ayala, A.; Gennett, T.; FitzGerald, S. A.; Brown, C. M.; et al. Record Hydrogen Storage Capacity in the Metal-Organic Framework Ni₂(m-dobdc) at Near-Ambient Temperatures. *Chem. Mater.* **2018**, *30* (22), 8179-8189. DOI: 10.1021/acs.chemmater.8b03276.
- (20) Faramawy, S.; Zaki, T.; Sakr, A. A-E. Natural gas Origin, composition, and processing: A review. *J. Nat. Gas Sci. Eng.* **2016**, *34*, 34-54. DOI: 10.1016/j.jngse.2016.06.030
- (21) Memetova, A.; Tyagi, I.; Karri, R. R.; Kumar, V.; Tyagi, K.; Suhas; Memetov, N.; Zelenin, A.; Pasko, T.; Gerasimova, A; et. al. Porous carbon-based material as a sustainable alternative for the storage of natural gas (methane) and biogas (biomethane): A review. *Chem. Eng. J.* **2022**, *446* (4), 137373. DOI: 10.1016/j.cej.2022.137373.
- (22) Peng, Y.; Krungleviciute, V.; Eryazici, I.; Hupp, J. T.; Farha, O. K.; Yildirim, T. Methane Storage in Metal-Organic Frameworks: Current Records, Surprise Findings, and Challenges. *J. Am. Chem. Soc.* **2013**, *135* (32), 11887-11894. DOI: 10.1021/ja4045289.
- (23) Tian, T; Zeng, Z.; Vulpe, D.; Casco, M. E. Divitini, G.; Midgley, P. A. Silvestre-Albero, J.; Tan, J-C.; Moghadam, P. Z.; Fairen-Jimenez, D. A sol-gel monolithic metal-organic framework with enhanced methane uptake. *Nature Mater.* **2018** , *17*, 174-179. DOI: 10.1038/nmat5050.

CHAPTER TWO

ADSORPTION THEORY AND THERMODYNAMICS

Physical Adsorption

Adsorption occurs when a molecule (an adsorbate) approaches another substance (an adsorbent) at the surface, resulting in a favorable interaction. These interactions lower the Gibbs free energy relative to the bulk phase, indicating that adsorption is an exothermic and spontaneous process. During adsorption, the adsorbate leaves the free bulk phase and transitions into a newly formed adsorbed phase that exists in equilibrium with the surface of the adsorbent. In the case of physical adsorption (physisorption), gas molecules interact with the adsorbent surface through weak London dispersion forces, driven by random fluctuations in electron density. Physisorption does not chemically alter the adsorbate or the adsorbent, leaving their fundamental bonding arrangements unchanged. At equilibrium, adsorbate molecules continuously adsorb and desorb from the surface at equal rates, resulting in constant macroscopic system properties. The kinetics of this process depend on the distinct physical properties of the adsorbent and the energy of the bulk gas phase. As a purely surface phenomenon, adsorption is inherently exothermic (negative enthalpy) with the energy released known as the “heat” of adsorption; this word may be used interchangeably with the “enthalpy” of adsorption since at constant pressure, the change in enthalpy of a process is equal to the heat. The heat of adsorption is often used as a proxy for describing the binding energy between a gas molecule and a specific adsorbent.¹

The Lennard-Jones (LJ) potential is a model used to generally describe the attractive van der Waals interaction that results from the combination of longer-range attractive forces and short-range repulsive (Pauli exclusion) forces:

$$V_{\text{LJ}}(r) = 4\varepsilon_{\text{LJ}} \left[\left(\frac{\sigma_{\text{LJ}}}{r} \right)^{12} - \left(\frac{\sigma_{\text{LJ}}}{r} \right)^6 \right] \quad (1)$$

In a physisorption interaction, ε_{LJ} is the binding energy of the adsorbate on the adsorbent surface, σ_{LJ} is the distance of the adsorbate-adsorbent interaction at 0 K, and r is the distance between the adsorbate and the surface. The 12 term (r^{-12}) refers to the short-range repulsive forces, rationalized by the Pauli exclusion principle, while the 6 term (r^{-6}) describes the longer-range attractive dipole-dipole forces rationalized by random fluctuations of the electron density around any two species. In Figure 1, a representative plot of the LJ potential is shown with an arbitrary binding energy and equilibrium binding distance.

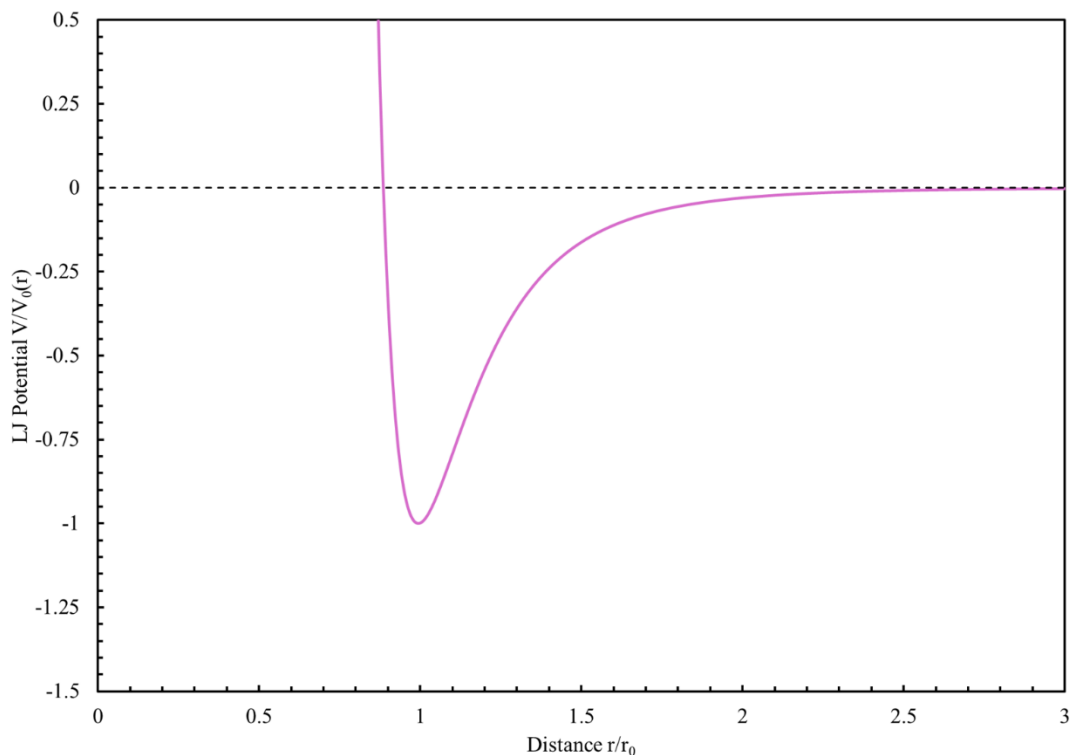


Figure 1. The Lennard-Jones 6-12 potential of a gas molecule on an adsorbent surface, with a binding energy of V_0 and equilibrium binding distance of r_0 .

The surface of an adsorbent can be simplistically thought of as a continuum of LJ potential energy wells, where the depth of the well corresponds to the binding energy of the adsorbate. A special case arises when considering interactions within a narrow pore of an adsorptive material, where two surface sites lie in proximity across a pore. In very narrow pores, the two sites' potential wells overlap, resulting in a single binding site with a higher binding energy than either site individually (as illustrated in Figure 2). However, this increased binding energy comes at the expense of needing twice as much adsorbent mass per adsorbate molecule, and hence comes with a trade-off in storage applications. These scenarios of open-surface, single-wall and double-wall pore confinement are explored in greater detail in Chapter 5.

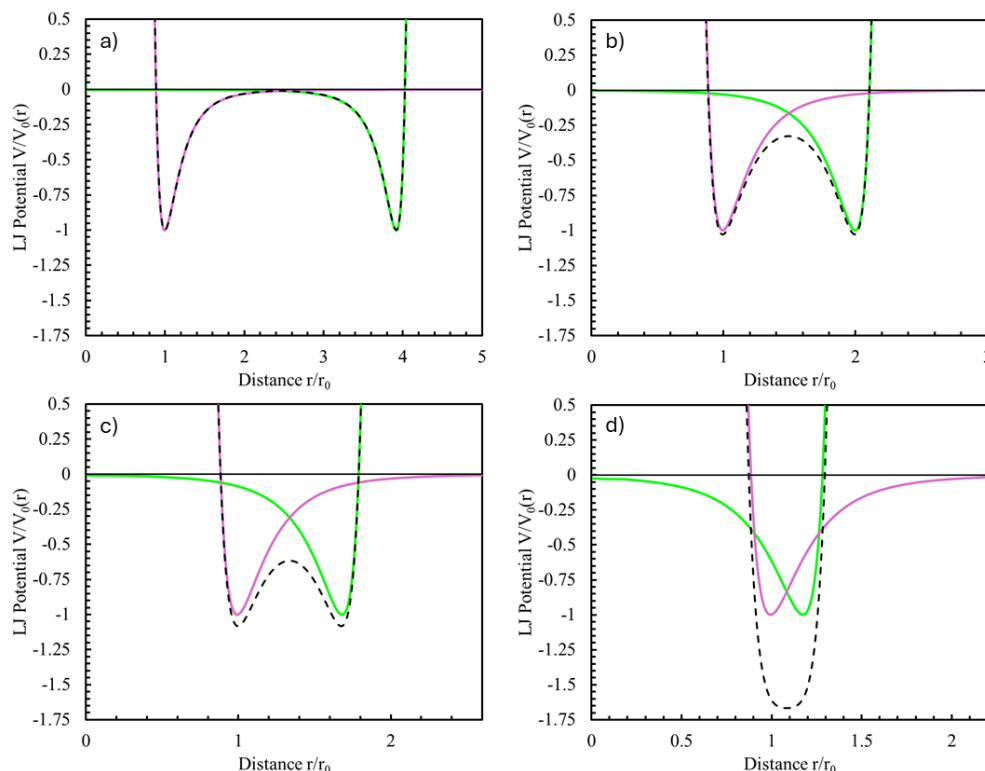


Figure 2. Lennard-Jones potential wells of two independent binding sites opposite one another inside a pore. As the pore size narrows (from a-d), the wells get closer to the unique distance (d) where there is overlap between the individual wells to create one singular well with higher binding energy.

Chemical Adsorption

A second type of adsorption, known as chemical adsorption (or chemisorption), occurs when the adsorbate and adsorbent chemically react to form a new bond between the two species. As a result, chemisorption is typically 10-100× stronger than physisorptive interactions. Unlike physisorption, chemisorption is generally irreversible at ambient temperature and pressure and often requires energy for both adsorption and desorption processes. Due to the strength of these chemical bonds and the conditions required, chemisorption often leads to permanent chemical alterations of the adsorbent surface. In contrast to physisorption, chemisorption often requires the

system to overcome an activation energy barrier. Materials that exhibit chemisorption with a specific gas molecule also can display physisorptive behavior if there is not enough energy (temperature and pressure) in the system to overcome the activation energy needed for the chemical bonds to form.² In general, shallow LJ potential wells (e.g., 1-10 kJ mol⁻¹) indicate weak interactions characteristic of physisorption, while deeper wells (e.g., 50-1000 kJ mol⁻¹) are typically associated with chemisorption.

Gas Adsorption Models

Langmuir Model

Adsorption has been observed and utilized by humans since antiquity, with early civilizations using it for medicinal purposes and water purification.³ In the 15th century, an accurate description of adsorption was provided by Leon Battista Alberti in his book *L'archiettura*.⁴ Alberti described the condensation of water on a porous surface, stating, “*I cannot deny that the humid air of the night is attracted by light earth or penetrates self-acting into the pores in which it may easily condense to wetness.*”³ Despite numerous historical observations and experiments, it wasn't until the early 20th century when Irving Langmuir wrote his three seminal articles that scientists had a physical description of adsorption at an atomistic level on solid and liquid interfaces.⁵⁻⁷ Langmuir originally derived his adsorption models using a kinetics approach, imagining adsorption and desorption of gas molecules in a molecularly thin layer on a two-dimensional surface. Langmuir made three crucial assumptions:

- i. the rate of incidence of the gas molecules in the bulk gas phase on a two-dimensional adsorbent surface, r_{inc} , is proportional to the pressure of the bulk phase at a constant temperature.

- ii. the rate of adsorption, r_{ads} , depends on the rate of incidence, r_{inc} , the probability of adsorption (contrary to elastic interactions), p_{ads} , and the probability of incidence at a vacant binding site, p_{vac} .
- iii. the desorption rate is equal to the desorption rate at maximum surface coverage, $r_{des,sat}$, multiplied by the fraction of binding sites occupied by adsorbed gas molecules, θ (disregarding any adsorbate-adsorbate interactions).

These three assumptions can be ultimately simplified when the bulk and adsorbed phases are treated as ideal (ignoring any intermolecular interactions) and every binding site on the surface is identical. Collectively, these assumptions and simplifying factors resulted in an equation that describes the simplest possible gas adsorption system, known as the Langmuir isotherm equation:

$$\theta = \frac{r_{inc}p_{ads}}{r_{des,sat} + r_{inc}p_{ads}} = \frac{KP}{1 + KP} \quad (2)$$

where K is the Langmuir constant, an indication of the strength of interaction between the adsorbate and adsorbent, and P is pressure.⁸ The Langmuir constant is independent of pressure and only depends on the temperature, as defined in Equation 3 based on the kinetic approach.

$$K = \frac{1}{\sqrt{2\pi mRT}} \frac{p_{ads}}{r_{des,sat}} \quad (3)$$

Where m is the mass of a single atom of the adsorbate, R is the gas constant and T is the temperature. When the adsorption system is kept in contact with a constant temperature reservoir, K can be calculated from the measured adsorption uptake as a function of pressure.

The Langmuir adsorption models (including the simplest variant above) can be more elegantly derived using first-principles statistical mechanics.⁹ The two possible microstates of an

adsorption site are: occupied or unoccupied. For a monolayer adsorbent, the occupied site contains one adsorbate ($N_1 = 1$) and the unoccupied site contains zero adsorbates ($N_0 = 0$). The adsorbed phase is treated as a constant volume that is permitted to exchange internal energy and particles with a thermal reservoir (constant temperature, T) and “chemical” reservoir (constant chemical potential, $\tilde{\mu}$). When the site is unoccupied, it is conventionally considered to have an energy of zero ($E_0 = 0$). If the site is occupied, its energy changes by a constant ($E_1 = \varepsilon$): the binding energy. The grand canonical partition function is used because the system is allowed to exchange energy and particles with the thermal and chemical reservoirs, and it is therefore most convenient. The single-site grand canonical partition function is:

$$\xi = \sum_{i=0}^1 e^{-\beta(E_i - \tilde{\mu}N_i)} = 1 + \Lambda^{-3} e^{\beta\tilde{\mu}} \int_{\Omega} e^{-\beta\varepsilon(x)} dx \quad (4)$$

where β is $(k_B T)^{-1}$, N_i is the number of molecules adsorbed, Λ is the thermal de Broglie wavelength of the adsorbate, x is a spatial dimension over which the adsorbate is allowed to explore, and Ω represents the entire binding site. If the adsorbate is treated as existing within a three-dimensional box (with square-well potentials in all three dimensions):

$$\xi = 1 + \Lambda^{-3} V_s e^{\beta\tilde{\mu}} e^{-\beta\varepsilon} \quad (5)$$

where V_s is the volume of the binding site. In the simplest model, all of the sites are identical, independent, and indistinguishable and the total grand canonical partition function, (Ξ), of the adsorption system (containing N_s sites) is:

$$\Xi = \prod_{i=1}^{N_s} \xi_i = (1 + \Lambda^{-3} V_s e^{\beta\tilde{\mu}} e^{-\beta\varepsilon_i})^{N_s} \quad (6)$$

The expected number of adsorbed molecules $\langle N_a \rangle$, determined by the temperature and chemical potential of the reservoir, can be calculated by taking a derivative of the logarithm of the total grand canonical partition function:

$$\langle N_a \rangle = \left(\frac{\partial \log \Xi}{\partial (\beta \tilde{\mu})} \right) = N_s \frac{\Lambda^{-3} V_B e^{\beta \tilde{\mu}} e^{-\beta \varepsilon}}{1 + \Lambda^{-3} V_s e^{\beta \tilde{\mu}} e^{-\beta \varepsilon}} \quad (7)$$

In this form, the pressure dependence of the model is not apparent, but if the bulk adsorbate reservoir can be treated as an ideal gas, the chemical potential of the ideal gas can be substituted for $\tilde{\mu}$:

$$\tilde{\mu} = k_B T \log(\Lambda^3 \beta P) \quad (8)$$

This gives for the surface site occupancy, θ :

$$\theta = \frac{\langle N_a \rangle}{N_s} = \frac{KP}{1 + KP} \quad (9)$$

$$K = \beta V_s e^{-\beta \varepsilon} = A e^{\frac{-\varepsilon}{RT}} \quad (10)$$

where in this case $A = V_s/k_B T$. According to this derivation, the Langmuir constant should have two parts: an exponential part and a pre-factor. Depending on the degrees of freedom the adsorbate retains when it transitions into the adsorbed phase (here treated as a three-dimensional box), the temperature dependence of the pre-factor (A) can vary. For an adsorbed state treated as a three-dimensional box (“3D ideal gas”), the temperature dependence of the pre-factor (as shown in Equation 10) is found to be T^{-1} . Some other cases are shown in Figure 3 and this concept is explored more deeply in Chapter 3.

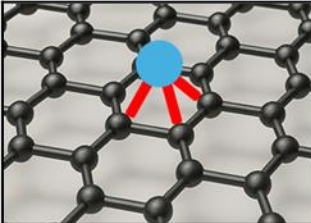
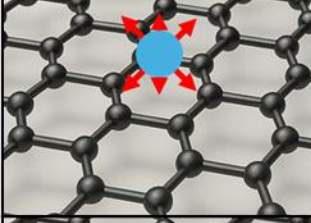
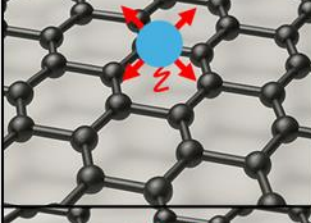
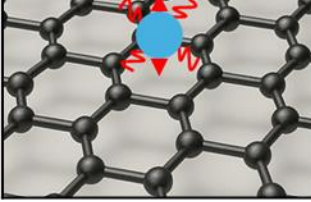
Visual Representation of Adsorbate Degrees of Freedom	Model Name	Partition Function	Langmuir Constant Temperature Dependence
	Fixed	$DF \times DF \times DF$	$K[T] = \frac{constant}{T^{2.5}} e^{-\frac{\varepsilon}{k_B T}}$
	3D Ideal Gas	$SP \times SP \times SP$	$K[T] = \frac{constant}{T^1} e^{-\frac{\varepsilon}{k_B T}}$
	2D Ideal Gas with z-Oscillation	$SP \times SP \times QP$	$K[T] = \frac{constant}{T^{0.5}} e^{-\frac{\varepsilon}{k_B T}}$
	(No physical picture)	$QP \times QP \times SP$	$K[T] = constant e^{-\frac{\varepsilon}{k_B T}}$

Figure 3. Visual representations of the adsorbate's degrees of freedom when in the adsorbed phase, the underlying partition functions, and the temperature dependence of the Langmuir constant. The three spatial partition functions are: delta function (DF), square potential (SP), and quadratic potential (QP). This figure was adapted from elsewhere.¹⁰

More complex Langmuir-type models can be easily derived by accounting for more sites with different binding energies, where each site has its own Langmuir constant, pre-exponential factor, and binding energy. The multi-site Langmuir model is:

$$\theta = \frac{\langle N_a \rangle}{N_s} = \sum_k \alpha_k \frac{K_k [T] P}{1 + K_k [T] P} \quad (11)$$

where k indicates the site type. Additional variables such as the formation of multiple layers, cooperation between sites, and dissociation upon adsorption can also be used to derive a variety of models.⁸

Freundlich and Langmuir-Freundlich Model

In 1909, a decade before Langmuir's seminal papers were published, Herbert Freundlich developed an early empirical adsorption model¹¹:

$$\frac{m_{adsorbate}}{m_{adsorbent}} = K_f \cdot c_{eq}^{\frac{1}{n_f}} = K_f \cdot P^{\frac{1}{n_f}} \quad (12)$$

where m_x is the mass of the adsorbate or adsorbent, K_f is the binding constant, c_{eq} is the concentration of the adsorbate at equilibrium, and n_f is the Freundlich coefficient. The Freundlich coefficient is associated with the heterogeneity of adsorption ($n_f > 1$). Similarly to the Langmuir model, the Freundlich model does not account for intermolecular interactions between molecules (i.e., the free gas phase and adsorbed phase are treated as ideal). Unlike the Langmuir model, the Freundlich equation assumes the binding sites' energies are non-uniform and this is accounted for by the Freundlich coefficient. For this reason, the Freundlich model can be used for multilayer adsorption on homogeneous surfaces as well as monolayer adsorption on heterogeneous surfaces. When the Freundlich coefficient is equal to 1, Henry's law is obtained. A few disadvantages of both the Freundlich model and Henry's law are that they do not predict an adsorption maximum, and are therefore not thermodynamically consistent in systems with a fixed quantity of adsorbent.¹² Due to these failures, the Freundlich model and Henry's law are only applicable in narrow ranges of temperature and pressure (typically in the dilute limit).

The Langmuir-Freundlich (Sips) model is a semi-empirical model that combines the two prior models developed for predicting the adsorption of gas molecules on a heterogeneous surface:¹³

$$\theta = \frac{(K_{Lf}P)^{1/n_{Lf}}}{1 + (K_{Lf}P)^{1/n_{Lf}}} \quad (13)$$

where θ is the fractional surface occupancy, P is the pressure of the free gas, K_{Lf} is the binding constant, and n_{Lf} is the Langmuir-Freundlich coefficient (or “heterogeneity factor”). When $n_{Lf} = 1$, the above equation simplifies into the single-site Langmuir model, indicating a purely homogeneous binding surface. When $n_{Lf} > 1$, it is an indicator of the heterogeneity of the surface. At high pressures, the Langmuir-Freundlich model approaches monolayer adsorption but at low pressures the model behaves similarly to the original Freundlich model. The thermodynamic and physical properties ascertained by fitting experimental measurements to the Langmuir-Freundlich equation can be non-physical due to the empirical nature of this model.

Hill Model

Another adsorption model was developed by Archibald V. Hill in 1910 in efforts to describe the binding of oxygen to hemoglobin¹⁴:

$$\frac{\text{Bound Ligands}}{\text{Total Receptors}} = \frac{K_H [L]^{n_H}}{1 + K_H [L]^{n_H}} \quad (14)$$

where K_H is the binding constant, $[L]$ is the total ligand concentration, and n_H is the Hill coefficient, a metric of cooperativity that loosely represents the number of ligands bound per receptor. In a gas adsorbate-solid adsorbent system, the Hill equation is used to describe the cooperative binding of multiple gas molecules on the same or neighboring binding sites. When

$n_H = 1$, there is a single gas molecule per binding site, and the Hill model is identical to the single-site Langmuir model. When $n_H > 1$, it indicates positive cooperativity between adsorbed molecules; but, when $n_H < 1$, it is an indication of repulsive forces between the adsorbed molecules. Unlike the previous two models, the Hill model is capable of fitting a unique isotherm shape with a very sharp rise at the critical pressure for the adsorption system. This model has been successfully employed for describing the cooperative adsorption of CO₂ on MOFs.¹⁵ In line with its original intention, the Hill equation plays an important role in biological research.¹⁶

Gibbs Surface Excess

Josiah Willard Gibbs first described the general principles of adsorption and developed a mathematical relationship between the absolute adsorbed amount and the measured amount, now known as the Gibbs surface excess.¹⁷ Experimental adsorption measurements have the issue of being able to measure only the excess adsorbed amount and not the absolute adsorbed amount. This is noticeable at pressures and temperatures near or above the critical point of the adsorbate fluid, where the measured adsorbed amount goes through a maximum (Figure 4). This behavior is not consistent with Langmuir's adsorption model where the adsorbed amount monotonically increases with pressure until it reaches the total number of adsorption sites on the surface. Gibbs's work shows that adsorption experiments are only able to discern the amount adsorbed "in excess" of the bulk gas density that would not have been in the same volume in the absence of the adsorbed phase (Figure 4). The reference molecules in the adsorbed phase are excluded from the measured adsorbed amount when the bulk gas density is accounted for. To calculate the

absolute adsorbed amount (the total number of molecules in the adsorbed phase), the Gibbs definition of excess adsorption is employed:

$$n_e[T, P] = n_a[T, P] - \rho_g[T, P] \cdot V_a[T, P] \quad (15)$$

where the n_a is the absolute adsorbed uptake, n_e is the experimentally measured excess adsorbed uptake, ρ_g is the bulk gas density, and V_a is the volume of the adsorbed phase. All are functions of pressure and temperature, however the volume of the adsorbed phase, V_a , is difficult to measure experimentally.¹⁸ At low pressures, the volume of the adsorbed phase and density of the bulk fluid are negligibly low, and the excess and absolute adsorbed amount can be treated as equivalent for all modeling and thermodynamic purposes. At high enough pressures and temperatures, the excess adsorbed amount reaches a maximum and then appears to decrease, clearly indicating that the bulk gas phase contribution to the adsorbed amount is non-negligible. This is readily apparent in the supercritical adsorption equilibria throughout this dissertation and must be accounted for in all fitting exercises.

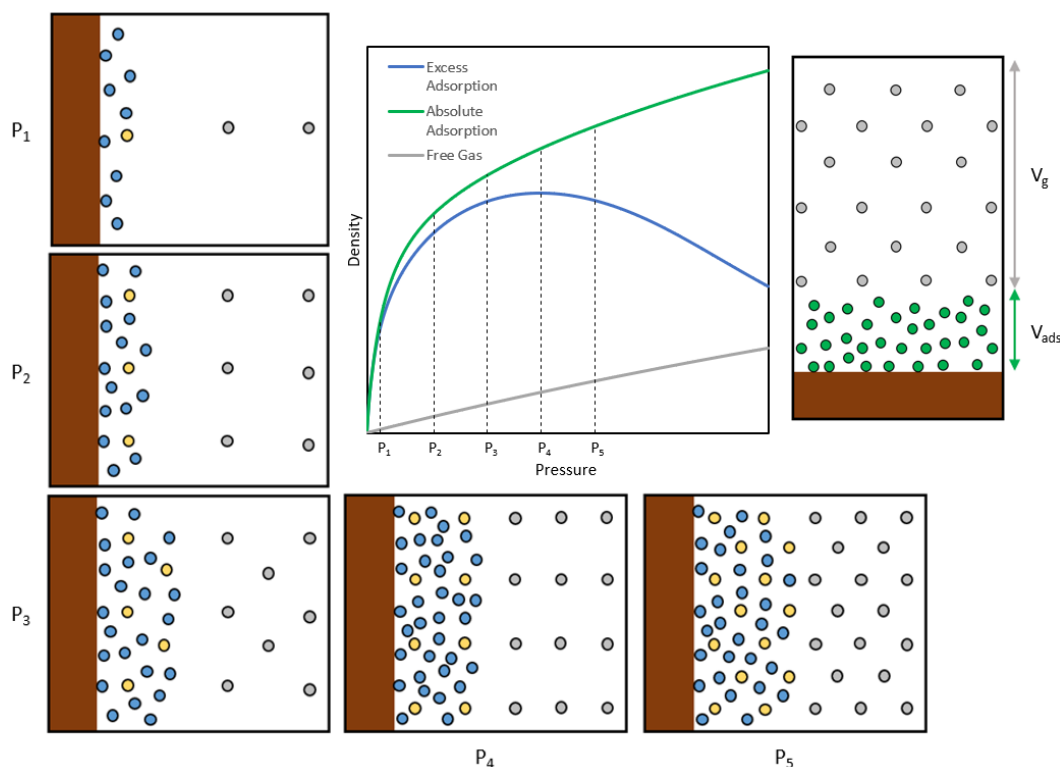


Figure 4. Representation of absolute and excess adsorption along an adsorption isotherm. The excess (blue), reference (yellow), and absolute (combined, green) adsorbed quantities are shown at five pressures P_1 - P_5 . The bulk fluid (gray) is shown as a crystal to emphasize constant density and geographical location. This figure was adapted from elsewhere.¹⁹

Adsorption Thermodynamics

Isosteric Enthalpy of Adsorption

Adsorption is a spontaneous interaction and thus there is a release of energy from the system and a decrease in the total free energy of the system. This release of energy as the gas molecule transitions from the bulk gas to the adsorbed phase is described as the enthalpy of adsorption. The isosteric enthalpy of adsorption is the amount of energy released at a fixed adsorbed amount and is commonly used as a proxy for the strength of binding of the adsorption system.

At equilibrium, the change in the Gibbs free energy is zero and the chemical potentials, μ_i , of the free gas and adsorbed phases are equal:

$$\mu_g = \mu_a \quad (16)$$

By using the Gibbs-Duhem relationship for the adsorbed phase and gas phase:

$$d\mu_i = -s_i dT + v_i dP \quad (17)$$

For an adsorbed system at a constant amount adsorbed, n_a , Equations 16-17 are combined to obtain:

$$-s_g dT + v_g dP = -s_a dT + v_a dP \quad (18)$$

Upon rearranging:

$$\frac{dP}{dT} = \frac{s_a - s_g}{v_a - v_g} \quad (19)$$

When the system is at equilibrium ($\Delta_{ads}G = 0$), the change in enthalpy of adsorption and change in entropy of adsorption are related by:

$$\Delta_{ads}H = T\Delta_{ads}S \quad (20)$$

where $\Delta_{ads}x = x_a - x_g$ refers to the process of adsorption. In other work, this is commonly written as Δx_{ads} but the definition is the same. After substitution the resulting relationship is referred to as the Clapeyron equation:

$$\left(\frac{\partial P}{\partial T}\right)_{n_a} = \frac{\Delta_{ads}H}{T\Delta_{ads}v} \quad (21)$$

At equilibrium, the enthalpy of adsorption is:

$$\Delta_{ads}H[T, P] = T\Delta_{ads}S = T\left(\frac{\partial P}{\partial T}\right)_{n_a} (v_a - v_g) \quad (22)$$

When the system is at near ideal conditions (low pressure), the molar volume of the gas phase, v_g , is significantly larger than the molar volume of the adsorbed phase, v_a ($v_g \gg v_a$). Under these conditions the bulk fluid can be treated as an ideal gas as well and therefore the ideal gas law is substituted for the volume of the gas phase, resulting in the Clausius-Clapeyron variant of the Clapeyron equation:

$$-\Delta_{ads}H[T, P] = \frac{RT^2}{P} \left(\frac{\partial P}{\partial T} \right)_{n_a} \quad (23)$$

The $\left(\frac{\partial P}{\partial T} \right)_{n_a}$ in both the Clapeyron and the Clausius-Clapeyron equation is dependent on the adsorption model, alluding to a direct relationship between the isosteric enthalpy of adsorption and the fitting model. This inherent relationship between the different models and their isosteric enthalpies of adsorption is explored in Chapter 3 and Chapter 4 where the temperature dependence of the Langmuir constant is systematically explored.

Isoexcess Enthalpy of Adsorption

For experimental adsorption measurements at sufficiently low pressures or near “ideal” conditions, where the density of the free bulk fluid is effectively negligible, the excess adsorbed amount is almost equal to the absolute adsorbed amount. Under such conditions, it is possible to treat the excess adsorption equilibria as equal to the absolute adsorption uptake and thereby calculate the isosteric enthalpy of adsorption directly; this method is known as the isoexcess method. As the density of the bulk gas increases, the difference between the two quantities increases, and the isoexcess method becomes invalid. In the isoexcess approach, the enthalpy of adsorption is defined as:

$$-\Delta_{ads}H[T, P] = \frac{RT^2}{P} \left(\frac{\partial P}{\partial T} \right)_{n_e} \quad (24)$$

The only difference between the isoexcess enthalpy of adsorption and the isosteric is that the isoexcess derivative is taken at constant excess adsorbed amount and is hence only a valid approximation of the isosteric quantity under dilute conditions.

Experimental Adsorption Fitting

To elucidate the thermodynamic and physical characteristics of an adsorption system from experimental measurements, a fitting equation and/or model is required to determine the amount adsorbed as a function of temperature and pressure. The Gibbs excess definition can be rewritten in terms of maximum uptake and surface coverage:

$$n_e[T, P] = n_a[T, P] - \rho_g[T, P] \cdot V_a[T, P] = (n_{max} - \rho_g[T, P] \cdot V_{max})\theta[T, P] \quad (25)$$

$$\theta[T, P] = \frac{n_a[T, P]}{n_{max}} \quad (26)$$

where n_{max} is the maximum adsorbed amount, V_{max} is the maximum adsorbed volume, and θ is the fractional surface site occupancy. An underlying assumption of this equation is that the adsorbed volume, V_a , dynamically changes with the fraction of sites occupied, and can be approximated simply by multiplying a constant (V_{max}) by the surface occupancy fraction. In porous solids, the maximum adsorbed volume can be estimated using the total pore volume, V_{pore} , or it can be an independent fitting parameter and determined from the experimental adsorption isotherms.¹⁹

Fitting experimental adsorption isotherms is not limited to the use of conventional adsorption models previously described; alternative empirical and mathematical approaches may also be employed to achieve an adequate representation of the data. A simple and crude method

for fitting experimental adsorption isotherms is using a best fit line or linear interpolation between the points. These methods are not able to determine the absolute uptake or the volume of the adsorbed phase for the material but using the relationship in Equation 23, the enthalpy of adsorption can be calculated. In this approach, there is no temperature dependence, and each isotherm is fitted independently. Therefore, upon calculation of the isoexcess enthalpy of adsorption, it is deduced to be indicative of the average temperature of the experimental conditions.

Alternatively, global fitting of the experimental adsorption data is possible but requires a built-in temperature dependence to the adsorption model. This method also leads to a temperature dependence of the isosteric enthalpy of adsorption. In this work, experimental adsorption equilibria were often globally fitted to a variant of the generalized Langmuir equation:

$$n_e[T, P] = (n_{max} - \rho_g[T, P] \cdot V_{max}) \sum_i \alpha_i \frac{K_i[T]P}{1 + K_i[T]P} \quad (27)$$

As a pedagogical example, methane adsorption on MOF-5 will be used to compare the calculated isoexcess enthalpy of adsorption from linear interpolation to the isosteric enthalpy of adsorption from fitting to the double-site Langmuir model (Figure 5). This adsorption system is more thoroughly explored and discussed in Chapter 4.

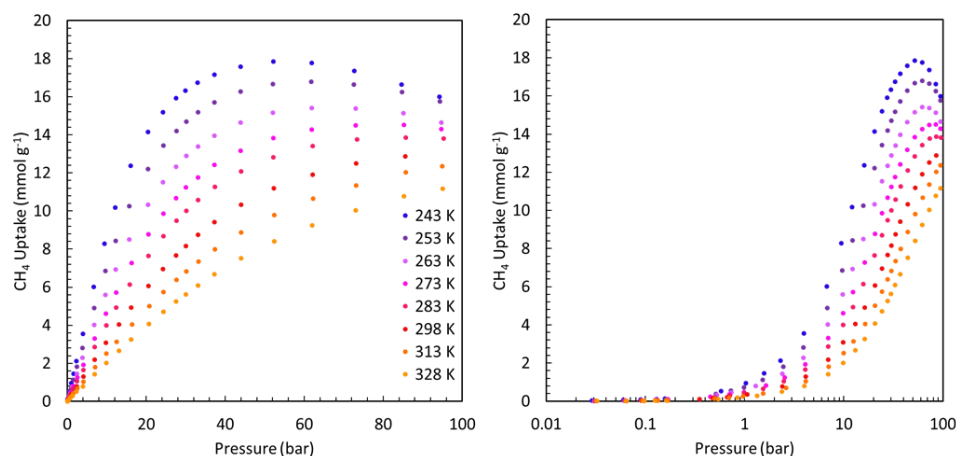


Figure 5. Excess methane adsorption on MOF-5 between 243–328 K and 0–100 bar.

Linear Interpolation

Using linear interpolation to fit excess adsorption isotherms is the simplest method for fitting as it does not require any physical information about the material or a fitting model. This method provides a way of determining pressure values at constant excess adsorbed amount, n_e , that will be used to calculate the isoexcess enthalpy of adsorption. Methane excess adsorption on MOF-5 goes through a maximum of $\sim 18 \text{ mmol g}^{-1}$ at 243 K indicating the bulk gas phase is non-negligible under these experimental conditions. This will cause the reported isoexcess enthalpy of adsorption to be invalid at higher n_e values but is still a reasonable around the Henry's law (dilute) limit.^{1,19} The linear interpolation of the raw data, resulting van't Hoff plot, and resulting isoexcess enthalpy of adsorption at the thermodynamic average temperature (279 K) are shown in Figure 6. The van't Hoff plot shows the approximately constant heat of adsorption, even with such a simple method used to analyze the experimental data. The isoexcess enthalpy of adsorption spuriously increases at higher adsorbed amount where the density of the bulk phase is no longer negligible and the isoexcess method is invalid.

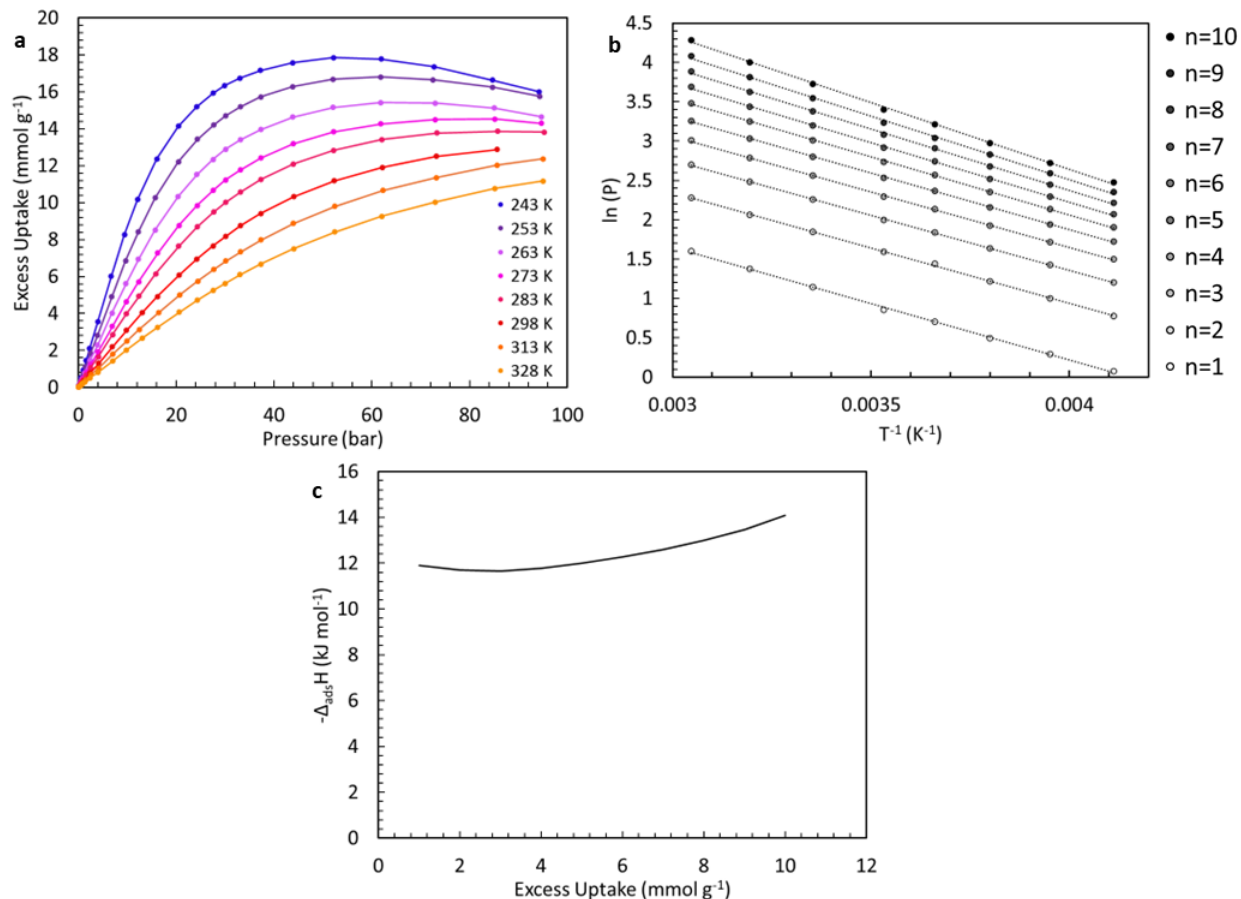


Figure 6. (a) Linear interpolation of the experimental excess adsorption of methane on MOF-5, and corresponding (b) van't Hoff plot and (c) isoexcess enthalpy of adsorption.

Generalized Langmuir Fitting

The isoexcess approach does satisfyingly report the enthalpy of adsorption in the high uptake regime at supercritical conditions. By incorporating the Gibbs definition of excess adsorption and by using simple Langmuir-type model (Equation 27), the increasing density of the bulk phase approaching that of the adsorbed fluid is accounted for, and a physically meaningful shape of the isotherm is enforced. The experimental methane adsorption equilibria were fitted to a double-site Langmuir model with a temperature dependence of the prefactor of the Langmuir constant of $T^{-0.5}$ (Figure 7). The double-site Langmuir does an adequate job

fitting all the excess adsorption data except at the highest pressures where it starts to deviate from the experimental data. One of the key assumptions made by Langmuir is that the adsorbed phase and free gas are ideal and, in those conditions, both phases are far from ideal causing this deviation. The isosteric enthalpy of adsorption of supercritical adsorption is calculated using the Clapeyron equation¹ (Equation 22). The $\left(\frac{\partial P}{\partial T}\right)_{n_a}$ term is dependent on the adsorption model used and can be determined using the relationship¹⁹:

$$\left(\frac{\partial P}{\partial T}\right)_{n_a} = \left(\frac{\partial \theta}{\partial P}\right)_{n_a}^{-1} \sum_i \left(\frac{\partial \theta}{\partial K_i}\right)_{n_a} \left(\frac{\partial K_i}{\partial T}\right)_{n_a} \quad (28)$$

For the double-site Langmuir adsorption model:

$$\left(\frac{\partial \theta}{\partial P}\right)_{n_a} = \left(\frac{\partial}{\partial P}\right)_{n_a} \left((1 - \alpha) \frac{K_1 P}{(1 + K_1 P)^2} + \alpha \frac{K_2 P}{(1 + K_2 P)^2} \right) \quad (29)$$

$$= \left((1 - \alpha) \frac{K_1}{(1 + K_1 P)^2} + \alpha \frac{K_2}{(1 + K_2 P)^2} \right) = X^{-1} \quad (30)$$

$$\left(\frac{\partial \theta}{\partial K_1}\right)_{n_a} = (1 - \alpha) \frac{P}{(1 + K_1 P)^2} = Y_1 \quad (31)$$

$$\left(\frac{\partial \theta}{\partial K_2}\right)_{n_a} = \alpha \frac{P}{(1 + K_2 P)^2} = Y_2 \quad (32)$$

$$\left(\frac{\partial K_i}{\partial T}\right)_{n_a} = \left(\frac{\partial}{\partial T}\right)_{n_a} \left(\frac{A_i}{T^x} e^{\frac{\varepsilon_i}{RT}} \right) = -\frac{(\varepsilon_i - xRT)}{RT^2} K_i = -Z_i \quad (33)$$

where R is the gas constant, x is temperature dependence of the Langmuir constant that was explored earlier, and the binding energies, ε_i , are negative for adsorption. The isosteric enthalpy of adsorption for methane on MOF-5 is shown in Figure 7 (for $x = 0.5$) and the Henry's law limit is consistent with that of the linear interpolation result: $\sim 12 \text{ kJ mol}^{-1}$. When using a Langmuir model that has an inherent temperature dependence, a temperature dependence is also

carried into the isosteric enthalpy of adsorption, as seen in Figure 7. As the temperature dependence (i.e., x) increases, so does the spread of the isosteric enthalpy of adsorption. The spread of the isosteric enthalpy of adsorption with x is explored in Chapter 3.

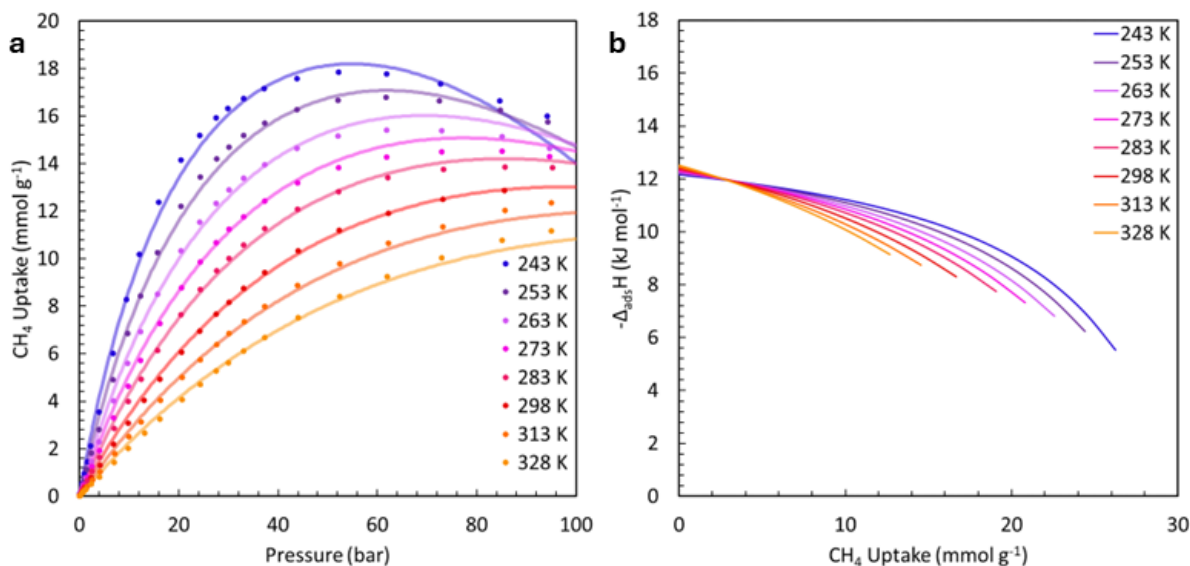


Figure 7. (a) . Equilibrium excess uptake (circles) of CH₄ on MOF-5 between 243-328 K and 0-100 bar, fitted to a double-site Langmuir model. (b) Isosteric enthalpy of adsorption of CH₄ on MOF-5 between 243-328 K and 0-100 bar based on a double-site Langmuir model.

To account for the gas-gas interactions in the free gas phase, fugacity can be used as the independent variable in the isotherm model instead of pressure. Fugacity is a corrected pressure term that accounts for the non-ideal behavior of real gases.

$$f = P \cdot \phi[P, T] \quad (34)$$

where f is fugacity, P is pressure, and ϕ is the fugacity coefficient. Ideal gases have a fugacity coefficient of 1 under all conditions. This is a reasonable assumption for real gases at near “ideal” conditions (e.g., at low pressure and near room temperature). Under experimental conditions where this assumption is not valid (e.g., high pressure and/or low temperature), the

fugacity can be substituted for pressure in thermodynamic calculations and fitting of the measured uptake. For example, in the case of the multi-site Langmuir model:

$$n_e[T, f] = (n_{max} - \rho_g[T, f] \cdot V_{max}) \sum_i \alpha_i \frac{K_i[T]f}{1 + K_i[T]f} \quad (35)$$

Adsorption Instrumentation

A common experimental approach for measuring adsorption isotherms is the volumetric technique, which involves stepwise dosing or evacuation of gas from a reference volume that is connected to the sample cell, enabling the calculation of the excess adsorbed amount as a function of pressure. A volumetric (or “Sieverts”) apparatus has a precisely calibrated reference and sample cell volume where the sample is dosed with known quantities of adsorbate at a constant temperature. Alternatively, in a gravimetric apparatus, the sample is suspended on a balance within a closed volume and the change in mass is used to calculate the uptake upon each dose of gas. The bulk gas density at a given temperature and pressure is determined using one of many thermophysical property libraries (e.g., CoolProp²⁰ or Refprop²¹) that contain high-accuracy “real gas” models for many common fluids. From the bulk gas densities measured at the end of the dosing steps, the amount of gas adsorbed during each step can be determined. The quality of the experiments is highly dependent on the amount of gas adsorbed and ensuring the ratio of bulk gas volume to adsorbed phase is as small as possible.

In this work, a custom high-pressure volumetric Sieverts apparatus as well as a commercial low-pressure, high-resolution volumetric Sieverts apparatus (3Flex, Micromeritics Corp.) were used to measure the adsorption equilibria. The high-pressure Sieverts (shown in Figure 8) has a measurable pressure range up to 200 bar and a temperature range from 40 K

(using a cryostat) up to ~ 750 K (using heating tape). The volume was calibrated using helium expansion as well as by comparison of measured adsorption uptake to reference adsorption isotherms. The 3Flex is an automated volumetric Sieverts apparatus designed for high-resolution adsorption measurements at below atmospheric pressure (typically 10^{-6} to 10^3 mbar). The temperature range of the 3Flex is between 40-298 K using the same cryostat as described above.

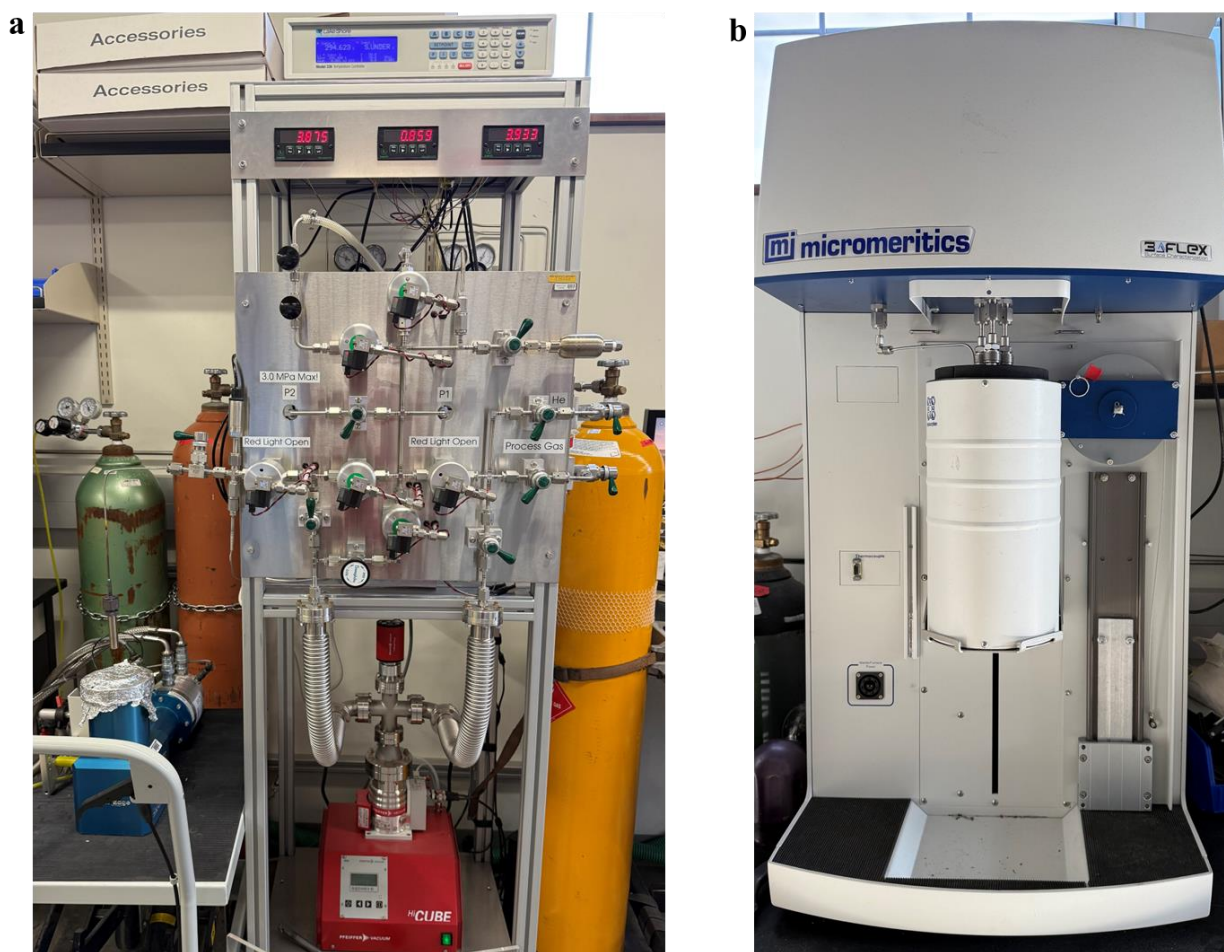


Figure 8. (a) Custom high-pressure volumetric Sieverts apparatus used for high-pressure (1-120 bar) adsorption measurements. (b) Commercial high-resolution volumetric Sieverts apparatus used for microstructural properties and low pressure (<1 bar) adsorption measurements.

References

- (1) Nuhnen, A.; Janiak, C. A practical guide to calculate the isosteric/enthalpy of adsorption via adsorption isotherms in metal-organic frameworks, MOFs. *Dalton Trans.* **2020**, 30 (49), 10295-10307. DOI: 10.1039/D0DT01784A.
- (2) Barghi, S. H.; Tsotsis, T. T.; Sahimi, M. Chemisorption, physisorption and hysteresis during hydrogen storage in carbon nanotubes. *Int. J. Hydrogen Energy* **2014**, 39, 1390-1397. DOI: 10.1016/j.ijhydene.2013.10.163.
- (3) Dabrowski, A. Adsorption – from theory to practice. *Adv. Colloid Interface Sci* **2001**, 93, 135-224. DOI: 10.1016/s0001-8686(00)00082-8.
- (4) Alberti, L. B. *L'architettura*; Padua, Firenze, Italy, 1483/1485.
- (5) Langmuir, I. The Constitution and Fundamental Properties of Solids and Liquids. Part I. Solids. *J. Am. Chem. Soc.* **1916**, 38 (11), 2221–2295. DOI: 10.1021/ja02268a002.
- (6) Langmuir, I. The Constitution and Fundamental Properties of Solids and Liquids. Part II. Liquids. *J. Am. Chem. Soc.* **1917**, 39 (9), 1848-1906. DOI: 10.1021/ja02254a006.
- (7) Langmuir, I. The Adsorption of Gases on Plane Surfaces of Glass, Mica and Platinum. *J. Am. Chem. Soc.* **1918**, 40 (9), 1361–1403. DOI: 10.1021/ja02242a004.
- (8) Swenson, H.; Stadie, N. P. Langmuir's Theory of Adsorption: A Centennial Review. *Langmuir* **2019**, 35 (16), 5409-5426. DOI: 10.1021/acs.langmuir.9b00154.
- (9) Callen, H. B. *Thermodynamics and Introduction to Thermostatistics*, Second ed; John Wiley & Sons: New York, NY, 1985.
- (10) Quine, C. M. Tunability of Gas Adsorption Enthalpies in Carbonaceous Materials for Energy-Related Applications, Ph.D. Dissertation, California Institute of Technology, 2023. <https://thesis.library.caltech.edu/15222/>.
- (11) Freundlich, H. *Kapillarchemie: eine Darstellung der Chemie der Kolloide und verwandter Gebiete*; Akademische Verlagsgesellschaft, 1909.
- (12) Do, D. D. *Adsorption Analysis: Equilibria and Kinetics*, Imperial College Press, 1998.
- (13) Tzabar, N.; ter Brake, H. J. M. Adsorption isotherms and Sips models of nitrogen, methane, ethane, and propane on commercial activated carbons and polyvinylidene chloride. *Adsorption* **2016**, 22, 901-914. DOI: 10.1007/s1045-0169794-9.
- (14) Hill, A. V. The possible Effects of the Aggregation of the Molecules of Haemoglobin on Its Dissociation Curves. *J. Physiol.* **1910**, 40, 4-7.

- (15) Zhu, Z.; Parker, S. T.; Forse, A. C.; Lee, JH.; Siegelman, R. L.; Milner, P. J.; Tsai, H.; Ye, M.; Xiong, S.; Paley, M. V., et. al. Cooperative Carbon Dioxide Capture in Diamine-Appended Magnesium-Olsalazine Frameworks. *J. Am. Chem. Soc.* **2023**, *145* (31), 17151-17163. DOI: 10.1021/jacs.3c03870.
- (16) Gesztelyi, R.; Zsuga, J.; Kemeny-Beke, A.; Varga, B.; Juhasz, B.; Tosaki, A. The Hill equation and the origin of quantitative pharmacology. *Arch. Hist. Exact Sci.* **2012**, *66*, 427-438. DOI: 10.1007/s00407-012-0098-5.
- (17) Josiah Willard Gibbs. On the equilibrium of heterogeneous substances. *Am. J. Sci. Arts* **1878**, *s3-16* (96), 441-458. DOI: 10.2475/ajs.s3-16.96.441.
- (18) Parilla, P. A.; Gross, K.; Hurst, K.; Gennett, T. Recommended volumetric capacity definitions and protocols for accurate standardized and unambiguous metrics for hydrogen storage materials. *Appl. Phys. A* **2016**, *122*, 201. DOI: 10.1007/s00339-016-9654-1.
- (19) Stadie, N. P. Synthesis and Thermodynamic Studies of Physisorptive Energy Storage Materials. Ph. D. Dissertation, California Institute of Technology, Pasadena, CA, 2012. <https://thesis.library.caltech.edu/7198/>.
- (20) Bell, I. H.; Wronski, J.; Quoilin, J.; Lemort, V. Pure and Pseudo-pure Fluid Thermophysical Property Evaluation and the Open-Source Thermophysical Property Library CoolProp. *Ind. Eng. Chem. Res.* **2014**, *53* (6), 2498-2508. DOI: 10.1021/ie4033999.
- (21) Lemmon, E.; Huber, M.; McLinden, M. *NIST Standard Reference Database 23: Reference Fluid Thermodynamic and Transport Properties-REFPROP, Version 9.1*; National Institute of Standards and Technology, 2013. <https://www.nist.gov/publications/nist-standard-reference-database-23-reference-fluid-thermodynamic-and-transport>.

CHAPTER THREE

THE TEMPERATURE DEPENDENCE OF THE LANGMUIR
ADSORPTION MODEL FOR A SINGLE SITE METAL-
ORGANIC FRAMEWORK

Contribution of Authors and Co-Authors

Manuscript in Chapter 3

Author: Dalton Compton

Contributions: Collected adsorption isotherms, analyzed data, produced figures, and wrote the manuscript.

Co-Author: Nan-Chieh Chiu

Contributions: Synthesized materials, collected x-ray diffraction, and assisted in editing the manuscript.

Co-Author: Kyriakos C. Stylianou

Contributions: Oversaw synthesis of materials, aided in interpretation of results and assisted in editing the manuscript.

Co-Author: Nicholas P. Stadie

Contributions: Oversaw experimental design, aided in interpretation of results, assisted in writing and editing the manuscript.

Manuscript Information

Dalton Compton, Nan-Chieh Chiu, Kyriakos Stylianou, and Nicholas P. Stadie

[†] Department of Chemistry and Biochemistry, Montana State University, Bozeman, Montana, 59717, United States

[‡] Materials Discovery Laboratory (MaD Lab), Department of Chemistry, Oregon State University, Corvallis, Oregon, 97331, United States

Status of Manuscript:

- ☐ Prepared for submission to a peer-reviewed journal
- ☐ Officially submitted to a peer-reviewed journal
- ☒ Accepted by a peer-reviewed journal
- ☐ Published in a peer-reviewed journal

ACS Langmuir

DOI: 10.1021/acs.langmuir.5c00757

Abstract

The single-site Langmuir adsorption model, also known as the Langmuir isotherm equation, is one of the simplest possible descriptions of adsorption phenomena, and yet finds widespread applicability across a range of disciplines. In its simplest form, it is deployed to treat adsorption equilibria at constant temperature (i.e., along isotherms); however, at the heart of its derivation is a more general class of models that each incorporate an explicit temperature dependence, subject to assumptions about the spatial/translational degrees of freedom of the adsorbed species. In this work, measurements of the temperature dependence of supercritical adsorption of H₂ on a single-site metal-organic framework (MOF) are presented, and fitted using a range of Langmuir models with distinct treatments of degrees of freedom in the adsorbed phase. Surprisingly, all of the models can be used to adequately represent the measured data (to within 0.0003 mmol g⁻¹ per point), despite yielding significantly different values for binding energy and the temperature dependence of the isosteric enthalpy of adsorption (i.e., the isosteric heat, q_{st}). However, a critical finding of this work is that the mean-temperature isosteric enthalpy of adsorption remains consistent across all models within experimental error ($\pm 0.1\%$ or < 0.1 kJ mol⁻¹), highlighting its reliability for evaluating adsorption thermodynamics.

Introduction

In the theory of adsorption, defined as the densification of one phase at the interface (or phase boundary) of another, the equations derived by Irving Langmuir in 1916-1918 have served as foundational models that can accurately describe certain simple systems based on an atomistic picture of site-by-site and layer-by-layer interactions.¹⁻³ The simplest Langmuir-type adsorption

model, also referred to as the single-site Langmuir (SL) equation, is constructed based on a minimalist description of adsorption of a fluid or dissolved species at the surface of a rigid adsorbent containing a fixed number of adsorption sites, where three important assumptions are held:

- i. every adsorption site is distinguishable and identical,
- ii. every adsorption site can host up to one adsorbate molecule, and
- iii. there are no interactions between adsorbate molecules, in the bulk fluid nor in the adsorbed phase.

When the bulk fluid is a pure ideal gas and the adsorbent is a solid, the SL equation is derived in terms of the pressure of the gas:

$$n_a[P] = n_s \frac{KP}{1 + KP} \quad \text{Eq. 1}$$

where n_a is the amount adsorbed (typically per unit mass of the solid adsorbent), n_s is the maximum amount adsorbed or total number of adsorption sites (also, typically per unit mass of solid adsorbent), P is the pressure of the ideal gas, and K is the so-called Langmuir “constant.” This equation has variously been referred to as the single-site Langmuir model, the monolayer Langmuir model, or simply the Langmuir isotherm equation. However, it is important to note that this was not the only equation to be proposed by Langmuir (e.g., Langmuir also developed a multilayer variant in 1918 that was later improved upon and has become widely known as the BET model).^{3,4} Beyond Langmuir’s contributions, other adsorption equations have been proposed and developed.⁵ A distinct advantage of the Langmuir-type models is that they can be derived from first principles using statistical mechanics,⁶ enabling a direct method for determining the inherent temperature dependence of the Langmuir equation. All in all, the SL

equation is a practical starting point for experimental adsorption analysis, from simple data interpolation to determination of key metrics such as the number of adsorption sites per unit mass (which can be directly related to the gas-accessible surface area, when it can be assured that only a monolayer of adsorbate is formed).

The SL equation and the more complex Langmuir models related to it are widely used for gas adsorption analysis, particularly to assist in the determination of thermodynamic properties such as the isosteric enthalpy of adsorption.⁷ The latter analysis requires the measurement of multiple adsorption isotherms at different temperatures, fitting the collection of isotherms to a single model, and extracting relevant thermodynamic properties. Given this process, the inherent temperature dependence of the model plays a critical role. However, this topic is rarely explored. Instead, many researchers simply fit each of their measured isotherms independently with a separate Langmuir equation for each one, rather than using a global model that fits all of the measured isotherms to one set of fitting parameters. This results in a large superset of resulting parameters that require additional analysis to reconcile into meaningful materials properties. This raises an important question: why do researchers avoid the use of an explicit temperature-dependent model?

One explanation is that not all adsorption systems, even those that follow the SL model very closely, exhibit the same temperature dependence. In fact, the temperature dependence can vary across different condition regimes and is strongly influenced by the inherent properties of the system⁸. Furthermore, multiple atomistic pictures of the adsorption site can lead to the same temperature dependence but for different reasons, complicating the interpretation of the T-dependence. Ultimately, an entire subset of adsorption equations underlies the above general SL

equation, each attributing a unique temperature dependence to the adsorption system. While efforts have been made to systematically organize these equations,^{9,10} a comprehensive framework remains lacking.

In this work, we employ a simple, empirical approach to elucidate the T-dependence of the SL equation for a model adsorption system by fitting a diverse range of equations to an experimental data set in order to better understand which model is most accurate. We present a systematic list of physically justifiable models, each rooted in a simple microscopic interpretation of the adsorption site. All models satisfy the above general Langmuir equation while providing insights into the temperature dependence of K according to:

$$n_a [T, P] = n_s \frac{K[T]P}{1 + K[T]P} \quad \text{Eq. 2}$$

The results of this systematic approach reveal new insights into the role of the T-dependence of the Langmuir model in determining thermodynamics properties of experimental adsorption systems such as the binding strength (or binding energy) and isosteric heat of adsorption.

Theory

Gibbs Excess Adsorption

All experimental adsorption measurements have the simple issue of not being able to directly assess the “absolute” (actual) adsorbed amount. J. Willard Gibbs realized this and hence the experimental quantity measured is referred to as the Gibbs “excess” amount: the amount beyond what would be expected in the same volume if no adsorbent were present.¹¹ The difference between the absolute and excess amounts is significant at higher pressures and colder

temperatures, where the bulk adsorbate fluid density approaches that of the adsorbed phase. The relationship between the excess and absolute amounts adsorbed is:

$$n_e = n_a - \rho_g V_a \quad \text{Eq. 3}$$

where n_e is the experimentally measured excess adsorbed amount, n_a is the actual or “absolute” adsorbed amount, ρ_g is the density of the bulk adsorbate fluid, and V_a is the volume of the adsorbed phase.

It is usually important to distinguish between n_e and n_a since the difference could be significant. However, when the conditions of adsorption are sufficiently dilute in the gas phase (i.e., $\rho_g \approx 0$ or $\rho_a \gg \rho_g$), it is convenient to be able to ignore the role of V_a since it is not experimentally measurable, and to thereby assume that $n_e \approx n_a$. In order to assess whether the difference between the experimentally measured adsorbed amount and the actual adsorbed amount is significant, a simple test can be performed. If the crystals of solid (porous) adsorbent are reasonably large, an approximate upper limit of V_a is the total pore volume, V_{tot} . By multiplying V_{tot} and the maximum gas-phase density of the adsorbate under the conditions explored, a maximum correction term to the absolute adsorbed amount can be approximated (see Supporting Information). For the experimental data collected in this work, that value was determined to be within the experimental error and hence the correction term is negligible under all conditions and $n_e \approx n_a$. Henceforth, the raw (as-measured) excess adsorption equilibria will be treated as absolute adsorption quantities for all further analysis herein.

Langmuir Theory

Following Langmuir’s approach, the three measured quantities at each point of adsorption equilibrium (adsorbed amount, n_a , pressure, P , and temperature, T) are related by a

collection of fixed parameters that describe the nature of the adsorbent surface. Once known, these parameters can then be used to derive any desired thermodynamic information related to the experimental adsorption system. The simplest possible case is a surface comprising a collection of identical and independent binding sites, each hosting a single adsorbate molecule, giving rise to the general SL adsorption model given by Equation 2. A simpler form defines the concept of fractional site occupancy, θ , as:

$$\theta[T, P] = \frac{n_a}{n_a + n_{empty}} = \frac{n_a}{n_s} = \frac{K[T] P}{1 + K[T] P} \quad \text{Eq. 4}$$

The Langmuir constant, $K[T]$, has both an exponential “Boltzmann factor” term (related to the energy of adsorption, which is identical at each site, ε)^{5,6} as well as a possible temperature dependence in the pre-exponential term, referred to herein as $A[T]$:

$$K[T] = A[T] e^{-\frac{\varepsilon}{RT}} \quad \text{Eq. 5}$$

where R is the gas constant.

Langmuir Pre-Factor

The precise form of $A[T]$ can be derived using statistical mechanics in the grand canonical formalism¹² and varies depending on the treatment of the degrees of freedom of the adsorbate on the adsorption site. For simplicity, we briefly treat two extreme cases (all intermediate cases are thoroughly treated in the Supporting Information): “fixed” adsorption (where the adsorbate loses all translational degrees of freedom upon adsorption) and the “Einstein crystal” adsorbed phase (where each adsorbate is bound to its site by harmonic oscillator type bonds in all three spatial dimensions). In the former case, the final result for the pre-factor is:

$$A_{Fix}[T] = \frac{h^3}{(2\pi\tilde{m})^{1.5} (k_B T)^{2.5}} \propto T^{-2.5} \quad \text{Eq. 6}$$

where h is Planck's constant, \tilde{m} is the mass of the adsorbate, and k_B is Boltzmann's constant.

This form of $A[T]$ does not contain any “loose” fitting parameters and so is simply a constant for a given adsorbate at a given temperature. The temperature dependence is significant: $\propto T^{-2.5}$.

Hence this model is also referred to as “model -2.5 ”. On the other hand, in the “Einstein crystal” case (the other extreme of cases investigated in this work), the final result for the pre-factor is:

$$A_{Ein}[T] = \frac{(2\pi)^{1.5} (k_B T)^{0.5}}{\tilde{m}^{1.5} \omega_s^3} \propto T^{+0.5} \quad \text{Eq. 7}$$

where ω_s is the natural frequency of the harmonic oscillation (taken to be identical in all three spatial dimensions), a “loose” fitting parameter that is temperature invariant but must be determined experimentally for a given system. The temperature dependence is significantly less and inversely correlated compared to the fixed model: $\propto T^{+0.5}$. Hence this model is also referred to as “model $+0.5$ ”.

A third important case is where the adsorbate retains three translational degrees of freedom upon adsorption but only two of which are harmonic oscillator type motion, while the third is constrained by an infinite square-well potential. This case does not have an easily justifiable physical picture, but has an important outcome for the pre-exponential factor (see Supporting Information for more details):

$$A_0[T] = \frac{2\pi L_s}{\tilde{m} \omega_s^2} \propto T^0 \quad \text{Eq. 8}$$

where ω_s is the natural frequency of the harmonic oscillation (taken to be identical in both of the first two dimensions of freedom) and L_s is the length of the potential well in the third dimension

of freedom. This form of $A[T]$ is independent of temperature: $\propto T^0$. Hence this model is also referred to as “model 0”.

Different physical pictures and the corresponding degrees of freedom of each lead to different temperature dependencies of $A[T]$ at intervals of $T^{0.5}$ from $T^{-2.5}$ to $T^{+0.5}$. Likewise, each leads to a different high-temperature heat capacity of the adsorbed phase, as expected based on the equipartition theorem.¹² All such models are simplistic in nature, much like the Einstein model of monatomic crystals, and may not be realistic for any experimental system; nevertheless, they provide a toolbox for exploring the effects of the temperature-dependent pre-factor on the resulting Langmuir adsorption model. The explicit forms of $A[T]$ for each case explored herein are given in the Supporting Information (Table S1) and the properties of a subset of highest importance are summarized in Table 1.

Table 1. Six important adsorption models explored herein, and their temperature dependence of the pre-exponential factor in the Langmuir constant, high-temperature limit heat capacity, and number of degrees of freedom. Further details are provided in Table S1.

Physical Picture	Adsorption Site Partition Function ($x \times y \times z$)	Adsorbate Degrees of Freedom	High T Heat Capacity ($k_B T$)	$A[T]$
Fixed	DF \times DF \times DF	0	$0 + 0 + 0 = 0$	$\frac{\text{constant}}{T^{2.5}}$
1D Ideal Gas	SP \times DF \times DF	1	$0.5 + 0 + 0 = 0.5$	$\frac{\text{constant}}{T^2}$
2D Ideal Gas	SP \times SP \times DF	2	$0.5 + 0.5 + 0 = 1$	$\frac{\text{constant}}{T^{1.5}}$
3D Ideal Gas	SP \times SP \times SP	3	$0.5 + 0.5 + 0.5 = 1.5$	$\frac{\text{constant}}{T^1}$
2D Lattice Gas	QP \times QP \times DF	2	$1 + 1 + 0 = 2$	$\frac{\text{constant}}{T^{0.5}}$
(no physical picture)	QP \times QP \times SP	3	$1 + 1 + 0.5 = 2.5$	constant

Note: potential function descriptions along each spatial dimension (x, y, or z) are abbreviated as: DF for delta function, SP for infinite square-well potential, and QP for quadratic potential.

Experimental Methods

Materials Synthesis

A metal-organic framework (MOF) of composition $[\text{Ni}_3(\text{pzdc})_2(\text{ade})_2(\text{H}_2\text{O})_4] \cdot 2.18 \text{ H}_2\text{O}$ (where “pzdc” is pyrazole-3,5-dicarboxylic acid and “ade” is adenine) was synthesized according to the previously reported procedure.¹³ The material was degassed under high vacuum at 130 °C for 12 h to obtain the dried composition of $\text{Ni}_3(\text{pzdc})_2(\text{ade})_2(\text{H}_2\text{O})_4$ prior to further analyses (referred to herein simply as “MOF”, shown in Figure 1); the MOF powder is sky blue prior to activation and turns lavender when fully dried. The phase purity of the sample was confirmed using powder X-ray diffraction (Figure S1).

Materials Characterization

Powder X-ray diffraction was measured under ambient conditions using a benchtop X-ray diffractometer (D2 Phaser, Bruker Corp.) with Cu K $\alpha_{1,2}$ radiation in reflection geometry.

Nitrogen (99.999%) adsorption/desorption uptake was measured using an automated Sieverts apparatus (3Flex, Micromeritics Corp.); the sample (dry mass: 0.344 g, skeletal density: 2.5 g mL⁻¹) was held in a liquid nitrogen bath (the boiling temperature of N₂ is 75.9 K in Bozeman, Montana). The surface area was estimated using the Brunauer-Emmett-Teller (BET) model, employing the Rouquerol consistency criteria.¹⁴ The pore size distribution was determined using a non-local density functional theory (NLDFT) slit pore model (implemented using Micromeritics MicroActive software).

Hydrogen Adsorption Measurements

Hydrogen (99.9999%) adsorption/desorption uptake was measured using an automated Sieverts apparatus (3Flex, Micromeritics Corp.). The sample (dry mass: 0.344 g, skeletal density: 2.5 g mL⁻¹) was held in the cold well of a closed-cycle helium refrigerated cryostat (CH-104, ColdEdge Technologies). The sample temperature was measured using a silicon diode (DT-670C, Lake Shore Cryotronics) and calibrated (indicating an offset of 1.4 K) using boiling liquid nitrogen (75.9 K) as a reference (Figure S2).

Structure Analysis

Structural modeling of the MOF pore network was performed using two dedicated software packages: CrystalMaker (v. 10.8.2) and Zeo++ (v. 0.3). The probe radius used to determine the accessible volume was 1.2 Å.

Results and Discussion

Model System Selection

To properly investigate the temperature dependence of the Langmuir model, it is essential to use a homogeneous adsorption system that fulfills the fundamental assumptions inherent to the SL equation. Hydrogen (H_2) is an ideal candidate for this purpose, as it is one of the weakest interacting molecular adsorbates (with the exception of helium, which presents significant experimental challenges since it is used as the de facto free space probe in most laboratories). This ensures the smallest perturbation to the porous adsorbent structure upon binding, satisfying a critical aspect of Langmuir's theory that the underlying structure of the adsorbent remains unchanged during binding. The ideal adsorbent for such studies must also exhibit rigidity, stability, and lack of any strong (chemisorption) binding sites. Most importantly the ideal adsorbent material should possess distinct, periodic, and disparate binding sites that validate the key assumptions of distinguishable, identical, and non-interacting sites, respectively.

A crystalline MOF with one binding site per cage and per unit cell is a desirable adsorbent for applications of the SL equation. This material should have narrow pores to prevent multilayer adsorption and disparate binding sites to prevent cooperative binding. A porous material is particularly desirable since it provides a high adsorption capacity relative to the mass of the adsorbent, enhancing the signal to noise ratio in the measurements. Previous reports of Xe adsorption on SBMOF-1 meet these criteria,¹⁵ but Xe is significantly more polarizable than H_2 . Many traditional porous adsorbents fail to qualify as model materials for H_2 due to the heterogeneity of the surface toward such a small molecular adsorbate. For example, even

platinum, a classic surface for H₂ adsorption, exhibits heterogeneity with two distinct sites depending on the facet exposed.¹⁶

In this work, a nickel-based MOF with ~ 7 Å pores and ~ 200 m² g⁻¹ surface area (Ni₃(pzdc)₂(ade)₂(H₂O)₄) was identified as an ideal porous material that satisfies the assumptions of the SL equation toward H₂ adsorption.¹³ The MOF features distinct, homogeneous binding sites that can accommodate a single H₂ molecule per site (Figure 1). Importantly, the adsorption mechanism is purely physisorptive, with minimal contribution from the Ni metal centers.¹⁷ The synthesis and characterization of the MOF were performed as previously reported, and a homogeneous pore-size distribution was confirmed (Figure 1d).

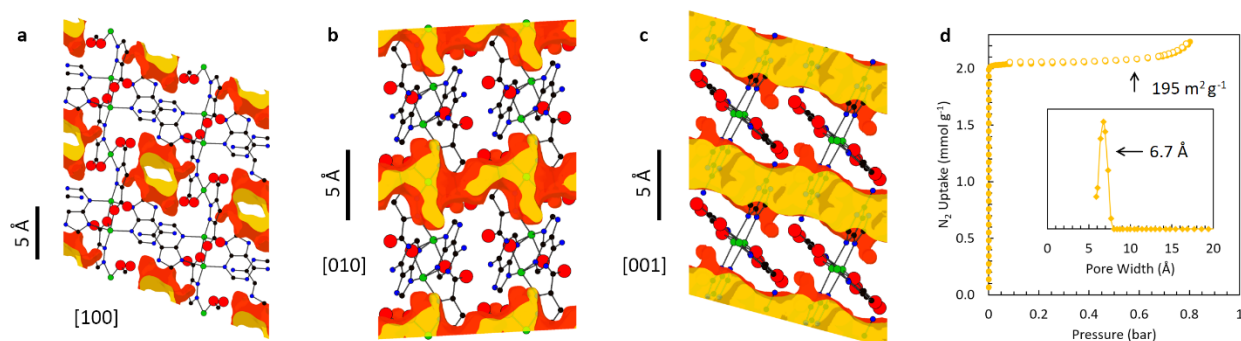


Figure 1. (a-c) Crystal structure of the single-site MOF (Ni₃(pzdc)₂(ade)₂(H₂O)₄) showing the one-dimensional channels in yellow that are perpendicular to the one-dimensional Ni-pzdc-ade chains. (d) N₂ adsorption/desorption isotherms at ~ 77 K showing its NLDFT pore size of ~ 7 Å and BET surface area of 195 m² g⁻¹.

Hydrogen Adsorption Uptake

Excess H₂ uptake equilibria (measured in mmol g⁻¹) as a function of pressure (in bar) and temperature (in K) were measured along four isotherms between 70-100 K using the volumetric technique (Figure 2). The excess uptake quantities were converted into absolute uptake by neglecting the contribution of the correction term (see the Supporting Information for the

justification of this approach under the conditions explored herein). Adsorption equilibria for further analysis were selected by truncating each isotherm at near the completion of a monolayer, beyond which adsorption occurs primarily on the outer surfaces of the particles. These selected adsorption equilibria were tabulated, imported into a Python package (Realist, v. 0.314¹⁸), and globally fitted to a series of SL equations of the general form shown in Equations 4-5.

Specifically, the temperature dependence of the pre-exponential factor in Equation 5 (referred to herein as $A[T]$) was varied by powers of 0.5 from -2.5 to 0 (some additional experiments are also described in the Supporting Information). This analysis culminated in six total fits, each characterized by a unique set of fitting parameters. The results of the fitting procedure, including the best-fit parameters and the goodness of fit (determined herein as the root of the sum of the squared residuals per data point, or RMSE), are summarized in Figure 3 and tabulated in Table 2.

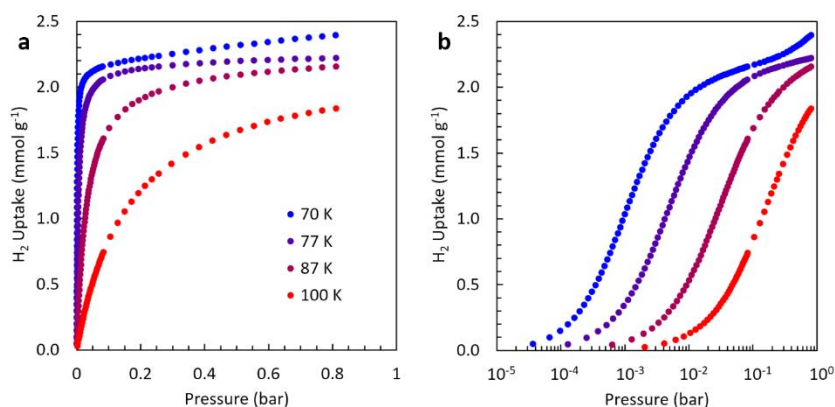


Figure 2. Equilibrium excess adsorption uptake of H₂ on Ni₃(pzdc)₂(ade)₂(H₂O)₄ between 70-100 K and 0-1 bar with: (a) normal and (b) logarithmic pressure axes.

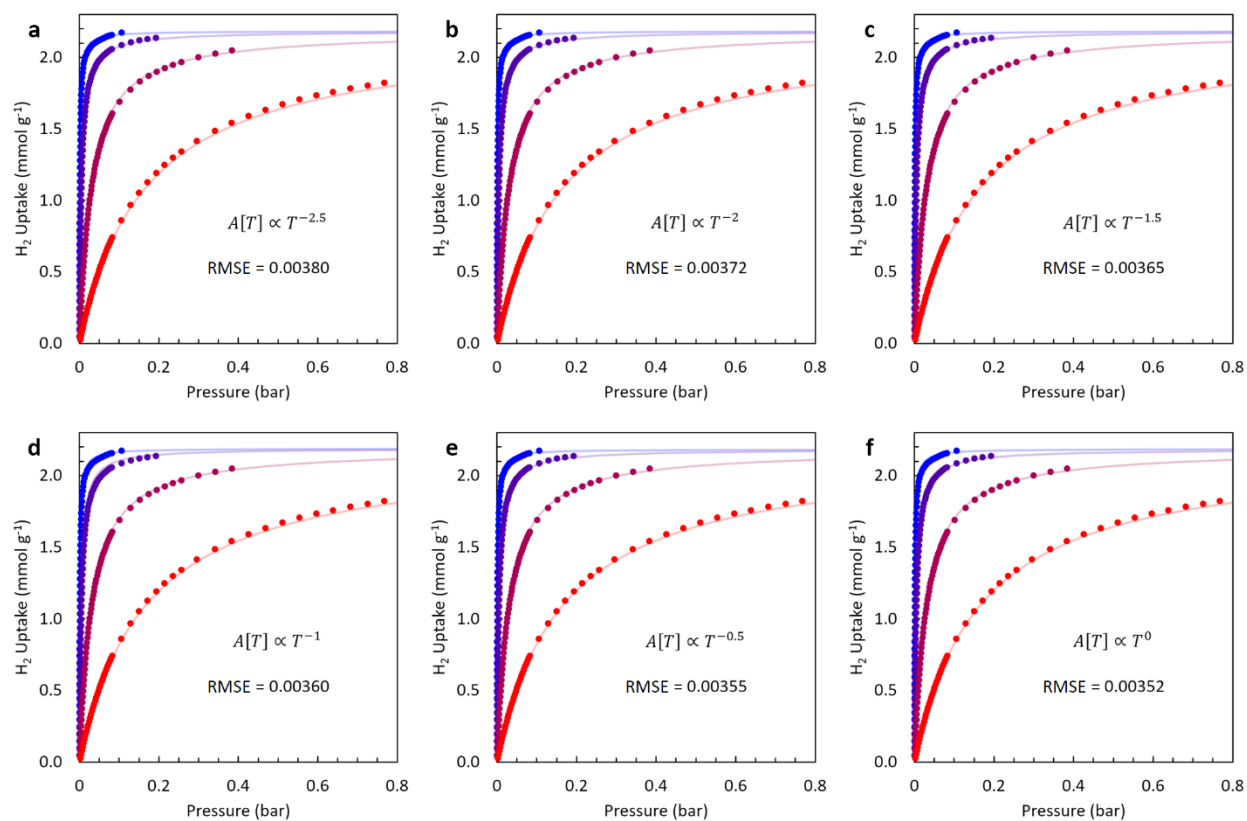


Figure 3. Equilibrium excess uptake (circles) of H₂ on Ni₃(pzdc)₂(ade)₂(H₂O)₄ between 70-100 K and 0-1 bar fitted by a series of SL equations (lines) with varying temperature dependencies: $A[T] \propto$ (a) $T^{-2.5}$ to (f) T^0 . Goodness of fit (RMSE) is indicated. Isotherm temperature is indicated by color from red (70 K) to blue (100 K).

The optimized fits of the experimental adsorption equilibria to the six models exhibited nearly identical goodness of fit, despite each model representing a different atomistic description of the single binding site. In general, all models provided a good fit to the experimental data, as confirmed by both statistical analysis and visual inspection (Figure 3). The goodness of fit systematically improved as the T-dependence of the pre-exponential factor varied from a large negative power (i.e., $T^{-2.5}$) to T-independent (i.e., T^0) (Table 2), but this was only a very small effect. In contrast to the small difference in goodness of fit between each model, the respective

binding energies varied systematically and significantly from ~ 10 to ~ 8 kJ mol⁻¹, from $T^{-2.5}$ to T^0 , respectively.

Hence, the results of this study imply that a nearly identical goodness of fit can be achieved while attributing widely varying binding energies to the adsorption event; a difference of 2 kJ mol⁻¹ is experimentally and computationally meaningful, at high levels of theory¹⁹. The meaning of the fitting parameters also differs widely depending on the model chosen (see Supporting Information). Interestingly, all best-fit values of the various fitting parameters were found to be physically reasonable for H₂ on Ni₃(pzdc)₂(ade)₂(H₂O)₄, further preventing any strong discrimination against any of the models used herein. In other words, no single model with a specific temperature dependence could be unambiguously declared as the “best model” to describe H₂ adsorption on the single-site MOF at between 70-100 K.

Thermodynamic Analysis

An important practical metric for adsorption systems that is widely reported in the adsorption literature is the isosteric enthalpy (or “heat”) of adsorption ($-\Delta_{ads}H$ or q_{st}). This value is often used as a proxy to describe the average interaction energy or strength of binding of the adsorption system, often as a function of surface occupancy. In some cases, q_{st} , is also reported as a function of both temperature and surface occupancy,^{20,21} requiring a more sophisticated modeling approach with an explicit temperature dependence built into the fitting model. Although the isosteric enthalpy can, in principle, be measured directly using calorimetry, such measurements are far less common than indirect determination via fitting measured adsorption equilibria. In this work, the isosteric enthalpy of adsorption is calculated as a function of both temperature and surface occupancy for each adsorption model using the widely

employed Clausius-Clapeyron equation (which requires two assumptions to be validated, see the Supporting Information) as shown below:

$$q_{st}[T, P] = -\Delta_{ads}H[T, P] = \frac{RT^2}{P} \left(\frac{\partial P}{\partial T} \right)_\theta \quad \text{Eq. 9}$$

The explicit form of the partial derivative in Equation 9 is directly influenced by the T-dependence inherent in the chosen adsorption model, as shown in the Supporting Information. This is the same relation employed in almost all efforts to deduce q_{st} from adsorption uptake equilibria, whether an explicit model is employed or not.

In the present work, the isosteric enthalpy of adsorption is invariant with respect to surface occupancy (θ) owing to two key assumptions: (1) a homogeneous binding site distribution on the adsorbent surface and (2) the treatment of the bulk adsorbate as an ideal gas. However, depending on the model chosen (i.e., the treatment of degrees of freedom in the binding site itself), the isosteric enthalpy of adsorption can be anything from invariant with temperature to highly sensitive to temperature. Two extreme cases are the “fixed” adsorption site model (where the adsorbate loses all translational degrees of freedom upon adsorption and $A_{Fix}[T] \propto T^{-2.5}$) and a looser-bound adsorption site (where each adsorbate can access 3 degrees of freedom and $A_0[T] \propto T^0$). In the former case, the final result for the isosteric heat of adsorption is:

$$q_{st,Fix}[T] = -(\varepsilon - 2.5RT) \quad \text{Eq. 10}$$

On the other hand, in “model 0” the final result for the isosteric heat of adsorption is:

$$q_{st,0}[T] = -\varepsilon \quad \text{Eq. 11}$$

The isosteric heats of all models can be described by a simple relation:

$$q_{st,x}[T] = -(\varepsilon - xRT) \quad \text{Eq. 12}$$

where x is the (positive) exponent of T in the denominator of $A[T]$. All of the above equations are valid in the ideal gas limit only.

The isosteric heats of adsorption of H_2 on $\text{Ni}_3(\text{pzdc})_2(\text{ade})_2(\text{H}_2\text{O})_4$, according to the results of six different SL models, are shown in Figure 4. Despite nearly identical goodness of fit across all models, it is evident that the choice of model is of great importance to the interpretation of the adsorption thermodynamics. For example, the model with the best fit by a slight margin (“model 0”, $\text{RMSE} = 0.00352$) would suggest that the isosteric heat is temperature invariant (Figure 4f) while the model with the marginally worst fit (“model -2.5”, $\text{RMSE} = 0.00380$) would suggest that the isosteric heat increases by 0.6 kJ mol^{-1} between 70-100 K (Figure 4a). While this $+0.6 \text{ kJ mol}^{-1}$ variance is small within the 30 K temperature range explored in this work, this would increase to a discrepancy of $+4.8 \text{ kJ mol}^{-1}$ over a wider range of 70-298 K, a temperature range of importance for applications. Whether the isosteric heat changes by 5 kJ mol^{-1} within this temperature range or not is still a subject of ongoing investigation, but clearly this would be of major technological significance. It is clear from this work that the experimental data alone cannot unambiguously be used to determine the temperature dependence of the isosteric heat since all models give a similar goodness of fit.

Table 2. Best-fit parameters for six models of H₂ adsorption on Ni₃(pzdc)₂(ade)₂(H₂O)₄ according to SL equations with different T-dependence of the pre-exponential factor, $A[T]$.

	n_s (mmol g ⁻¹)	<i>constant</i> (K ^x bar ⁻¹)	ε (kJ mol ⁻¹)	$\Delta_{ads}H$ at 82 K (kJ mol ⁻¹)	RMSE
Fixed ($T^{-2.5}$)	2.19(1)	408(13)	-7.97(2)	-9.71	0.00380
1D Ideal Gas (T^{-2})	2.19(1)	27.0(2)	-8.31(2)	-9.72	0.00372
2D Ideal Gas ($T^{-1.5}$)	2.19(1)	1.79(5)	-8.66(2)	-9.72	0.00365
3D Ideal Gas (T^{-1})	2.19(1)	0.119(3)	-9.01(2)	-9.72	0.00360
2D Lattice Gas ($T^{-0.5}$)	2.19(1)	0.0079(2)	-9.35(2)	-9.75	0.00355
QQQPSP* (T^0)	2.19(1)	0.00052(1)	-9.70(2)	-9.74	0.00352

*Note: there is no name or reasonable “physical picture” for this model (see Supporting Information)

Average Temperature Isostatic Heat

The calculated isosteric enthalpy of adsorption varies significantly across the different models explored in this study (Figure 4), despite that there is no significant difference between the goodness of fit for the different models. Notably, however, the calculated isosteric enthalpy of adsorption at the average temperature of measurement (defined herein as the thermodynamic average, or the average of $1/T$) remains consistent across all the models explored. This effect is shown in Figure 5, where the isosteric enthalpy of adsorption at the average temperature of 82 K for the four isotherms is identical for all models. This finding is an important result as it demonstrates that, regardless of the specific model employed, an unambiguous outcome of adsorption modeling is the value of the isosteric heat at the thermodynamic average temperature over the temperature range explored. We recommend that researchers seeking to determine the

isosteric enthalpy of adsorption at a given process temperature collect a large set of data around their temperature of interest, ensuring that this temperature corresponds to the average of the experimental temperature set. While the binding energy reported by the best fit will not be unambiguously true, nor will the temperature dependence of q_{st} , the value of the q_{st} at the average temperature will be a reliable metric for further analysis. For H_2 adsorption on $\text{Ni}_3(\text{pzdc})_2(\text{ade})_2(\text{H}_2\text{O})_4$, the isosteric heat of adsorption (which we expect would be corroborated by calorimetry) at 82 K is found to be 9.7 kJ mol^{-1} . Interestingly, this “average temperature” heat of adsorption is the same deliverable that is possible to achieve using non-temperature-dependent methods such as individual isotherm fitting, but with far fewer fitting parameters in this case.

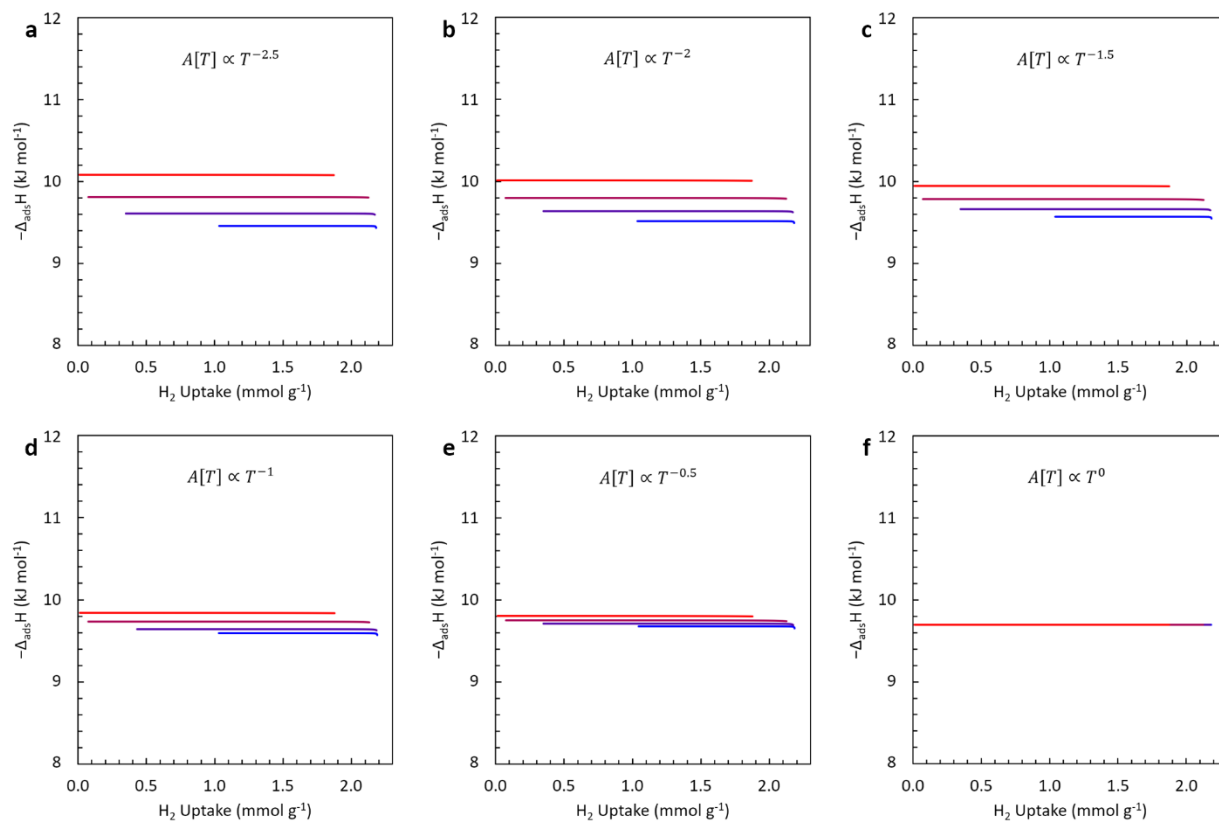


Figure 4. Isosteric enthalpy of adsorption of H_2 on $\text{Ni}_3(\text{pzdc})_2(\text{ade})_2(\text{H}_2\text{O})_4$ between 70-100 K and 0-1 bar based on a series of SL equations with varying temperature dependencies: $A[T] \propto T^{-2.5}$ to (f) T^0 . Isotherm temperature is indicated by color from red (70 K) to blue (100 K).

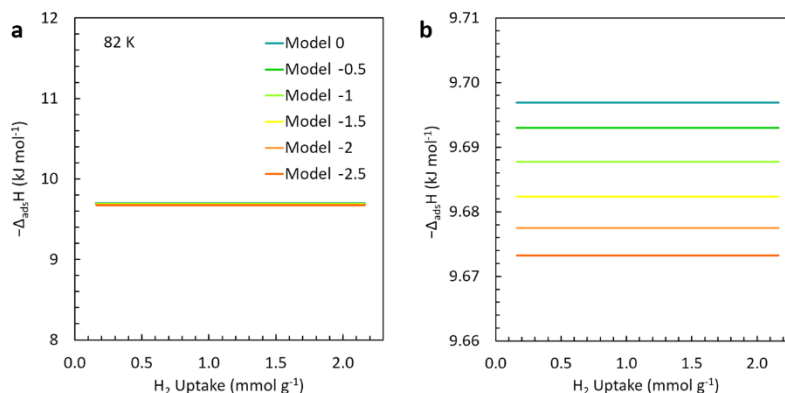


Figure 5. Isosteric enthalpy of adsorption of H_2 on $\text{Ni}_3(\text{pzdc})_2(\text{ade})_2(\text{H}_2\text{O})_4$ at 82 K and 0-1 bar based on a series of SL equations with varying temperature dependencies: $A[T] \propto T^{-2.5}$ to T^0 .

Conclusions

Hydrogen adsorption was measured on a metal-organic framework ($\text{Ni}_3(\text{pzdc})_2(\text{ade})_2(\text{H}_2\text{O})_4$) with crystallographically identical binding sites between 70-100 K. The adsorption equilibria were then globally fitted to a series of single-site Langmuir (SL) equations with different inherent treatments of the temperature dependence. This approach allowed for the characterization of the adsorption system across the entire temperature range using only three fitting parameters in all cases, as opposed to fitting each isotherm independently, which would have required three fitting parameters per isotherm. Furthermore, it enabled a rigorous intercomparison of different sub-variants of the SL equation, each representing a unique atomistic picture of the adsorption site and therefore a distinct temperature dependence. The choice of $\text{Ni}_3(\text{pzdc})_2(\text{ade})_2(\text{H}_2\text{O})_4$ as a model adsorbent for this study was based on its structure, which features identical, independent hydrogen binding sites that accommodate only a single hydrogen molecule per site.

In this study, we found that as the temperature dependence was allowed to vary widely, corresponding to significantly different physical pictures of the adsorption site, the overall goodness of fit remained largely unchanged, and the differences in the results from fit to fit were not observable by eye. However, the slight variation in model choice resulted in notable disparities in binding energy and the temperature dependence of the isosteric heat of adsorption. In the narrow temperature range explored (a window of 30 K), this amounted to $\sim 2 \text{ kJ mol}^{-1}$ differences in the attributed binding energies (a measurable difference of technological importance) and 0.6 kJ mol^{-1} differences in the isosteric heats at high and low temperature. Despite these differences, the isosteric heat of adsorption at the average temperature studied (82

K) was found to be consistent across all models. This suggests that when researchers are uncertain, they should prioritize selecting a fitting model that accurately fits their data and then report the isosteric enthalpy of adsorption (as opposed to the binding energy) as a reliable finding, particularly at the average temperature of study.

Associated Content

Acknowledgements

We thank Cullen Quine for assistance with implementing the Realist software package. We gratefully acknowledge support for this work from the U.S. Department of Energy's Office of Energy Efficiency and Renewable Energy (EERE) under award number DE-EE0008815, as well as from the College of Science at Oregon State University via the Industrial Award (2024).

Supporting Information

Absolute Adsorption Approximation: The maximum correction term in Equation 3 in the main text ($\rho_g V_a$) was determined by assuming that the maximum adsorbed phase volume is equal to the total pore volume of the adsorbent. For the MOF used in this study, $\text{Ni}_3(\text{pzdc})_2(\text{ade})_2(\text{H}_2\text{O})_4$, the total pore volume accessible to H_2 was calculated using a standard software package (Zeo++) using the experimentally determined crystal structure (measured by K. C. Stylianou et al.[S1]) and a probe radius of 1.2 Å (corresponding to H_2); it was found to be 0.119 mL g⁻¹. Furthermore, the densest gas phase of hydrogen encountered under the experimental conditions explored in this work (calculated using NIST Refprop) was 0.139 mmol mL⁻¹ at 70 K and 810 mbar.

By combining these two quantities, the maximum possible correction term is 0.0166 mmol g⁻¹ which is ~0.7% of the measured (excess) uptake quantity at 70 K and 810 mbar. This is below the standard error associated with the measurement and is hence negligible.

Clausius-Clapeyron Approximation: In general, adsorption equilibria obey the Clapeyron equation which is a general relation for any two phases in thermal and mechanical equilibrium:

$$\Delta_{ads}H[T, P] = T \Delta_{ads}S = T \left(\frac{\partial P}{\partial T} \right)_\theta \Delta_{ads}v = T \left(\frac{\partial P}{\partial T} \right)_\theta (v_a - v_g)$$

When one of the two phases in equilibrium is an ideal gas and the other is a condensed phase (e.g., an adsorbed phase), it is common to employ an approximation that the condensed phase molar volume is negligible compared to the gas and thus derive the Clausius-Clapeyron subvariant:

$$q_{st}[T, P] = -\Delta_{ads}H[T, P] = \frac{RT^2}{P} \left(\frac{\partial P}{\partial T} \right)_\theta$$

The above equations can be explicitly solved for all of the models explored in this work, each giving rise to a specific form of the partial derivative and therefore a specific relationship between the fitting parameters and the isosteric enthalpy of adsorption. These relationships are summarized in Equation 12 in the main text.

Powder X-Ray Diffraction Analysis: The phase purity of Ni₃(pzdc)₂(ade)₂(H₂O)₄ was assessed by powder X-ray diffraction (XRD) methods, as shown in Figure S1.

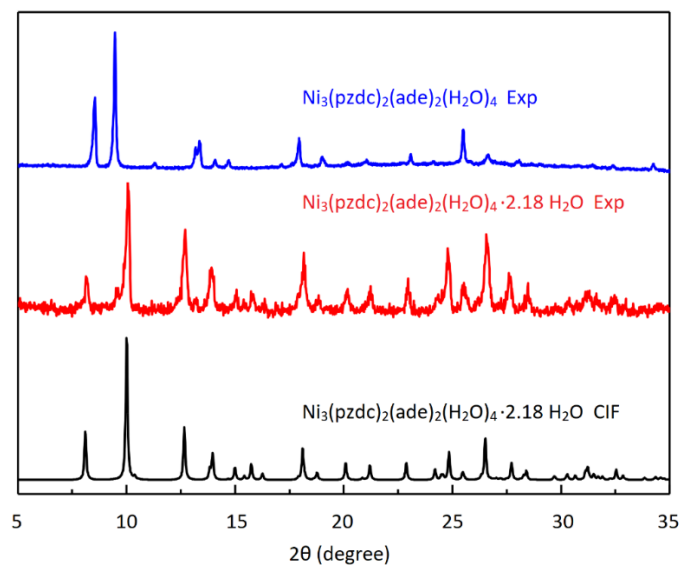


Figure S1. XRD pattern of $\text{Ni}_3(\text{pzdc})_2(\text{ade})_2(\text{H}_2\text{O})_4$ and $\text{Ni}_3(\text{pzdc})_2(\text{ade})_2(\text{H}_2\text{O})_4 \cdot 2.18 \text{H}_2\text{O}$ compared to a simulated pattern (based on the single-crystal XRD structure of $\text{Ni}_3(\text{pzdc})_2(\text{ade})_2(\text{H}_2\text{O})_4 \cdot 2.18 \text{H}_2\text{O}^{[S1]}$).

Cryostat Temperature Calibration: The cryostat temperature was calibrated by comparison to boiling nitrogen, as shown in Figure S2.

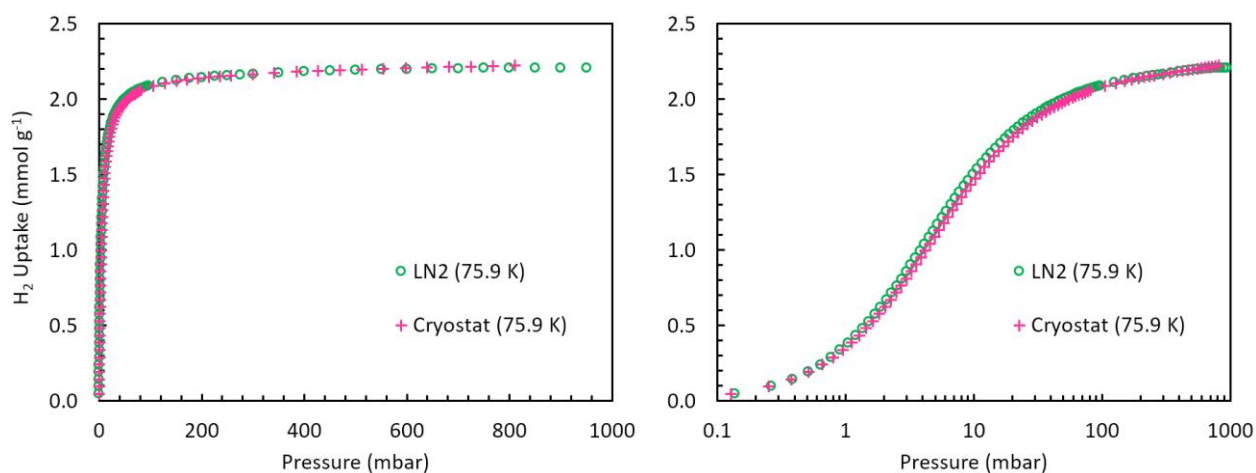


Figure S2. Equilibrium excess adsorption uptake of H_2 on $\text{Ni}_3(\text{pzdc})_2(\text{ade})_2(\text{H}_2\text{O})_4$ in a liquid nitrogen bath (N_2 boils at 75.9 K in Bozeman, Montana) and at the same set-point using a cryostat (75.9 K).

Langmuir Adsorption Theory: In the “classic” (also known as the single-site monolayer)

Langmuir model, there are three simple assumptions used to define the adsorption system:

1. Every adsorption site is identical, independent, and distinguishable (hence “single-site”)
2. Each adsorption site can accommodate up to 1 adsorbate molecule (hence “monolayer”)
3. The chemical reservoir is an ideal gas

The third assumption is necessary to obtain the classic Langmuir equation from first principles, but is not always strictly ensured by the system of study. In this case, the conditions investigated experimentally meet the criteria to be considering suitably ideal (see Clausius-Clapeyron Approximation above). Therefore, if the adsorbent is crystalline and contains identical sites that can host only a single adsorbate per site, the adsorption isotherm will be described by the Langmuir model.

When held in contact with a thermal reservoir (held at temperature T) and a chemical reservoir (held at chemical potential μ), a single such adsorption site has the following grand canonical partition function (owing to two possible states, empty or singly occupied, according to the first assumption):

$$\xi[\beta, \beta\tilde{\mu}] = \sum_{i \text{ (states)}} q_i e^{-\beta E_i} e^{\beta\tilde{\mu} N_i} = 1 + q[\beta] e^{-\beta\epsilon} e^{\beta\tilde{\mu}}$$

$$\beta = \frac{1}{k_B T}$$

$$\beta\tilde{\mu} = \frac{\tilde{\mu}}{k_B T} = \frac{1}{k_B T} \left(\frac{\partial G}{\partial N} \right)_{T,P}$$

In the above equations, q is the canonical partition function for the adsorbate when occupying the adsorption site, and ε is the binding energy (difference in energy between the bulk adsorbate and the bound adsorbate).

The total grand canonical partition function for the surface (containing N_s identical, independent, and distinguishable sites, according to the second assumption) is then:

$$\mathcal{Z}[\beta, \beta\tilde{\mu}] = \prod_{j \text{ (sites)}} \xi_j = \xi^{N_s} = (1 + q[\beta]e^{-\beta\varepsilon}e^{\beta\tilde{\mu}})^{N_s}$$

Finally, following the usual thermodynamic relations, the expectation value for the number of sites occupied, which is equivalent to the adsorption equation, is:

$$\langle N \rangle[\beta, \beta\tilde{\mu}] = N_s \cdot \frac{q[\beta] \cdot e^{-\beta\varepsilon} \cdot e^{\beta\tilde{\mu}}}{1 + q[\beta] \cdot e^{-\beta\varepsilon} \cdot e^{\beta\tilde{\mu}}}$$

This is much more commonly expressed in terms of the pressure of the chemical reservoir, P^* .

To do so requires invoking the third assumption. The chemical potential of an ideal (monatomic) gas is:

$$P^* = \frac{(2\pi\tilde{m})^{1.5} (k_B T)^{2.5}}{h^3} e^{\beta\tilde{\mu}}$$

Therefore:

$$\langle N \rangle[T, P^*] = N_s \cdot \frac{A[T] \cdot e^{\frac{\varepsilon}{k_B T}} \cdot P^*}{1 + A[T] \cdot e^{\frac{\varepsilon}{k_B T}} \cdot P^*}$$

The fractional occupancy is simply:

$$\theta[T, P^*] = \frac{\langle N \rangle}{N_s} = \frac{A[T] \cdot e^{\frac{\varepsilon}{k_B T}} \cdot P^*}{1 + A[T] \cdot e^{\frac{\varepsilon}{k_B T}} \cdot P^*}$$

The pre-exponential term, $A[T]$, varies depending on the treatment of the bound molecule on the adsorption site (see Table S1). We note that, in general, the form of $A[T]$ is independent of the nature of the ideal gas adsorbate (i.e., monatomic, diatomic, etc.), as long as the same internal degrees of freedom are retained in the adsorbed state as in the gas state.

Adsorption Site Descriptions and $A[T]$: To derive $A[T]$, an explicit form of $q[\beta]$ (i.e., $q[T]$) is needed. Four representative examples are explored below and a more systematic list is given in Table S1.

Fixed (i.e., “model -2.5”):

If the bound molecule has no degrees of freedom (the adsorption site is either “on” or “off”, “occupied” or “empty”), then the canonical partition functions of the adsorbed molecule in all three spatial dimensions are simply:

$$q_{DF}[\beta] = 0 + 1 = 1$$

In other words:

$$q_{Fix,x}[\beta] = q_{DF,x}[\beta] = 1$$

$$q_{Fix,y}[\beta] = q_{DF,y}[\beta] = 1$$

$$q_{Fix,z}[\beta] = q_{DF,z}[\beta] = 1$$

Together:

$$q_{Fix}[\beta] = q_{DF,x}[\beta] \times q_{DF,y}[\beta] \times q_{DF,z}[\beta] = 1 \times 1 \times 1 = 1$$

Then, following the statistical mechanics above:

$$\xi_{Fix}[\beta, \beta\tilde{\mu}] = 1 + e^{-\beta\varepsilon} e^{\beta\tilde{\mu}}$$

$$A_{Fix}[T] = \frac{h^3}{(2\pi\tilde{m})^{1.5} (k_B T)^{2.5}}$$

This is confirmed by using a more general approach which integrates over the entire potential experienced by the adsorbed molecule. For a perfectly fixed adsorbate, the potential is simply an inverted Dirac delta function (whose value is equal to the energy of adsorption, ε , at the origin and infinity everywhere else), centered at the adsorption site. The explicit details of this integration approach are given elsewhere.^[S2]

3D Ideal Gas (i.e., “model -1”):

If the bound molecule is treated as a particle in a box in all three spatial dimensions, then the individual partition functions are simply:

$$q_{SP}[\beta] = L \frac{\sqrt{2\pi\tilde{m}}}{h\sqrt{\beta}} = \frac{L}{\Lambda}$$

where:

$$\Lambda = \frac{h}{\sqrt{2\pi\tilde{m}k_B T}} = \frac{h\sqrt{\beta}}{\sqrt{2\pi\tilde{m}}}$$

In other words:

$$q_{3DI,x}[\beta] = q_{SP,x}[\beta] = \frac{L_x}{\Lambda}$$

$$q_{3DI,y}[\beta] = q_{SP,y}[\beta] = \frac{L_y}{\Lambda}$$

$$q_{3DI,z}[\beta] = q_{SP,z}[\beta] = \frac{L_z}{\Lambda}$$

Together:

$$q_{3DI}[\beta] = q_{SP,x}[\beta] \times q_{SP,y}[\beta] \times q_{SP,z}[\beta] = \frac{L_x}{\Lambda} \times \frac{L_y}{\Lambda} \times \frac{L_z}{\Lambda} = \frac{V_s}{\Lambda^3}$$

Then, following the statistical mechanics above:

$$\xi_{3DI}[\beta, \beta\tilde{\mu}] = 1 + \frac{V_s}{\Lambda^3} e^{-\beta\varepsilon} e^{\beta\tilde{\mu}}$$

$$A_{3DI}[T] = \frac{V_s}{k_B T}$$

This is also confirmed by using a more general approach which integrates over the entire potential experienced by the adsorbed molecule. For an adsorbate in a box, the potential along x is simply a square-well of width L_x (whose value is equal to the energy of adsorption, ε , in the box and infinity everywhere else), centered at the adsorption site. The explicit details of this integration approach are given elsewhere.^[S2]

Einstein Adsorbed Phase (i.e., “model +0.5”):

If the bound molecule is treated as a harmonic oscillator in all three spatial dimensions, then the individual partition functions are simply:

$$q_{QP}[\beta] = \frac{2\pi}{h\omega\beta}$$

In other words:

$$q_{Ein,x}[\beta] = q_{QP,x}[\beta] = \frac{2\pi}{h\omega_x\beta}$$

$$q_{Ein,y}[\beta] = q_{QP,y}[\beta] = \frac{2\pi}{h\omega_y\beta}$$

$$q_{Ein,z}[\beta] = q_{QP,z}[\beta] = \frac{2\pi}{h\omega_z\beta}$$

Together:

$$q_{Ein}[\beta] = q_{QP,x}[\beta] \times q_{QP,y}[\beta] \times q_{QP,z}[\beta] = \frac{2\pi}{h\omega_x\beta} \times \frac{2\pi}{h\omega_y\beta} \times \frac{2\pi}{h\omega_z\beta}$$

When all three dimensions are taken to have the same natural frequency of oscillation, ω_s :

$$q_{Ein}[\beta] = \left(\frac{2\pi}{h\omega_s\beta} \right)^3$$

Then, following the statistical mechanics above:

$$\xi_{Ein}[\beta, \beta\tilde{\mu}] = 1 + \left(\frac{2\pi}{h\omega_s\beta} \right)^3 e^{-\beta\varepsilon} e^{\beta\tilde{\mu}}$$

$$A_{Ein}[T] = \frac{(2\pi)^{1.5} (k_B T)^{0.5}}{\omega_s^3 (\tilde{m})^{1.5}}$$

This is confirmed by using a more general approach which integrates over the entire potential experienced by the adsorbed molecule. For a harmonic oscillator, the potential along x is simply a quadratic function with a minimum at ε (whose value is equal to $\varepsilon + \frac{1}{2}\tilde{m}\omega_x^2 x^2$), centered at the adsorption site. The explicit details of this integration approach are given elsewhere.^[S2]

2D Ideal Gas with z-Oscillation (i.e., “model -0.5”):

Instead of treating all three spatial dimensions as equivalent, other models can be developed that treat each dimension differently. For simplicity, the above three types of potential can be interchanged: inverted delta functions, square wells, or quadratic potentials. For example, if the bound molecule is treated as a particle in a 2D box (accounting for the two spatial dimensions along the surface of the adsorbent as square wells) and a harmonic oscillator in the direction orthogonal to the surface (treated as a quadratic potential, nominally in the z direction), then the individual partition functions are:

$$q_{2DO,x}[\beta] = q_{SP,x}[\beta] = \frac{L_x}{\Lambda}$$

$$q_{2DO,y}[\beta] = q_{SP,y}[\beta] = \frac{L_y}{\Lambda}$$

$$q_{2DO,z}[\beta] = q_{QP,z}[\beta] = \frac{2\pi}{h\omega_z\beta}$$

Together:

$$q_{2DO}[\beta] = q_{SP,x}[\beta] \times q_{SP,y}[\beta] \times q_{QP,z}[\beta] = \frac{L_x}{\Lambda} \times \frac{L_y}{\Lambda} \times \frac{2\pi}{h\omega_z\beta} = \frac{A_s}{\Lambda^2} \left(\frac{2\pi}{h\omega_s\beta} \right)$$

Then, following the statistical mechanics above:

$$\xi_{2DO}[\beta, \beta\tilde{\mu}] = 1 + \frac{A_s}{\Lambda^2} \left(\frac{2\pi}{h\omega_s\beta} \right) e^{-\beta\varepsilon} e^{\beta\tilde{\mu}}$$

$$A_{2DO}[T] = \frac{(2\pi)^{0.5} A_s}{\omega_s (\tilde{m})^{0.5} (k_B T)^{0.5}}$$

Other possibilities for mixed-potential adsorption sites are shown in Table S1 and indexed according to the type of potential in each of the spatial directions (x , y , and z). Upon derivation of the adsorption model, the form of $A[T]$ is unique to each choice of $q[\beta]$. The high-T heat capacity of the adsorbed phase in each model is equal to the order of T in the expression for $q[\beta]$ (e.g., $q_{2DO}[\beta] \propto \beta^{-2} \propto T^2$ so the heat capacity at high temperature is $2k_B T$).

Nomenclature:

Physical Constant	Variable	Value	Units
Boltzmann	k_B	1.381×10^{-23}	J K ⁻¹
Planck	h	6.626×10^{-34}	J s
Quantity	Variable	Typical Order	Units
Number of Adsorption Sites	N_s	10^{23}	molecules
Binding Energy	ε	10^1	kJ mol ⁻¹
Adsorbate Mass	\tilde{m}	10^{-27}	kg
Adsorption Site Length	L_s	10^{-1}	nm
Adsorption Site Area	A_s	10^{-2}	nm ²
Adsorption Site Volume	V_s	10^{-3}	nm ³
Natural Frequency	ω_s	10^{13}	s ⁻¹

Thermal de Broglie Wavelength:

$$\Lambda = \frac{h}{\sqrt{2\pi\tilde{m}k_B T}} = \frac{h\sqrt{\beta}}{\sqrt{2\pi\tilde{m}}}$$

Table S1. Partition functions and T-dependence of the adsorption equation for single-site Langmuir models of ideal gases, depending on the number and potential form of the external degrees of freedom in the adsorbed state. Abbreviations: DF = delta function, SP = square potential, QP = quadratic potential. Variables in **red** are fitting constants of the resulting model.

Model Name	Single Adsorption Site			Total Adsorption System		
	Partition Function (x × y × z)	Degrees of Freedom	High T Heat Capacity (k _B T)	Explicit A[T]	T Dep of A	Δ Heat Capacity (RT)
Einstein Crystal	QP × QP × QP	3	1 + 1 + 1 = 3	$\frac{(2\pi)^{1.5} (k_B T)^{0.5}}{\omega_s^3 (\tilde{m})^{1.5}}$	0.5	+1.5
(no physical picture)	QP × QP × SP	3	1 + 1 + 0.5 = 2.5	$\frac{2\pi L_s}{\omega_s^2 (\tilde{m})}$	0	+1
2D Lattice Gas	QP × QP × DF	2	1 + 1 + 0 = 2	$\frac{(2\pi)^{0.5} h}{\omega_s^2 (\tilde{m})^{1.5} (k_B T)^{0.5}}$	-0.5	+0.5
2D Ideal Gas w z-Oscillation	SP × SP × QP	3	0.5 + 0.5 + 1 = 2	$\frac{(2\pi)^{0.5} A_s}{\omega_s (\tilde{m})^{0.5} (k_B T)^{0.5}}$	-0.5	+0.5
(no physical picture)	QP × SP × DF	2	1 + 0.5 + 0 = 1.5	$\frac{h L_s}{\omega_s (\tilde{m}) (k_B T)}$	-1	0
3D Ideal Gas	SP × SP × SP	3	0.5 + 0.5 + 0.5 = 1.5	$\frac{V_s}{k_B T}$	-1	0
z-Oscillators	DF × DF × QP	1	0 + 0 + 1 = 1	$\frac{h^2}{\omega_s (2\pi\tilde{m}^3)^{0.5} (k_B T)^{1.5}}$	-1.5	-0.5
2D Ideal Gas	SP × SP × DF	2	0.5 + 0.5 + 0 = 1	$\frac{h A_s}{(2\pi\tilde{m})^{0.5} (k_B T)^{1.5}}$	-1.5	-0.5
1D Ideal Gas	SP × DF × DF	1	0.5 + 0 + 0 = 0.5	$\frac{h^2 L_s}{(2\pi\tilde{m}) (k_B T)^2}$	-2	-1
Fixed	DF × DF × DF	0	0 + 0 + 0 = 0	$\frac{h^3}{(2\pi\tilde{m})^{1.5} (k_B T)^{2.5}}$	-2.5	-1.5

References

- (1) Langmuir, I. The Constitution and Fundamental Properties of Solids and Liquids. Part I. Solids. *J. Am. Chem. Soc.* 1916, 38 (11), 2221–2295.
<https://doi.org/10.1021/ja02268a002>
- (2) Langmuir, I. The Constitution and Fundamental Properties of Solids and Liquids. II. Liquids. *J. Am. Chem. Soc.* 1917, 39 (9), 1848–1906. <https://doi.org/10.1021/ja02254a006>
- (3) Langmuir, I. The Adsorption of Gases on Plane Surfaces of Glass, Mica and Platinum. *J. Am. Chem. Soc.* 1918, 40 (9), 1361–1403. <https://doi.org/10.1021/ja02242a004>
- (4) Brunauer, S.; Emmett, P. H.; Teller, E. Adsorption of Gases in Multimolecular Layers. *J. Am. Chem. Soc.* 1938, 60 (2), 309–319. <https://doi.org/10.1021/ja01269a023>
- (5) Swenson, H.; Stadie, N. P. Langmuir’s Theory of Adsorption: A Centennial Review. *Langmuir* 2019, 35 (16), 5409–5426. <https://doi.org/10.1021/acs.langmuir.9b00154>
- (6) Hill, T. L. An Introduction to Statistical Thermodynamics; Addison-Wesley, 1960.
- (7) Stadie, N. P. Synthesis and Thermodynamic Studies of Physisorptive Energy Storage Materials, California Institute of Technology, 2012. <https://doi.org/10.7907/ZK3P-CV60>
- (8) Savara, A. Standard States for Adsorption on Solid Surfaces: 2D Gases, Surface Liquids, and Langmuir Adsorbates. *J. Phys. Chem. C* 2013, 117 (30), 15710–15715.
<https://doi.org/10.1021/jp404398z>
- (9) Wang, Z. Temperature Dependence of Gas Physisorption Energy: Experimental and Computational Studies of Krypton on Porous Carbon, PhD thesis, California Institute of Technology, 2023. <https://thesis.library.caltech.edu/15181/>
- (10) Quine, C. M. Tunability of Gas Adsorption Enthalpies in Carbonaceous Materials for Energy-Related Applications, California Institute of Technology, 2023.
<https://thesis.library.caltech.edu/15222/>
- (11) Gibbs, J. W. On the Equilibrium of Heterogeneous Substances. *Trans. Conn. Acad.* 1876, III, 108–248 and 343–524.
- (12) Callen, H. Thermodynamics and an Introduction to Thermostatistics, Second.; John Wiley & Sons, 1985.
- (13) Stylianou, K. C.; Warren, J. E.; Chong S. Y.; Rabone, J.; Bacsá, J.; Bradshaw, D.; Rosseinsky, M. J. CO₂ selectivity of a 1D microporous adenine-based metal-organic framework synthesized in water. *Chem. Commun.*, 2011, 47, 3389–3392.
<https://doi.org/10.1039/c0cc05559j>

- (14) Rouquerol, J.; Llewellyn, P.; Rouquerol, F. Is the BET Equation Applicable to Microporous Adsorbents? *Studies in Surface Science and Catalysis*; Elsevier, 2007; Vol. 160, pp 49–56. [https://doi.org/10.1016/S0167-2991\(07\)80008-5](https://doi.org/10.1016/S0167-2991(07)80008-5)
- (15) Banerjee, D., Simon, C., Plonka, A. *et al.* Metal-organic framework with optimally selective xenon adsorption and separation. *Nat. Commun.* **7**, ncomms11831 (2016). <https://doi.org/10.1038/ncomms11831>
- (16) Will, F. G. Hydrogen Adsorption on Platinum Single Crystal Electrodes. *J. Electrochem. Soc.* 1965, 112 (4), 451. <https://doi.org/10.1149/1.2423567>
- (17) Chiu, N. C.; Compton, D.; Gładysiak, A.; Simrod, S.; Khivantsev, K.; Woo, T. K.; Stadie, N. P.; Stylianou, K. C. Hydrogen Adsorption in Ultramicroporous Metal–Organic Frameworks Featuring Silent Open Metal Sites. *ACS Appl. Mater. Interfaces* 2023, acsami.3c12139. <https://doi.org/10.1021/acsami.3c12139>
- (18) Quine, C. M. REal Adsorption Langmuir Isotherms for Sorption Theory: REALIST. *Github*. <https://github.com/cullenmq/REALIST> (accessed 2025-03-30).
- (19) R. Rowsey, E. E. Taylor, R. W. Hinson, D. Compton, N. P. Stadie, R. K. Szilagyi, Does Boron or Nitrogen Substitution Affect Hydrogen Physisorption on Open Carbon Surfaces? *Phys. Chem. Chem. Phys.*, **24**, 28121–28126 (2022)
- (20) Mertens, F. O. Determination of Absolute Adsorption in Highly Ordered Porous Media. *Surf. Sci.* 2009, 603 (10–12), 1979–1984. <https://doi.org/10.1016/j.susc.2008.10.054>
- (21) Stadie, N. P.; Murialdo, M.; Ahn, C. C.; Fultz, B. Anomalous Isosteric Enthalpy of Adsorption of Methane on Zeolite-Templated Carbon. *J. Am. Chem. Soc.* 2013, 135 (3), 990–993. <https://doi.org/10.1021/ja311415m>
- (S1) Stylianou, K. C.; Warren, J. E.; Chong S. Y.; Rabone, J.; Bacsá, J.; Bradshaw, D.; Rosseinsky, M. J. “CO₂ Selectivity of a 1D Microporous Adenine-Based Metal–Organic Framework Synthesized in Water.” *Chem. Commun.*, 2011, 47, 3389–3392. <https://doi.org/10.1039/c0cc05559j>
- (S2) Wang, Z. “Temperature Dependence of Gas Physisorption Energy: Experimental and Computational Studies of Krypton on Porous Carbon.” PhD thesis, California Institute of Technology, 2023. <https://thesis.library.caltech.edu/15181/> (see section 2.4, “Surface Dynamics”)

CHAPTER FOUR

LIMITS OF LANGMUIR MODELING OF SUPERCRITICAL
ADSORPTION EQUILIBRIA: METHANE ON MOF-5 AS A
CASE STUDY

Contribution of Authors and Co-Authors

Manuscript in Chapter 4

Author: Dalton Compton

Contributions: Collected adsorption isotherms, analyzed data, produced figures, and wrote the manuscript.

Co-Author: Cullen M. Quine

Contributions: Collected adsorption isotherms, developed data analysis package, and assisted in editing the manuscript.

Co-Author: Peyton S. Summerhill

Contributions: Aided in data analysis and editing the manuscript

Co-Author: Channing C. Ahn

Contributions: aided in interpretation of results and editing the manuscript.

Co-Author: Brent T. Fultz

Contributions: aided in interpretation of results and editing the manuscript.

Co-Author: Nicholas P. Stadie

Contributions: Oversaw experimental design, aided in interpretation of results, and assisted in writing and editing the manuscript.

Manuscript Information

Dalton Compton[†], Cullen M. Quine[‡], Peyton S. Summerhill[†], Channing C. Ahn[‡], Brent T. Fultz[‡],
Nicholas P. Stadie[†]

[†]Department of Chemistry and Biochemistry, Montana State University, Bozeman, Montana,
59717, United States

[‡] California Institute of Technology, Pasadena California 91125, United States

Status of Manuscript:

- ☒ Prepared for submission to a peer-reviewed journal
- ☐ Officially submitted to a peer-reviewed journal
- ☐ Accepted by a peer-reviewed journal
- ☐ Published in a peer-reviewed journal

Abstract

Adsorption measurements are commonly interpolated and modeled using Langmuir-type equations in order to elucidate both structural properties of the adsorbent (e.g., number of adsorption sites, surface area, and pore volume) as well as thermodynamic properties of the adsorption system (e.g., the isosteric heat of adsorption). While accurate fits can be obtained with relatively simple models, questions remain as to whether the thermodynamic properties derived from such methods are meaningful, especially under supercritical conditions where the isotherms do not show well-resolved features. In this study, “blind” Langmuir modeling of both the structural and thermodynamic properties of CH₄ adsorption on MOF-5 (an established model system) was found to be significantly limited using only supercritical adsorption measurements; the ~75% of binding sites with 9-12 kJ mol⁻¹ binding energies were robustly detected, but the ~17% of strong binding sites could not be detected, even with significant constraining of the parameters. However, the isosteric heat of adsorption (q_{st}) at the average temperature of study is a robust deliverable of all Langmuir modeling efforts explored: 12.9 ± 0.6 kJ mol⁻¹ of CH₄ on MOF-5 at near-ambient conditions.

Introduction

Irving Langmuir’s adsorption models¹⁻³ (including the most well-known single-site or monolayer adsorption isotherm equation) are widely used to interpolate and interpret gas-solid adsorption equilibria measured in a wide range of systems and conditions. Despite that the models were originally designed to treat strong adsorbate-solid interactions (and negligible adsorbate-adsorbate interactions in both the bulk phase and the adsorbed phase), successful

applications of Langmuir theory have been demonstrated in systems with weak adsorbate-solid interactions as well.⁴ Brunauer, Emmett, and Teller improved Langmuir's multilayer model by applying a simple assumption in the second layer and above that is now the most widely used model for estimating the gas-accessible surface area of solid adsorbents: BET theory.⁵ The most successful applications of Langmuir's models for gas-solid systems are in dilute gas conditions where the bulk phase behaves as an ideal gas. For example, we recently investigated a pure single-site system (H_2 on a Ni-based porous crystal with single-molecule adsorption sites) in order to explore the role of the temperature dependence of the Langmuir constant prefactor; excellent agreement was achieved since H_2 was within 1% of ideal gas density under all conditions measured.⁶ The simplest single-site Langmuir model does not always fit to experimental adsorption equilibria owing to heterogeneity of the binding site environments (either inherent to the crystal structure or due to the presence of defects). In these cases, multi-site Langmuir models or even the uniform distribution Langmuir (or "Unilan"⁷) model can be employed with greater accuracy, especially when the bulk phase is still approximately an ideal gas under all conditions studied.

Nevertheless, great efforts have been made to modify Langmuir's models for applicability in regimes of interest for high-pressure catalysis, separations, and storage/delivery, far from the ideal limit.⁸ Some necessary strategies are to include the roles of the excluded volume of the bulk phase (i.e., the so-called "excess" adsorption amount must be modeled), the related and non-negligible molar volume of the adsorbed phase, the real-gas equation of state instead of the ideal gas law, and increasingly relevant adsorbate-adsorbate interactions in the adsorbed phase. Most of these strategies introduce some complexity (additional fitting

parameters) to the model, which increases the likelihood of overfitting the data. Our previous work has endeavored to prevent overfitting of the data while still accounting for the role of interactions in the bulk fluid (gas or supercritical fluid) in order to accurately assess the thermodynamics of adsorption.⁹⁻¹¹ All of this past work by our group has focused on carbon materials of varying surface homogeneity, inevitably tolerating significant heterogeneity owing to the complexity of porous carbon structure and composition. It therefore remains an open question as to just how much accuracy can be obtained from the thermodynamic modeling of such supercritical adsorption equilibria, especially under far-from-ideal gas conditions.

Alternatively, metal-organic frameworks (MOFs) are porous crystals, consisting of metal oxo or nitrido clusters connected by organic linkers, that form homogeneous structures with atomically precise adsorption sites.¹² Owing to their potential applications in catalysis, separation, and storage/delivery, this class of materials has garnered a lot of attention from adsorption researchers, both as fundamental and practical subjects of research across a wide variety of adsorbates. MOFs serve as ideal model materials for fundamental adsorption studies such as the investigation of the efficacy of Langmuir modeling for predicting relevant properties of adsorption systems from their measured adsorption equilibria. Despite this fact, few researchers report systematic studies of the modeling aspect of this work.

Hydrogen (H_2) and methane (CH_4) are common adsorbates for energy storage studies, an important potential application of MOFs.^{7,13} Both adsorbates are most often studied at supercritical temperatures, and often also up to supercritical pressures; unlike H_2 , significant improvements in total energy density of CH_4 can be readily achieved over pure compression at near-ambient temperatures.¹⁴⁻¹⁶ Understanding the relationship between the chemical

composition and structure of the binding site(s), the density of the overall crystal structure, and the packing density of the crystalline particles into a powder or monolith has been of highest importance in progressing toward ultimate energy storage density targets.^{11,14,15,17} The thermodynamic quantities of interest in adsorption-based storage systems are the binding site types and energies, as well as the isosteric heat of adsorption, where the latter is directly important for applications since adsorption is exothermic and the heat must be dissipated. Therefore, while H₂ and CH₄ studies on MOFs are widely reported, there is little understanding of how accurate Langmuir modeling is for MOFs despite its potential importance.

In this work, we use a series of Langmuir models to attempt to accurately determine the previously established^{18,19} binding site types and energies of methane on MOF-5 (the quintessential MOF²⁰) at supercritical temperatures. The guiding questions are whether Langmuir modeling of the experimental adsorption equilibria alone can successfully reproduce the number of different binding site types (previously directly identified by in situ neutron diffraction methods¹⁸) and also their energies (previously ranked using neutron diffraction¹⁸ and directly investigated via first-principles computational methods¹⁹). The results show that in complex adsorption systems investigated under high-pressure conditions, resolving the binding site landscape of the adsorbent is extremely challenging in the absence of a priori knowledge of the binding sites; however, the isosteric heat of adsorption emerges as a relatively model-independent property regardless of the binding sites and energies attributed.

Theory

The single-site Langmuir (SL) model¹⁻³ describes the simplest possible adsorption systems that abide by three assumptions: the bulk fluid is a pure ideal gas, the adsorbent is a rigid

solid with identical, independent adsorption sites, and each site can only accommodate a single adsorbate molecule. By any of several derivations,⁴ the SL model can be derived as a function of pressure as:

$$n_a[P] = n_{max} \frac{KP}{1 + KP} \quad \text{Eq. 1}$$

where n_a is the adsorbed amount (typically in dimensions of amount per mass of adsorbent), n_{max} is the total number of adsorption sites (in the same dimensions), P is the pressure of the bulk ideal gas, and K is the Langmuir “constant” (in dimensions of inverse pressure). The latter parameter (K) varies depending on the strength of the binding interaction.

Irving Langmuir also developed a more general multi-site model³ for solids that have a discrete set of distinct binding sites (each site type also only accommodating a single adsorbate molecule, but with a unique binding strength):

$$n_a[P] = n_{max} \sum_{i \text{ (sites)}} \alpha_i \frac{K_i P}{1 + K_i P} \quad \text{Eq. 2}$$

where i is an index over site types, α_i is the fraction of sites of type i , and K_i is the Langmuir “constant” of sites of type i . This model is subject to the constraint that $\sum_i \alpha_i = 1$. Hence, the number of fitting parameters increases significantly upon introducing additional binding site types, which can lead to over-fitting if applied to a set of experimental measurements without any underlying physical insight as to its necessity. It is important to assess whether the addition of site types in the fitting equation meets established criteria for statistical justification.

Langmuir-type models are widely used for the analysis of thermodynamic properties of adsorption systems such as the isosteric enthalpy (or “heat”) of adsorption (referred to herein as q_{st} or $-\Delta_{ads}H$). For materials with multiple binding site types with differing binding energies,

the isosteric heat of adsorption represents an average value at the conditions of T and P studied, and is offset from the energy by a factor of $\sim RT$ (where R is the gas constant) at low surface occupancies. In order to assess the individual site energies explicitly, a temperature-dependent model is needed; the “constant” K_i for a site of type i bears the relationship between T and the binding energy at that site, E_i , according to:

$$n_a[T, P] = n_{max} \sum_{i \text{ (sites)}} \alpha_i \frac{K_i[T]P}{1 + K_i[T]P} \quad \text{Eq. 3}$$

$$K_i[T] = A_i[T] e^{-\frac{E_i}{RT}} \quad \text{Eq. 4}$$

where $A_i[T]$ is a pre-exponential factor that represents the physical nature of the binding site.^{6,21} Analogous treatment of the BET model leads to a general multi-site BET equation of similar form (see Supporting Information). In past work,⁶ we showed that the goodness of fit to all such Langmuir-type models does not depend on the precise form of $A_i[T]$ and thus a temperature dependence of $A_i[T] \propto T^{-0.5}$ is used throughout the present work for all site types.

Additionally, it is important to distinguish between excess and absolute adsorption uptake in high-pressure supercritical conditions, where the difference between them is significant. J. Willard Gibbs first realized that it is not possible to directly measure the actual (absolute) adsorption uptake of any system and coined the term “excess” to describe the experimentally measured adsorption uptake quantity.²² The difference between excess and absolute uptake is:

$$n_e[T, P] = n_a[T, P] - \rho_g[T, P] \cdot V_a[T, P] \quad \text{Eq. 5}$$

where n_a is the actual or “absolute” adsorbed amount, n_e is the experimental or “excess” adsorbed amount, ρ_g is the density of the bulk (supercritical) fluid, and V_a is the volume of the adsorbed phase. All are functions of temperature and pressure; however, while ρ_g is a known

quantity (to high accuracy with a modern equation of state²³), V_a is a complex function that is difficult or impossible to measure.²⁴

Straightforwardly, in crystalline porous solids, the total pore volume, V_{pore} , can be used as an approximation of the maximum volume of the adsorbed phase, V_{max} . Multiplying V_{max} by the adsorption site occupancy fraction ($\theta = n_a/n_{tot}$) is a common method to approximate V_a :⁸

$$n_e[T, P] = (n_{max} - \rho_g[T, P] \cdot V_{max}) \sum_{i(sites)} \alpha_i \frac{K_i[T]P}{1 + K_i[T]P} \quad \text{Eq. 6}$$

In this work, the correction term is significant (see Supporting Information), and thus the excess adsorption equilibria need to be treated as such to achieve an accurate fit to any model. By combining Equation 6 with Equation 4, a series of multi-site Langmuir models can be “globally” fitted (i.e., incorporating an inherent temperature dependence, allowing all isotherms to be fitted with a single set of parameters) to supercritical adsorption equilibria of H₂ or CH₄ on porous crystalline materials such as MOFs.

Experimental Methods

Materials

MOF-5 was obtained from a commercial supplier (BASF AG) and, after activation at 403 K for 12 h under oil-free vacuum ($\leq 10^{-8}$ mbar, HiPace 80, Pfeiffer Vacuum GmbH), used as-received.

Materials Characterization

Powder X-ray diffraction (XRD) was measured under ambient conditions using a benchtop X-ray diffractometer (D2 Phaser, Bruker Corp.) with Cu K $\alpha_{1,2}$ radiation in reflection

geometry. The sample was mounted on an oriented silicon crystal to minimize background intensity.

Nitrogen (99.999%) adsorption/desorption analysis was measured using an automated Sieverts apparatus (3Flex, Micromeritics Corp.); the sample was held in a liquid nitrogen bath (the boiling temperature of N_2 is 75.9 K in Bozeman, Montana). The surface area was estimated using the Brunauer-Emmett-Teller (BET) model, employing the Rouquerol consistency criteria.²⁵ The pore size distribution was determined using a non-local density functional theory (NLDFT) slit pore model (implemented using Micromeritics MicroActive software).

Methane Adsorption Measurements

Methane (99.995%) adsorption/desorption uptake was measured using an automated Sieverts apparatus (3Flex, Micromeritics Corp.) as well as a high-pressure custom Sieverts apparatus (thoroughly described elsewhere²⁶). The sample was held in a temperature-controlled environment: either the cold well of a closed-cycle helium refrigerated cryostat (CH-104, ColdEdge Technologies, for temperatures <200 K) or within a custom Peltier device (for temperatures >200 K). Temperature precision of ± 0.1 K was achieved in both cases.

Methane Adsorption Modeling

All measured adsorption equilibria were assessed as to the significance of the conversion between excess and absolute uptake amounts prior to modeling (see Supporting Information). The supercritical adsorption isotherms were globally fitted to a series of Langmuir equations (SL, 2L, 3L, and 4L, where $i = 1, 1-2, 1-3, \text{ and } 1-4$, respectively), implementing the definition of “excess adsorption” described by Equation 6, using an open-source Python package

(REALIST,²⁷ v. 0.314). When converting the subcritical isotherms from excess to absolute, the correction term was deemed negligible (see Supporting Information).

Each series of isotherms was fitted “globally” (all at once) using a model with an explicit temperature dependence, referred to as “model -0.5” or “ $T^{-0.5}$ ” in past work.⁶ The goodness of fit was determined by taking the square root of the sum of squared residuals and dividing by the number of data points measured, referred to as RMSE. The errors of the fitting parameters were unable to be calculated for all the models and will not be shown until all have been calculated.

Structure Analysis

Structural modeling of the pore network of MOF-5 was performed using two dedicated software packages: CrystalMaker (v. 10.8.2) and Zeo++ (v. 0.3)²⁸. The probe radius used to determine the accessible volume in MOF-5 was 1.9 Å in both cases.

Results and Discussion

Crystalline Adsorbent MOF-5

MOF-5 was chosen as a model material for studies of the efficacy of Langmuir adsorption modeling of supercritical fluid adsorption at high pressures. Several properties of MOF-5 motivated this decision: it is porous (exhibiting a large amount adsorbed per quantity of adsorbent, improving the quality of the adsorption measurements), relatively rigid and stable (validating a key assumption of Langmuir’s models), and crystalline (exhibiting well-defined adsorption sites that are identical from place to place on the surface). While other candidate model materials also meet these requirements^{29,30}, MOF-5 further benefits from detailed previous studies of its binding sites toward CH₄, both experimentally¹⁸ and computationally¹⁹. A highly

crystalline and homogeneous powder of MOF-5 was obtained from a commercial supplier to ensure the measurement of high-quality adsorption equilibria (as verified by XRD and N₂ adsorption measurements, see Figure S1-S2).

The porous structure of MOF-5 consists of four ZnO₄ tetrahedra in a corner-sharing arrangement at each node, connected by benzene dicarboxylate linkers in a primitive cubic (pcu) net with a 12.9 Å edge length and ~12 Å pores (Figures 1a-1b). Out of square rotation of the rings in the dicarboxylate linkers leads to two distinct cages per unit cell: the first with the ring faces pointing in and the second with the ring edges pointing in (Figure 1b). Upon methane loading, previous neutron diffraction studies¹⁸ have shown that four binding sites are sequentially filled: cup (strong), hex (moderate), and cavity (weak) sites in the first cage type, where the latter is mainly interacting with other adsorbed methane, and a second type of moderate-strength sites near the nodes in the second cage type referred to as oxide sites (Figures 1b-1f). The binding energies of each site were subsequently estimated by computational methods¹⁹: -18.9 kJ mol⁻¹ (cup sites), -12.1 kJ mol⁻¹ (oxide sites), -9.0 kJ mol⁻¹ (hex sites), and -2.1 kJ mol⁻¹ (cavity sites). In addition, both studies agree as to the relative abundance of each site: cup (4 per node), oxide (12 per node), hex (6 per node), and cavity (~2 per node) comprising a total of ~24 CH₄ molecules per node (or per pcu cage). These previously established binding energies and relative quantities of each site provide a comprehensive picture of CH₄ adsorption in MOF-5 (Table 1) for comparison to Langmuir modeling results.

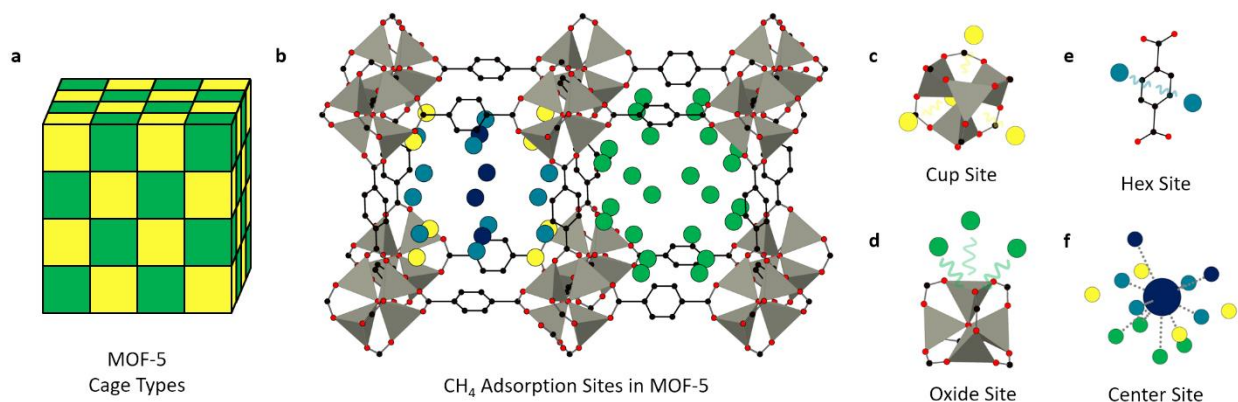


Figure 1. Crystal structure of MOF-5 showing (a) two cage types within its repeating 3D checkerboard structure and (b-f) four CH₄ binding sites identified by past neutron diffraction studies:¹⁸ cup sites are shown in yellow, oxide sites in green, hex sites in teal, and selected cavity sites in dark blue. Zinc is shown in gray, carbon in black, and oxygen in red (hydrogen is omitted for clarity).

Table 1. Summarized properties of CH₄ adsorption on MOF-5, per past reports^{18,19}.

Site Index (<i>i</i>)	Site Type	No. Per Node ¹⁸	No. Per Mass ¹⁸ (mmol g ⁻¹)	α_i	Binding Energy ¹⁹ (kJ mol ⁻¹)
1	cup	4	5.2	0.17	-18.9
2	oxide	12	15.6	0.50	-12.1
3	hex	6	7.8	0.25	-9.0
4	cavity	~2	2.6	0.083	-2.1
	Total:	24	31.2	1	

Methane Adsorption on MOF-5

An extensive set of methane adsorption equilibria (excess uptake, in mmol g⁻¹) as a function of pressure (in bar) and temperature (in K) were measured between 0-100 bar and 243-328 K (Figure 2). Owing to the similar molar density of the bulk and adsorbed phases in the near-critical regime ($P_c = 46.1$ bar, $T_c = 190.6$ K), the excess adsorption isotherms increase to a maximum and then decrease at high pressures (Figure 2a-2b). While not directly measured, the

underlying absolute adsorbed uptake is known to increase monotonically with pressure and is expected to be considerably higher than the measured excess uptake under dense supercritical fluids such as methane at 243 K and 100 bar. However, it cannot be ascertained by inspection alone. Furthermore, no particular features are observed in the supercritical isotherms that would indicate the presence of multiple site types.

For comparison to the featureless supercritical adsorption equilibria, a series of subcritical isotherms were also measured between 0-1 bar and 95-112 K (Figure 2c-2d). By contrast, the low-temperature, low-pressure subcritical isotherms exhibit a distinct pore-filling plateau since the bulk fluid is significantly lower density than the adsorbed phase in that regime; hence, in the subcritical regime, the excess uptake could simply be converted to absolute uptake by neglecting the contribution of the correction term, as detailed in the Supporting Information. This measured plateau at 95-112 K corresponds to a maximum of 36.1 mmol g⁻¹ or 27.8 methane molecules per cage, ~16% higher than the maximum detected by neutron diffraction studies.¹⁸ We attribute this increase in maximum uptake to extra-particle surface adsorption effects. In addition, an early rise in each isotherm is also detected, prior to the pore-filling condensation event. This early rise reaches a maximum of 6.5 mmol g⁻¹ or 8.4 methane molecules per cage, indicating that it could be a more selective measurement of the strongest binding sites.

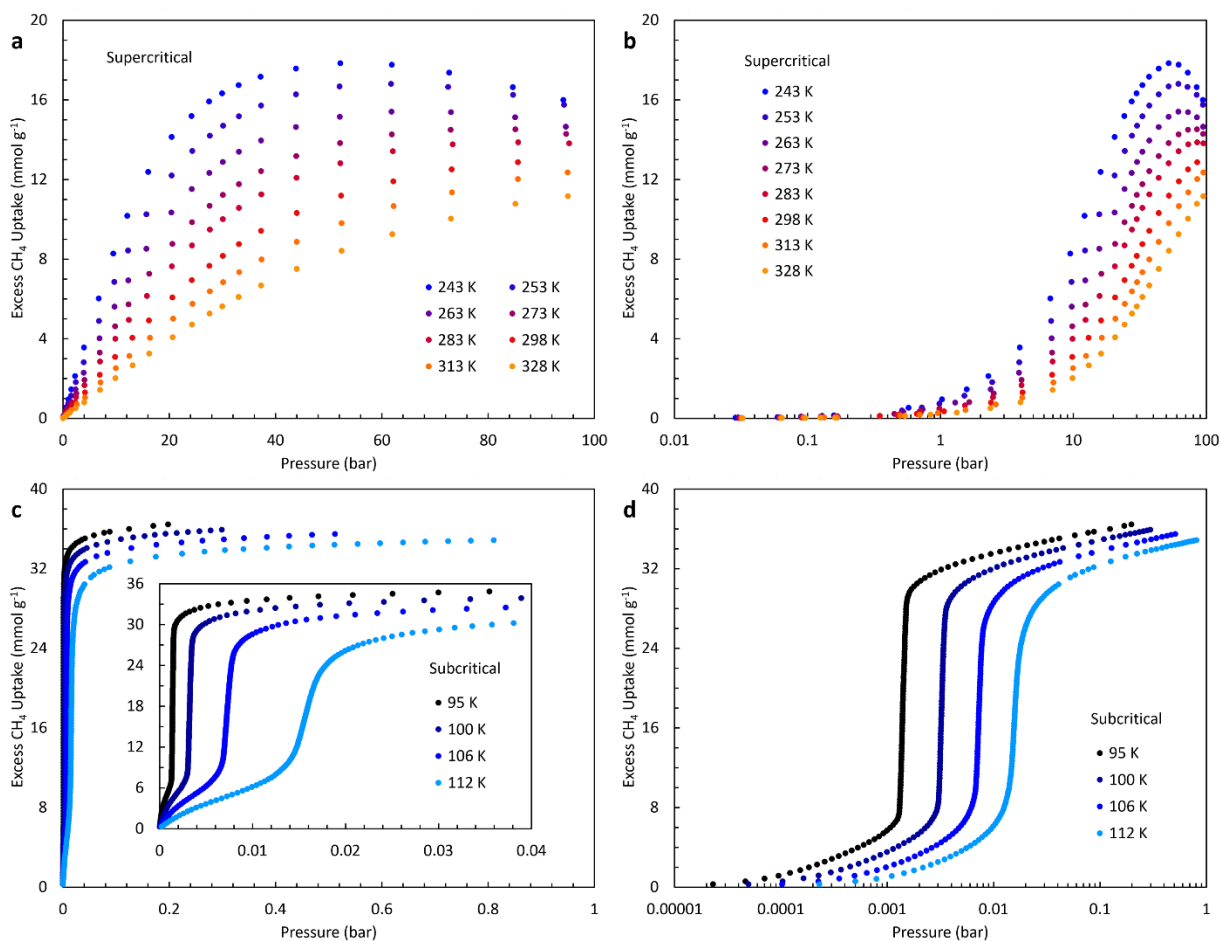


Figure 2. Equilibrium excess adsorption uptake of CH₄ on MOF-5 between (a-b) 243-328 K and 0-100 bar and (c-d) 95-112 K and 0-1 bar.

Supercritical Adsorption Equilibria Fitting

To test the capabilities of Langmuir modeling to both predict structural properties of MOF-5 as well as describe the binding energy distribution of complex materials, the supercritical CH₄ adsorption equilibria (Figures 2a-2b) were globally fitted to a series of Langmuir-type models of increasing complexity from single-site (SL) to four-site (4L) descriptions based on Equation 6. In the first set of fitting experiments, all of the parameters were allowed to be loose; these fits are referred to as “blind” fits (Figure 3). The best fit parameters upon “blind” fitting for

all models ($\text{RMSE} < 0.033 \text{ mmol g}^{-1}$ per point for SL to 4L). Surprisingly, increasing the number of fitting parameters beyond the SL model did not improve the quality of the fits. The total number of CH_4 adsorption sites on MOF-5 was determined to be $\sim 36 \text{ mmol g}^{-1}$, which is higher than the past neutron diffraction result but approximately equal to the value ascertained from the subcritical adsorption plateau. However, the V_{max} was determined by “blind” fitting to be 2.3-2.4 mL g^{-1} , which is far greater than the pore volume of MOF-5 (determined to be 1.30 mL g^{-1} using Zeo++ and 1.47 mL g^{-1} based on the total pore volume via N_2 adsorption analysis on the same experimental sample). All of the “blind” fits identified a majority of binding sites with an adsorption energy of $\sim 11 \text{ kJ mol}^{-1}$ (with a characteristic pre-exponential factor of $\sim 0.002 \text{ K}^{1/2} \text{ bar}^{-1}$); multi-site modeling (2L to 4L) did not clearly reveal the presence of stronger binding sites ($> 13 \text{ kJ mol}^{-1}$). Further analysis of the site energies and relative composition of each was therefore not performed owing to the unphysical magnitude of V_{max} .

In a series of additional fitting experiments, n_{max} and V_{max} were variously fixed at known values based on a variety of sources: past neutron diffraction experiments,¹⁸ subcritical CH_4 adsorption measurements (via the plateau value), computational pore volume (via Zeo++ using a CH_4 probe), and experimental total pore volume (via N_2 adsorption analysis at 77 K). These fits are referred to as the “blind* com.”, “blind* exp.”, “loose com.”, and “loose exp.” fits, where “blind*” and “loose” refers the variables being held constant while exp. and com. refers to the experimental and computation finding for n_{max} , V_{max} , binding site energies, pre-exponential factors, and relative quantities (see Figures S3, S4, S6, S7). The best fit parameters upon “blind*” and “loose” fitting are shown in Tables S1, S2, S4, S5. In all cases, the resulting fits were statistically poorer ($\text{RMSE} > 0.04 \text{ mmol g}^{-1}$ per point) than those in the “blind” series,

as expected. However, unlike the “blind” fits, the “loose” fits of the SL model were significantly poorer than the 2L-4L models when fixing both n_{max} and V_{max} to known values. A representative “loose” fit to the 3L model is shown in Figure 3e. The binding energies estimated by all of the “loose” fits vary from -14 kJ mol^{-1} to -1 kJ mol^{-1} (perhaps revealing the presence of a content of weaker binding sites), but the respective fractions of each site type show a majority of the sites centered at a binding energy of $\sim 12 \text{ kJ mol}^{-1}$. This is consistent with past computational studies¹⁹ which show $\sim 75\%$ of the sites to be between -9 and -12 kJ mol^{-1} . In all “loose” fits, no sites with a higher binding energy of -18 kJ mol^{-1} were observed, clearly showing that a good fit to the data could be achieved without the presence of a strong binding site in the model.

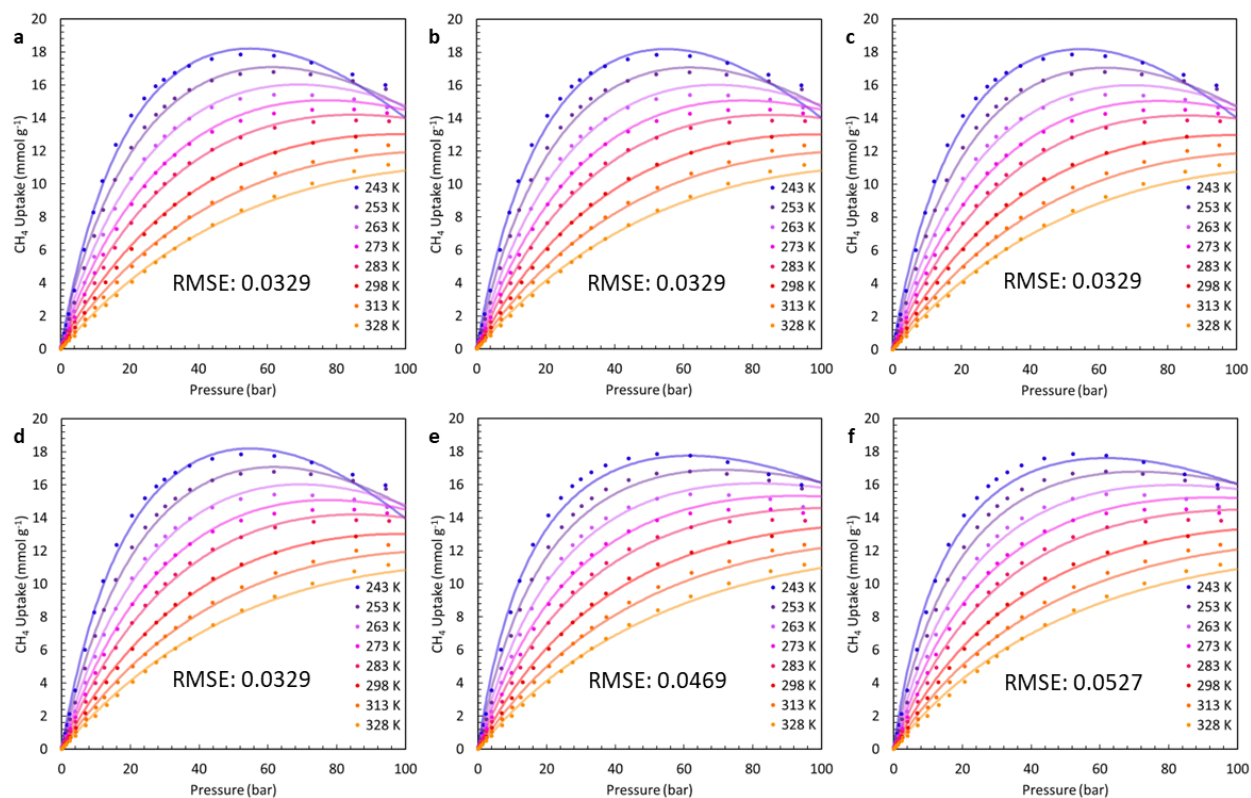


Figure 3. Equilibrium excess uptake (circles) of CH₄ on MOF-5 between 243–328 K and 0–100 bar fitted to a series of “blind” Langmuir models (lines) with varying complexity: (a) 1L, (b) 2L, (c) 3L, and (d) 4L. For comparison, representative fits to (e) a more constrained “loose” 3L model and (f) a “fixed” 4L model are shown. Goodness of fit (RMSE) is indicated.

Given the struggles to distinctly identify the presence of a higher energy binding site using a “blind”, “blind*”, or “loose” fitting approach, a fourth set of fitting experiments was undertaken with either the binding energies (E_i) or the binding site compositions (α_i) fixed to their known values as determined by past computational studies¹⁹. Hence, both fitting methods employed constrained versions of the 4L model. The only fitting parameters left loose in these approaches were the pre-exponential factors (A_i) for each site type. These methods are referred to as “tight” fits (Figures S5, S8); the best fit parameters upon “tight” fitting are shown in Tables S3, S6. Interestingly, these methods both provided a reasonable fit to the experimental data.

Nevertheless, even when the binding site compositions were fixed, a strong binding site type was not clearly revealed. Only when the binding site energies were fixed to the known values (from past computational studies) did the resulting composition parameters (α_i) agree with the past neutron diffraction results. The goodness of fit was generally similar to that of the “loose” methods, implying an intrinsic relationship between A_i and E_i that permits a wide range of E_i for each site type without incurring a significant error.

Finally, a “fixed” fitting approach was undertaken to determine if a reasonable fit of the measured supercritical adsorption equilibria could be obtained using all of the previously determined properties of CH₄ on MOF-5: the number of binding site types, their binding energies and their relative quantities (based on neutron diffraction and computational chemistry experiments). Hence, in the “fixed” method, only the pre-exponential factors (A_i) were permitted to be loose; the results are also shown in Figure 3f, Figure S8, Table 3, and Table S6. The strong binding site (fixed at $-18.9 \text{ kJ mol}^{-1}$) was accompanied by a much lower pre-exponential factor ($0.000689 \text{ K}^{1/2} \text{ bar}^{-1}$) than found in any previous fitting experiment. In short, an adequate fit to the supercritical adsorption equilibria could be achieved using a model that accounted for all of the past reported properties of the system. Nevertheless, the high-energy binding of CH₄ on MOF-5 at the cup sites (detected by both neutron diffraction and computational modeling) could not meaningfully be detected by any Langmuir modeling approach, except when the presence of that site type was known a priori.

Fitting Parameter Correlation

Owing to the similar quality of fits achieved both when all of the binding energies were clustered around $11\text{-}12 \text{ kJ mol}^{-1}$ and when the distribution of binding energies was forcibly

broadened to include ~17% of strong sites and ~8% of very weak sites, the relationship between the binding energies and the pre-exponential factors across all fits was further explored. A compensating correlation was found to exist between A_i and E_i (Figure S10), with a logarithmic relationship: $E_i(\text{kJ mol}^{-1}) = -2.18 \ln A_i(\text{K}^{1/2} \text{ bar}^{-1}) - 1.77$ (Equation S1). The origin of this relationship remains unknown, and will be the focus of future research. No systematic relationship between the best-fit value of E_i and the goodness of fit was observed, but “blind” fitting using a wide variety of least-squares minimization methods always produced SL binding energies of ~11 kJ mol⁻¹ for CH₄ on MOF-5, indicating a minimum in the overall error when the binding energies are centered around that value.

Subcritical Adsorption Equilibria Fitting

To further investigate the relative quantity and binding energy of the strongest binding sites in MOF-5, a complementary investigation was undertaken at subcritical temperatures (Figures 2c-2d) where the majority of CH₄ binding interactions would likely be of the strongest type. The subcritical adsorption equilibria were fitted to an SL model, which resulted in an acceptable set of best-fit parameters, as confirmed by statistical analysis (RMSE = 0.0187 mmol g⁻¹) and visual inspection (Figure S11). The best-fit parameters upon subcritical fitting are shown in Table S5. Contrary to our hypothesis, the resulting binding energies revealed by this method were still ≤ 13 kJ mol⁻¹ and the strong cup sites identified in past work (with a binding energy of 18.9 kJ mol⁻¹) remained elusive. A comparison between the extrapolated “blind” fit of the supercritical adsorption equilibria and the measured low-pressure subcritical adsorption equilibria reveals that there is excellent consistency between the two sets of measurements,

neither requiring the presence of strong binding sites to describe macroscopic CH₄ adsorption measurements on MOF-5 (Figure S12).

Table 2. Best-fit global Langmuir model parameters for single- (SL) to four- (4L) site Langmuir models of CH₄ adsorption on MOF-5 under “blind” fitting conditions (where no parameters were fixed).

Fitting Parameter	Single-Site	Double-Site	Three-Site	Four-Site
n_{\max} (mmol g ⁻¹)	36.3	36.3	36.2	37.1
V_{\max} (mL g ⁻¹)	2.36	2.36	2.34	2.43
α_1	1	0.935	0.418	0.522
A_1 (K ^{1/2} bar ⁻¹)	0.00206	0.00204	0.00139	0.00112
E_1 (kJ mol ⁻¹)	-11.2	-11.2	-12.0	-12.4
α_2	-	0.065	0.447	0.442
A_2 (K ^{1/2} bar ⁻¹)	-	0.00281	0.00236	0.00325
E_2 (kJ mol ⁻¹)	-	-10.5	-10.8	-10.2
α_3	-	-	0.135	0.026
A_3 (K ^{1/2} bar ⁻¹)	-	-	0.00452	0.0798
E_3 (kJ mol ⁻¹)	-	-	-9.50	-0.423
α_4	-	-	-	0.010
A_4 (K ^{1/2} bar ⁻¹)	-	-	-	0.0527
E_4 (kJ mol ⁻¹)	-	-	-	-0.418
RMSE (mmol g ⁻¹)	0.0329	0.0329	0.0329	0.0329

Table 3. Best-fit global Langmuir model parameters for a “fixed” four-site Langmuir (4L) model of CH₄ adsorption on MOF-5 (where n_{tot} , V_{max} , α_i , and E_i were fixed).

Fitting Parameter	Four-Site “Tight α_i ”	Four-Site “Tight E_i ”	Four-Site “Fixed”
n_{max} (mmol g ⁻¹)	36.1	36.1	36.1
V_{max} (mL g ⁻¹)	1.47	1.47	1.47
α_1	0.5	0.111	0.167
A_1 (K ^{1/2} bar ⁻¹)	0.000964	7.43E-5	5.12E-6
E_1 (kJ mol ⁻¹)	-13.7	-18.9	-18.9
α_2	0.167	0.499	0.5
A_2 (K ^{1/2} bar ⁻¹)	0.00418	0.00195	0.00200
E_2 (kJ mol ⁻¹)	-10.6	-12.1	-12.1
α_3	0.083	0.168	0.25
A_3 (K ^{1/2} bar ⁻¹)	0.00461	0.008125	0.00723
E_3 (kJ mol ⁻¹)	-10.5	-9.0	-9.0
α_4	0.25	0.222	0.083
A_4 (K ^{1/2} bar ⁻¹)	0.00481	8.17E-6	2.22E-7
E_4 (kJ mol ⁻¹)	-0.503	-2.1	-2.1
RMSE (mmol g ⁻¹)	0.0482	0.0470	0.0527

Isosteric Heat of Adsorption

The isosteric heat of adsorption (q_{st} or $-\Delta_{ads}H$) is a key practical metric for adsorption systems and its measurement and interpretation is extensively documented.³¹ Generally, q_{st} describes the quantity of heat released per mass or mole of adsorbate upon adsorption (i.e., the transition from the bulk gas or supercritical fluid to the adsorbed phase) and typically depends on the surface occupancy of the adsorbent. The dependency on surface occupancy occurs for at least two possible reasons: a varying binding energy on a heterogeneous surface (since energy and enthalpy are offset by the quantity $\Delta_{ads}PV \approx RT$ at low loadings) and the varying quantity of

$\Delta_{ads}PV$ (which approaches zero at high loadings under high-pressure, supercritical conditions).

The temperature dependence of q_{st} is more subtle and the topic of ongoing research.^{32,33}

Regardless of its dependence on temperature and pressure, the interpretation of q_{st} as a measure of binding strength is both universal and practically relevant. The Clapeyron equation provides the general definition:

$$q_{st}[T, P] = -\Delta_{ads}H[T, P] = T \Delta_{ads}S = T \left(\frac{\partial P}{\partial T} \right)_{n_a} \Delta_{ads}v = T \left(\frac{\partial P}{\partial T} \right)_{n_a} (v_a - v_g) \quad \text{Eq. 7}$$

where the partial derivative is given by the equation for the chosen model and v_a and v_g are the molar volumes of the adsorbed phase and the bulk fluid, respectively. While the latter volume is given by the equation of state²³, the volume of the adsorbed phase (v_a) is not possible to measure. For consistency with Equation 6, the following definition of v_a has been adopted herein:

$$v_a[T, P] = V_{max} \frac{n_a[T, P]}{n_{max}} \quad \text{Eq. 8}$$

The isosteric heat of CH₄ adsorption on MOF-5, according to “blind” fits to four different Langmuir models at supercritical conditions, is shown in Figure 4. The binding energy distribution for each model is also shown. It is clear that the choice of model does not play a significant role in the resulting heat of adsorption; regardless of the complexity of the model, q_{st} varied between 12-13 kJ mol⁻¹ under all conditions studied. Hence, q_{st} is a relatively model-independent quantity compared to the binding site energy distribution (given by the number and magnitude of E_i values in the complete set).

The consistency of q_{st} from model to model is even more clearly seen when comparing the results over all five fitting experiments carried out in this study. The isosteric heat of CH₄

adsorption on MOF-5 according to 15 different models is shown at the average temperature of study (279 K) in Figure 5. All of the results exhibit a monotonic decrease in isosteric heat of adsorption as a function of CH₄ uptake (or surface occupancy), as expected. Importantly, none of the models (even those like the “fixed” 4L model that contains ~17% of sites with a strong binding energy of $-18.9 \text{ kJ mol}^{-1}$) show a large isosteric heat of adsorption at low coverage. This is emblematic of the general result that q_{st} is a relatively model-independent outcome of adsorption modeling, even across models with a widely varying description of the binding energy landscape on the surface. The average value (and standard error) of q_{st} at 279 K and low loadings across all models in this study is $12.9 \pm 0.6 \text{ kJ mol}^{-1}$.

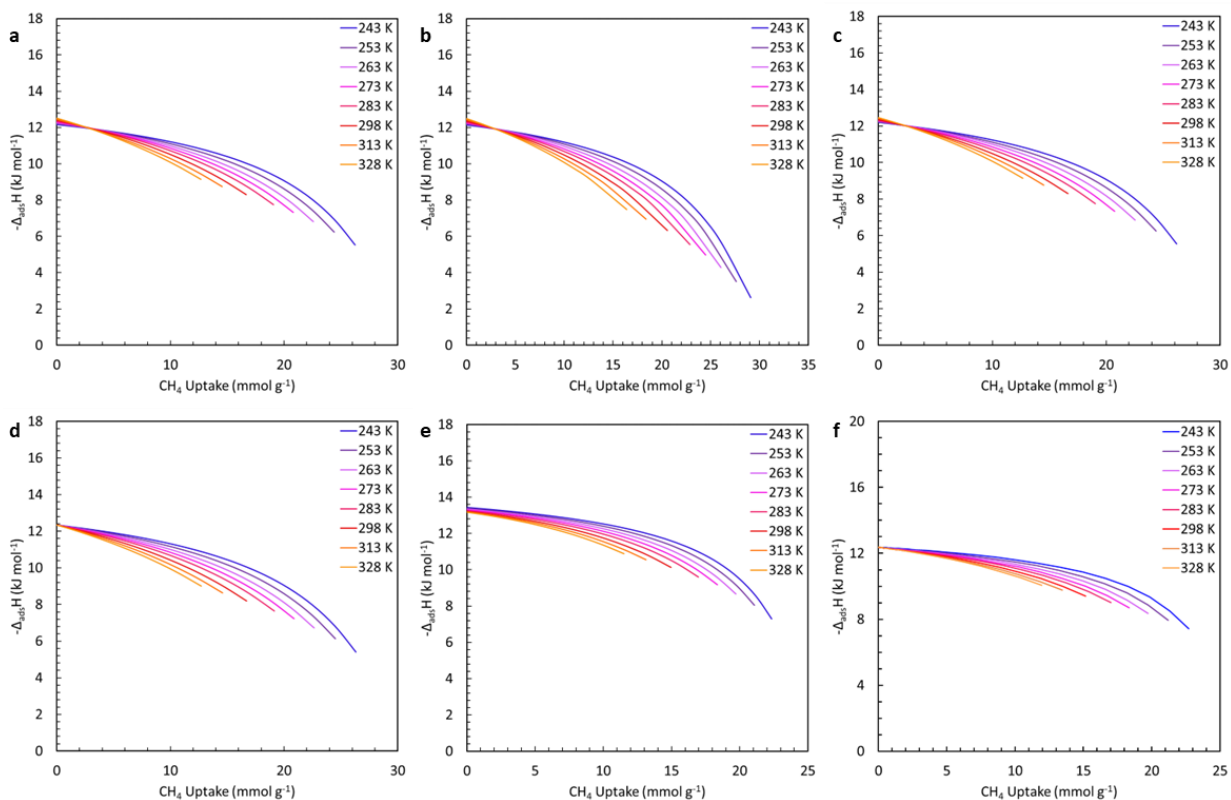


Figure 4. Isosteric heat of adsorption of CH₄ on MOF-5 between 243-328 K and 0-100 bar based on a series of “blind” Langmuir models with varying complexity: (a) SL, (b) 2L, (c) 3L, and (d) 4L. For comparison, the same results based on (e) a more constrained “loose” 3L model and (f) a “fixed” 4L model are shown. Temperature is indicated by color from 243 K (blue) to 328 K (yellow).

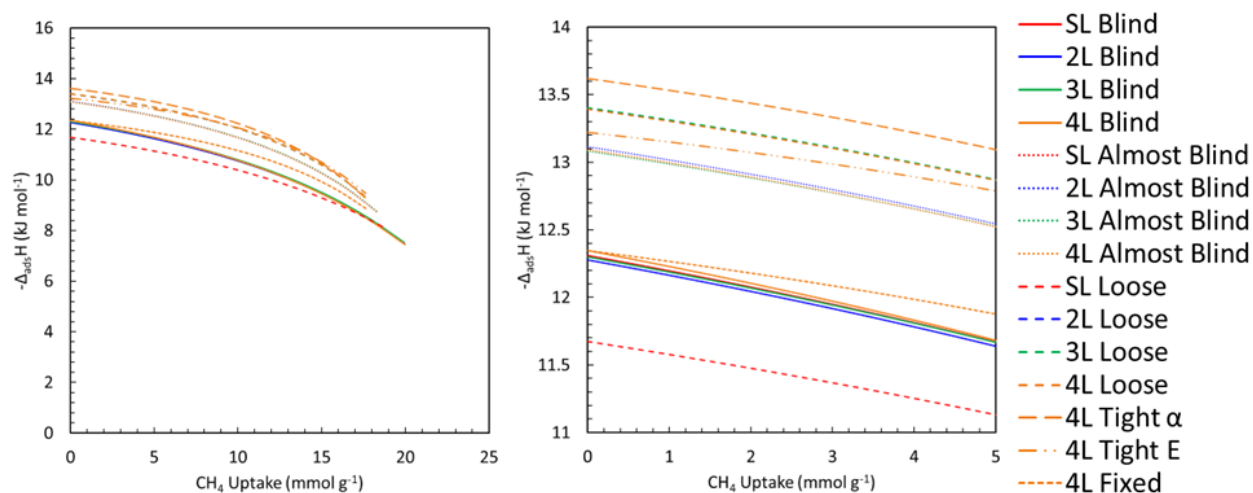


Figure 5. Isosteric heat of adsorption of CH_4 on MOF-5 at 279 K and 0-100 bar based on all fitting experiments in this study. Model type and fitting method are indicated by color.

Conclusion

Methane adsorption was measured on a high-quality, crystalline sample of a metal-organic framework (MOF-5) across sub- and supercritical bulk fluid conditions, between 95-112 K and 243-328 K at 0-1 bar and 0-100 bar, respectively. The adsorption equilibria were then globally fitted to a series of Langmuir equations, starting with simple single-site models (SL) and increasing to multi-site models (up to 4L), with standard methods to treat aspects such as the temperature dependence of the Langmuir constant, the volume growth of the adsorbed phase, and real-gas effects on the isosteric heat of adsorption. This experimental design allowed for the direct comparison of best-fit properties such as the total number of binding sites (n_{max}), maximum volume of the adsorbed phase (V_{max}), and site type and binding energy distribution (α_i and E_i) between models across the temperature and pressure range of highest interest for energy storage applications.

In this study, we determined that Langmuir modeling alone falls short at accurately determining the binding site energies of a multi-site material when the measurements are made at supercritical temperatures and up to high pressures. This remained true even when stricter and stricter constraints were enforced which should have guided the best-fit parameters toward previously established values (by other methods such as neutron scattering and computational chemistry). Regardless of the model chosen, none revealed a stronger binding site than 14 kJ mol⁻¹ unless specifically constrained to do so. Instead, all of the models show a majority of the binding sites to exhibit energies of ~12 kJ mol⁻¹, with a possible detectable contribution from weaker sites (~1 kJ mol⁻¹). Measuring and modeling the adsorption equilibria under subcritical conditions also did not elucidate any high-energy binding sites. The models show there is a distribution of sites where there is a singular high energy site, two medium energy sites, and a single low binding energy site. This brings into some question on the “truth” of the computational results and how accurate these values are in experimental systems. This suggests that researchers attempting to determine the binding site energy landscape of a novel material or adsorption system should proceed with caution when using a Langmuir-type modeling approach. However, the isosteric heat of adsorption remains robust and consistent across all models studied, affirming its relatively model-independent nature.

Associated Content

Acknowledgements

We gratefully acknowledge Justin Purewal for providing the sample of MOF-5. This work was supported by the U.S. Department of Energy’s Office of Energy Efficiency and

Renewable Energy (EERE) under the Hydrogen and Fuel Cell Technologies and Vehicle Technologies Offices under Award Number DE-EE0008815.

Supporting Information

Absolute vs. Excess Adsorption: The maximum correction term in Equation 5 in the main text ($\rho_g V_a$) was determined to be significant and must be accounted for upon fitting.

For the MOF used in this study, MOF-5, the total pore volume accessible to CH₄ was calculated using a standard software package (Zeo++) using the experimentally determined crystal structure a probe radius of 1.9 Å (corresponding to CH₄), as well as N₂ adsorption. The pore volume was found to be 1.30 and 1.47 mL g⁻¹. The densest gas phase of methane encountered under the supercritical experimental conditions explored in this work (calculated using NIST Refprop) was 7.034 mmol mL⁻¹ at 243 K and 94.17 bar.

By combining these two quantities, the maximum possible correction term is 10.32 mmol g⁻¹ which is ~58% of the measured maximum (excess) uptake quantity at 243 K and 52 bar. This correction term must be accounted for in all supercritical experimental conditions explored. In the subcritical experimental conditions, the densest gas phase encountered was 0.0898 mmol mL⁻¹ at 0.811 bar and 112 K. The largest possible correction term for the subcritical conditions is 0.132 mmol g⁻¹ which is ~0.36% of the total uptake. This is below the standard error associated with the measurement and is therefore negligible.

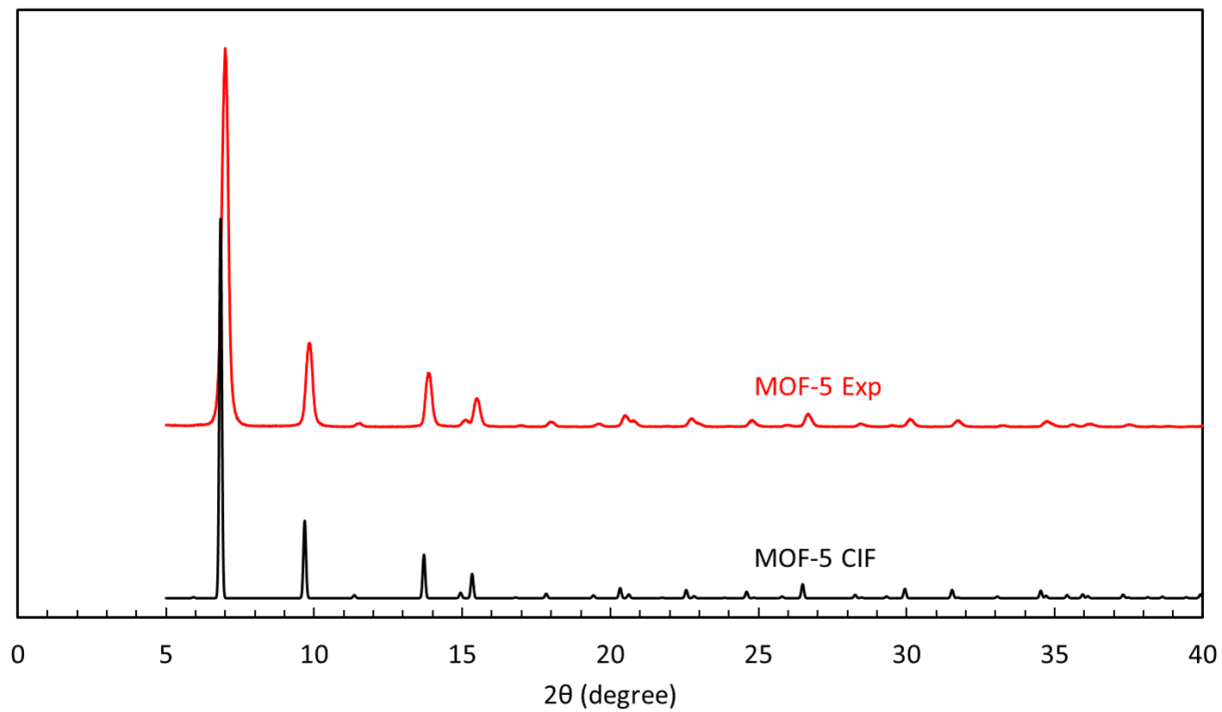
Powder X-Ray Diffraction Analysis:

Figure S1. XRD pattern of MOF-5 powder studied in this work compared to a simulated pattern.

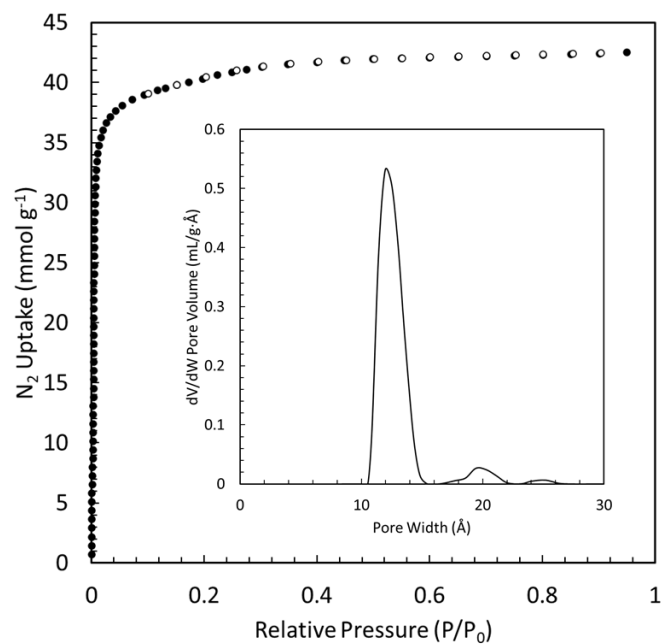
Nitrogen Adsorption Analysis:

Figure S2. Equilibrium N_2 adsorption/desorption isotherms at ~ 77 K and the corresponding NLDFT pore size distribution.

Best-Fit Parameters for Supercritical SL-4L Models:

Table S1. Best-fit global Langmuir model parameters for single- (SL) to four- (4L) site Langmuir models of CH₄ adsorption on MOF-5 under “blind* exp.” fitting conditions (where only $V_{max} = 1.47 \text{ mL g}^{-1}$ was fixed).

Fitting Parameter	Single-Site	Double-Site	Three-Site	Four-Site
$n_{\max} (\text{mmol g}^{-1})$	30.0	30.0	30.0	30.0
$V_{\max} (\text{mL g}^{-1})$	1.47	1.47	1.47	1.47
α_1	1	0.9998	0.424	0.997
$A_1 (\text{K}^{1/2} \text{ bar}^{-1})$	0.00189	0.00187	0.00110	0.00187
$E_1 (\text{kJ mol}^{-1})$	-11.9	-12.0	-13.1	-12.0
α_2	-	0.0002	0.564	0.001
$A_2 (\text{K}^{1/2} \text{ bar}^{-1})$	-	.152	0.00271	0.0117
$E_2 (\text{kJ mol}^{-1})$	-	-1.86	-11.2	-8.05
α_3	-	-	0.012	0.001
$A_3 (\text{K}^{1/2} \text{ bar}^{-1})$	-	-	0.00607	0.0348
$E_3 (\text{kJ mol}^{-1})$	-	-	-9.48	-5.39
α_4	-	-	-	0.001
$A_4 (\text{K}^{1/2} \text{ bar}^{-1})$	-	-	-	0.0694
$E_4 (\text{kJ mol}^{-1})$	-	-	-	-3.87
RMSE (mmol g^{-1})	0.0401	0.0401	0.0401	0.0401

Table S2. Best-fit global Langmuir model parameters for single- (SL) to four- (4L) site Langmuir models of CH₄ adsorption on MOF-5 under “loose exp.” fitting conditions (where only $n_{max} = 36.1$ mmol g⁻¹ and $V_{max} = 1.47$ mL g⁻¹ were fixed).

Fitting Parameter	Single-Site	Double-Site	Three-Site	Four-Site
n_{max} (mmol g ⁻¹)	36.1	36.1	36.11	36.1
V_{max} (mL g ⁻¹)	1.47	1.47	1.467	1.47
α_1	1	0.775	0.042	0.712
A_1 (K ^{1/2} bar ⁻¹)	0.00242	0.00181	0.000946	0.00160
E_1 (kJ mol ⁻¹)	-10.5	-12.2	-13.6	-12.5
α_2	-	0.225	0.735	0.063
A_2 (K ^{1/2} bar ⁻¹)	-	1.51E-5	0.00186	0.00581
E_2 (kJ mol ⁻¹)	-	-0.533	-12.2	-9.72
α_3	-	-	0.223	0.002
A_3 (K ^{1/2} bar ⁻¹)	-	-	2.19E-5	0.0378
E_3 (kJ mol ⁻¹)	-	-	-0.0526	-5.33
α_4	-	-	-	0.223
A_4 (K ^{1/2} bar ⁻¹)	-	-	-	2.09E-10
E_4 (kJ mol ⁻¹)	-	-	-	-0.000839
RMSE (mmol g ⁻¹)	0.0955	0.0469	0.0469	0.0469

Table S3. Best-fit global Langmuir model parameters four-site Langmuir (4L) models of CH₄ adsorption on MOF-5 under “tight α exp.” (where n_{max} , V_{max} , and α_i were fixed), “tight E exp.” (where n_{max} , V_{max} , and E_i were fixed), and “fixed exp.” (where n_{max} , V_{max} , α_i , and E_i were fixed) fitting conditions.

Fitting Parameter	Four-Site “Tight α_i ”	Four-Site “Tight E_i ”	Four-Site “Fixed”
n_{max} (mmol g ⁻¹)	36.1	36.1	36.1
V_{max} (mL g ⁻¹)	1.47	1.47	1.47
α_1	0.5	0.111	0.167
A_1 (K ^{1/2} bar ⁻¹)	0.000964	7.43E-5	8.69E-5
E_1 (kJ mol ⁻¹)	-13.7	-18.9	-18.9
α_2	0.167	0.499	0.5
A_2 (K ^{1/2} bar ⁻¹)	0.00418	0.00195	0.00208
E_2 (kJ mol ⁻¹)	-10.6	-12.1	-12.1
α_3	0.083	0.168	0.25
A_3 (K ^{1/2} bar ⁻¹)	0.00461	0.008125	0.000124
E_3 (kJ mol ⁻¹)	-10.5	-9.0	-9.0
α_4	0.25	0.222	0.083
A_4 (K ^{1/2} bar ⁻¹)	0.00481	8.17E-6	.171
E_4 (kJ mol ⁻¹)	-0.503	-2.1	-2.1
RMSE (mmol g ⁻¹)	0.0482	0.0470	0.0493

Table S4. Best-fit global Langmuir model parameters for single- (SL) to four- (4L) site Langmuir models of CH₄ adsorption on MOF-5 under “blind* com.” fitting conditions (where only $V_{max} = 1.30 \text{ mL g}^{-1}$ was fixed).

Fitting Parameter	Single-Site	Double-Site	Three-Site	Four-Site
$n_{max} \text{ (mmol g}^{-1}\text{)}$	28.9	28.9	28.9	28.9
$V_{max} \text{ (mL g}^{-1}\text{)}$	1.30	1.30	1.30	1.30
α_1	1	0.917	0.9992	0.9750
$A_1 \text{ (K}^{1/2} \text{ bar}^{-1}\text{)}$	0.00186	0.00175	0.00182	0.00179
$E_1 \text{ (kJ mol}^{-1}\text{)}$	−12.1	−12.2	−12.1	−12.1
α_2	-	0.083	0.0003	0.0235
$A_2 \text{ (K}^{1/2} \text{ bar}^{-1}\text{)}$	-	0.00347	0.0146	0.00462
$E_2 \text{ (kJ mol}^{-1}\text{)}$	-	−10.8	−7.73	−10.0
α_3	-	-	0.0005	0.0012
$A_3 \text{ (K}^{1/2} \text{ bar}^{-1}\text{)}$	-	-	0.228	0.0233
$E_3 \text{ (kJ mol}^{-1}\text{)}$	-	-	−1.41	−6.59
α_4	-	-	-	0.0003
$A_4 \text{ (K}^{1/2} \text{ bar}^{-1}\text{)}$	-	-	-	0.0730
$E_4 \text{ (kJ mol}^{-1}\text{)}$	-	-	-	−3.73
RMSE (mmol g ^{−1})	0.0432	0.0432	0.0432	0.0432

Table S5. Best-fit global Langmuir model parameters for single- (SL) to four- (4L) site Langmuir models of CH₄ adsorption on MOF-5 under “loose com.” fitting conditions (where only $n_{max} = 30.2 \text{ mmol g}^{-1}$ and $V_{max} = 1.30 \text{ mL g}^{-1}$ were fixed).

Fitting Parameter	Single-Site	Double-Site	Three-Site	Four-Site
$n_{max} \text{ (mmol g}^{-1}\text{)}$	31.2	31.2	31.2	31.2
$V_{max} \text{ (mL g}^{-1}\text{)}$	1.30	1.30	1.30	1.30
α_1	1	0.908	0.793	0.9094
$A_1 \text{ (K}^{1/2} \text{ bar}^{-1}\text{)}$	0.00203	0.00182	0.00178	0.001844
$E_1 \text{ (kJ mol}^{-1}\text{)}$	−11.5	−12.2	−12.2	−12.2
α_2	-	0.092	0.116	0.0003
$A_2 \text{ (K}^{1/2} \text{ bar}^{-1}\text{)}$	-	6.86E-5	0.00231	0.00247
$E_2 \text{ (kJ mol}^{-1}\text{)}$	-	−0.505	−11.7	−0.171
α_3	-	-	0.091	0.0538
$A_3 \text{ (K}^{1/2} \text{ bar}^{-1}\text{)}$	-	-	3.66E-5	2.37E-5
$E_3 \text{ (kJ mol}^{-1}\text{)}$	-	-	−0.00481	−0.0601
α_4	-	-	-	0.0365
$A_4 \text{ (K}^{1/2} \text{ bar}^{-1}\text{)}$	-	-	-	1.92E-5
$E_4 \text{ (kJ mol}^{-1}\text{)}$	-	-	-	0.0310
RMSE (mmol g ^{−1})	0.00560	0.00459	0.00459	0.00459

Table S6. Best-fit global Langmuir model parameters four-site Langmuir (4L) models of CH₄ adsorption on MOF-5 under “tight α com.” (where n_{max} , V_{max} , and α_i were fixed), “tight E com.” (where n_{max} , V_{max} , and E_i were fixed), and “fixed com.” (where n_{max} , V_{max} , α_i , and E_i were fixed) fitting conditions.

Fitting Parameter	Four-Site “Tight α_i ”	Four-Site “Tight E_i ”	Four-Site “Fixed”
n_{max} (mmol g ⁻¹)	31.2	31.2	31.2
V_{max} (mL g ⁻¹)	1.30	1.30	1.30
α_1	0.5	0.149	0.167
A_1 (K ^{1/2} bar ⁻¹)	0.000952	7.50E-5	6.56E-5
E_1 (kJ mol ⁻¹)	-13.5	-18.9	-18.9
α_2	0.25	0.498	0.5
A_2 (K ^{1/2} bar ⁻¹)	0.00320	0.00193	0.00196
E_2 (kJ mol ⁻¹)	-11.0	-12.1	-12.1
α_3	0.167	0.264	0.25
A_3 (K ^{1/2} bar ⁻¹)	0.00527	0.00792	0.00808
E_3 (kJ mol ⁻¹)	-9.91	-9.0	-9.0
α_4	0.083	0.089	0.083
A_4 (K ^{1/2} bar ⁻¹)	4.12E-9	7.90E-7	8.99E-8
E_4 (kJ mol ⁻¹)	-0.00046	-2.1	-2.1
RMSE (mmol g ⁻¹)	0.0461	0.0461	0.0461

Best-Fit Parameters for Subcritical SL Model:Table S7. Best-fit global Langmuir model parameters for single- (SL) site Langmuir model of CH₄ adsorption on MOF-5 under subcritical conditions

Fitting Parameter	Single-Site
n_{\max} (mmol g ⁻¹)	9.98
V_{\max} (mL g ⁻¹)	0.0001
α_1	1
A_1 (K ^{1/2} bar ⁻¹)	0.00263
E_1 (kJ mol ⁻¹)	-12.1
RMSE (mmol g ⁻¹)	0.0187

Plots of Supercritical Adsorption Fitting Experiments:

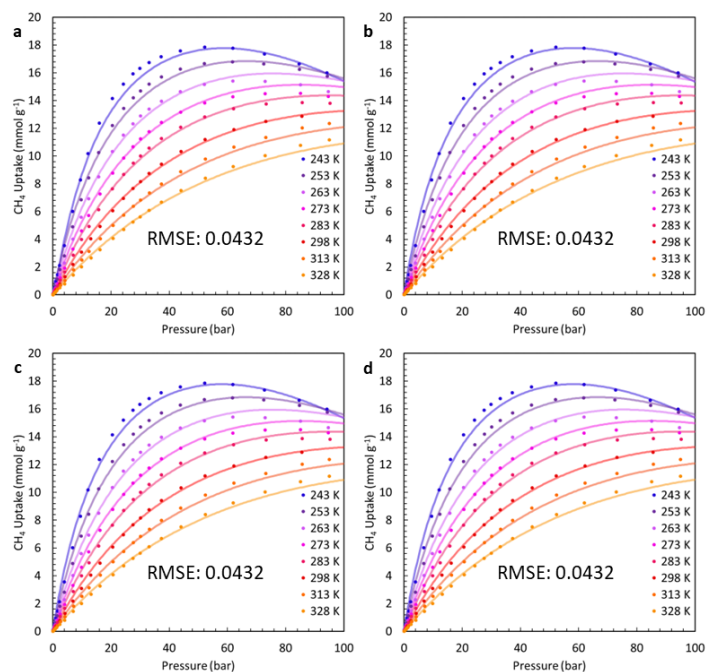


Figure S3. Equilibrium excess uptake (circles) of CH₄ on MOF-5 between 243-328 K and 0-100 bar fitted by a series of “blind* exp.” ($V_{max} = 1.47 \text{ mmol g}^{-1}$) Langmuir models (lines) with varying complexity: (a) SL, (b) 2L, (c) 3L, and (d) 4L.

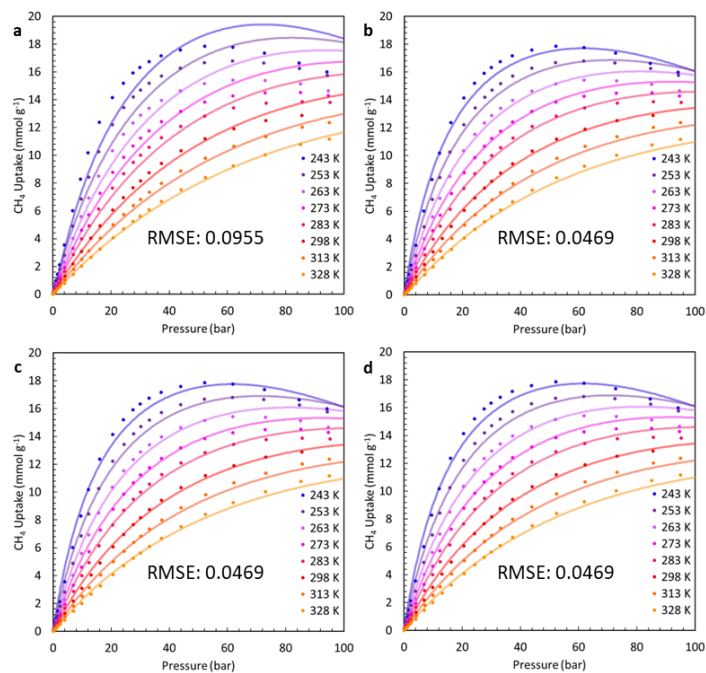


Figure S4. Equilibrium excess uptake (circles) of CH_4 on MOF-5 between 243-328 K and 0-100 bar fitted by a series of “loose exp.” ($n_{\max} = 36.1 \text{ mmol g}^{-1}$ and $V_{\max} = 1.47 \text{ mmol g}^{-1}$) Langmuir models (lines) with varying complexity: (a) SL, (b) 2L, (c) 3L, and (d) 4L.

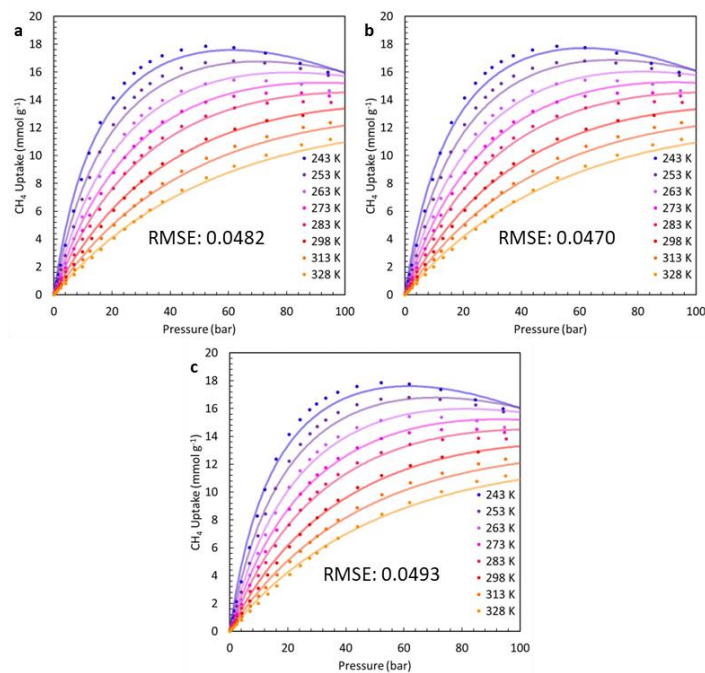


Figure S5. Equilibrium excess uptake (circles) of CH₄ on MOF-5 between 243-328 K and 0-100 bar fitted by a series of (a) “tight α exp.” (where n_{max} , V_{max} , and α_i were fixed), (b) “tight E exp.” (where n_{max} , V_{max} , and E_i were fixed), and (c) “fixed exp.” (where n_{max} , V_{max} , α_i , and E_i were fixed).

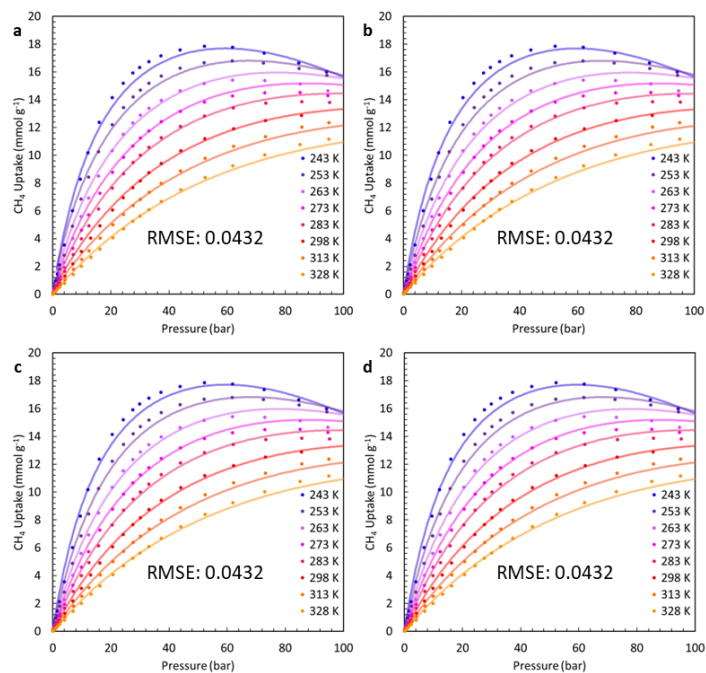


Figure S6. Equilibrium excess uptake (circles) of CH₄ on MOF-5 between 243-328 K and 0-100 bar fitted by a series of “blind* com.” ($V_{max} = 1.30 \text{ mmol g}^{-1}$) Langmuir models (lines) with varying complexity: (a) SL, (b) 2L, (c) 3L, and (d) 4L.

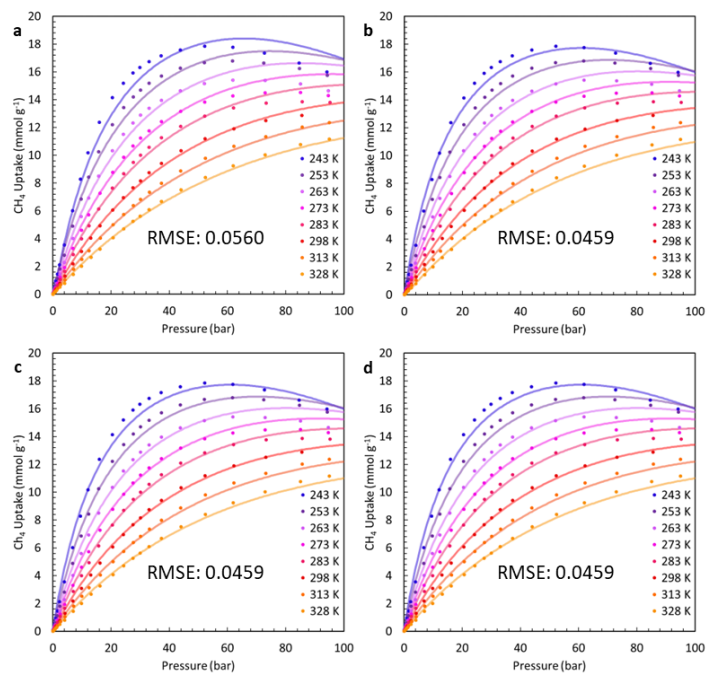


Figure S7. Equilibrium excess uptake (circles) of CH₄ on MOF-5 between 243-328 K and 0-100 bar fitted by a series of “loose com.” ($n_{max} = 31.2 \text{ mmol g}^{-1}$ and $V_{max} = 1.30 \text{ mmol g}^{-1}$) Langmuir models (lines) with varying complexity: (a) SL, (b) 2L, (c) 3L, and (d) 4L.

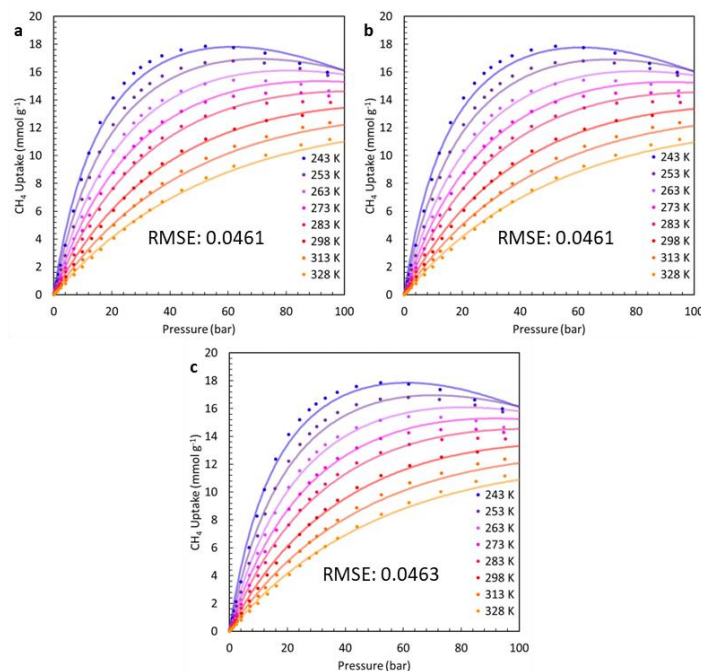


Figure S8. Equilibrium excess uptake (circles) of CH₄ on MOF-5 between 243-328 K and 0-100 bar fitted by a series of (a) “tight α com.” (where n_{max} , V_{max} , and α_i were fixed), (b) “tight E com.” (where n_{max} , V_{max} , and E_i were fixed), and (c) “fixed com.” (where n_{max} , V_{max} , α_i , and E_i were fixed).

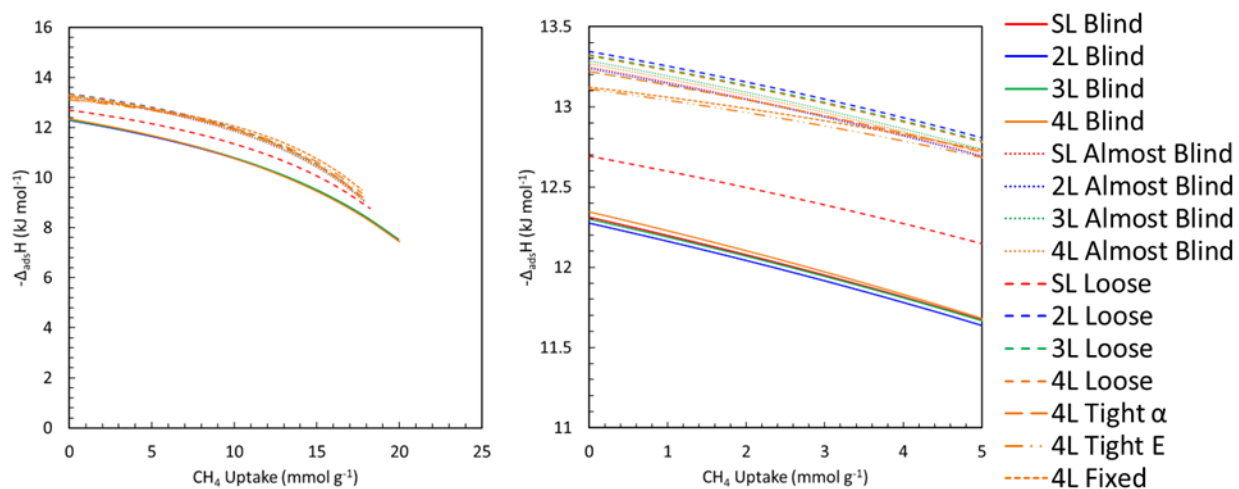


Figure S9. Isosteric heat of adsorption of CH₄ on MOF-5 at 279 K and 0-100 bar based on all fitting experiments in this study (where $n_{max} = 31.2 \text{ mmol g}^{-1}$ and $V_{max} = 1.30 \text{ mmol g}^{-1}$). Model type and fitting method are indicated by color.

A/E Parameter Correlation Analysis: Using the A_i and E_i from all of the Langmuir fits there is a clear correlation between these two variables. Figure S10 shows this correlation with the omittance of some points that were deemed outliers by visual inspection. By fitting the selected points in red to a logarithmic relationship there is clear correlation defined by Equation S3. This correlation is spurious and is unknown where it originates from. This investigation is outside of the scope of this work and will be the focus of future experiments.

$$E_i (\text{kJ mol}^{-1}) = -2.18 \ln A_i (\text{K}^{1/2} \text{ bar}^{-1}) - 1.77 \quad \text{Eq. S1}$$

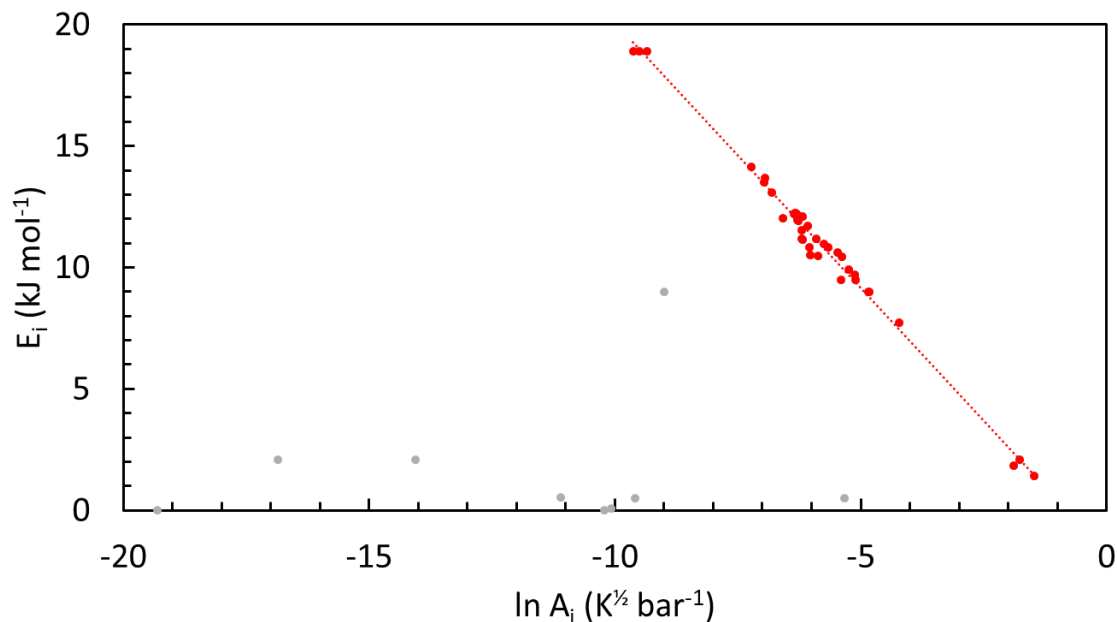


Figure S10. Logarithmic correlation between A_i and E_i of all the Langmuir fits from both computational set values and experimental set values. Points in grey have been omitted from the correlation fit due to them being deemed outliers by visual inspection.

Plots of Subcritical Methane Adsorption Fitting Experiments:

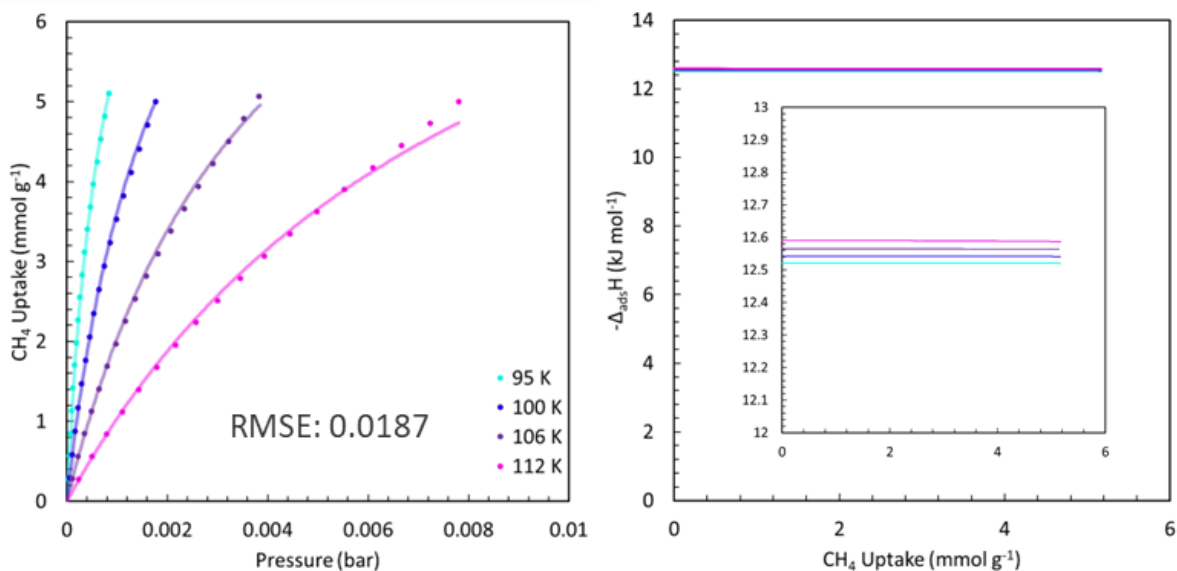


Figure S11. Equilibrium excess uptake (circles) of CH₄ on MOF-5 between 95-112 K and 0-0.01 bar globally fitted by a single-site Langmuir model with a temperature dependence of $T^{-0.5}$ (lines).

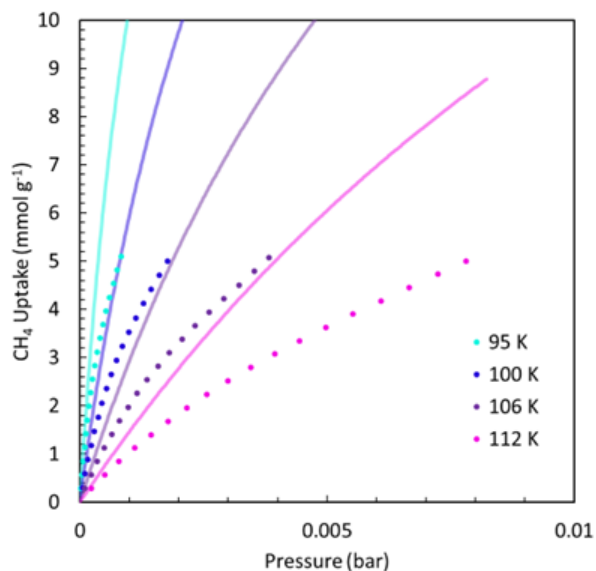


Figure S12. Equilibrium excess uptake (circles) of CH₄ on MOF-5 between 95-112 K and 0-0.01 bar compared to extrapolated 4L "blind fit" of the supercritical equilibria (lines).

References

- (1) Langmuir, I. The Constitution and Fundamental Properties of Solids and Liquids. Part I. Solids. *J. Am. Chem. Soc.* **1916**, *38* (11), 2221–2295. DOI: 10.1021/ja02268a002.
- (2) Langmuir, I. The Constitution and Fundamental Properties of Solids and Liquids. Part II. Liquids. *J. Chem. Soc.* **1917**, *184* (5), 721. DOI: 10.1021/ja02254a006.
- (3) Langmuir, I. The Adsorption of Gases on Plane Surfaces of Glass, Mica and Platinum. *J. Am. Chem. Soc.* **1918**, *40* (9), 1361–1403. DOI: 10.1021/ja02242a004.
- (4) Swenson, H. Stadie, N. P. Langmuir’s Theory of Adsorption: A Centennial Review. *Langmuir* **2019**, *35* (16), 5409–5426. DOI: 10.1021/acs.langmuir.9b00154.
- (5) Brunauer, S.; Emmett, P. H.; Teller, E. Adsorption of Gases in Multimolecular Layers. *J. Am. Chem. Soc.* **1938**, *60* (2), 309–319. DOI: 10.1021/ja01269a023.
- (6) Compton, D.; Chui, N. C.; Stylianou, K. C.; Stadie, N. P. The Temperature Dependence of the Langmuir Adsorption Model in a Single Site Metal-Organic Framework. *Langmuir* **2025**, accepted.
- (7) Purewal, J.; Liu, D.; Sudik, A.; Veenstra, M.; Yang, J.; Maurer, S.; Müller, U.; Siegel, D. J. Improved Hydrogen Storage and Thermal Conductivity in High Density MOF-5 Composites. *J. Phys. Chem. C* **2012**, *116* (38), 20199–20212. DOI: 10.1021/jp305524f.
- (8) Stadie, N. P. Synthesis and Thermodynamic Studies of Physisorptive Energy Storage Materials. Ph. D. Dissertation, California Institute of Technology, Pasadena, CA, 2012. <https://thesis.library.caltech.edu/7198/>.
- (9) Stadie, N. P.; Murialdo, M.; Ahn, C. C.; Fultz, B. Anomalous Isosteric Enthalpy of Adsorption of Methane on Zeolite-Templated Carbon. *J. Am. Chem. Soc.* **2013**, *135* (3), 990–993. DOI: 10.1021/ja311415m.
- (10) Stadie, N. P.; Murialdo, M.; Ahn, C. C.; Fultz, B. Unusual Entropy of Adsorbed Methane on Zeolite-Templated Carbon. *J. Phys. Chem. C* **2015**, *119* (47), 26409–26421. DOI: 10.1021/acs.jpcc.5b05021.
- (11) Quine, C. M.; Taylor, E. E.; Compton, D.; Gabe, A.; Nishihara, H.; Strange, N. A.; Ahn, C. C.; Fultz, B. T.; Stadie, N. P. Record Methane Storage and Delivery from Ultrasoft Ordered Microporous Carbon Monoliths with Tunable Porosity. **2025**.
- (12) Farha, O. K.; Hupp, J. T. Rational Design, Synthesis, Purification, and Activation of Metal-Organic Framework Materials. *Acc. Chem. Res.* **2010**, *43* (8), 1166–1175.

- (13) Eddaoudi, M.; Kim, J.; Rosi, N.; Vodak, D.; Wachter, J.; O’Keeffe, M.; Yaghi, O. M. Systematic Design of Pore Size and Functionality in Isoreticular MOFs and Their Application in Methane Storage. *Science* **2002**, 295 (5554), 469-472. DOI: 10.1126/science.1067208.
- (14) Casco, M. E.; Martinez-Escandell, M.; Gadea-Ramos, E.; Kaneko, K.; Silvestre-Albero, J.; Rodriguez-Reinoso, F. High-Pressure Methane Storage in Porous Materials: Are Carbon Materials in the Pole Position? *Chem. Mat* **2015**, 27 (3), 959–964. DOI: 10.1021/cm5042524.
- (15) Tian, T.; Zeng, Z.; Vulpe, D.; Casco, M. E.; Divitini, G.; Midgley, P. A.; Silvestre-Albero, J.; Tan, J.C.; Moghadam, P. Z.; et. al. A sol-gel monolithic metal-organic framework with enhanced methane uptake. *Nat. Mater* **2018**, 17 (2), 174-179. DOI: 10.1038/nmat5050.
- (16) Peng, Y.; Krungleviciute, V.; Eryazici, I.; Hupp, J. T.; Farha, O. K.; Yildirim, T. Methane Storage in Metal-Organic Frameworks: Current Records, Surprise Findings, and Challenges. *J. Am. Chem. Soc.* **2013**, 135 (32), 11887-11894. DOI: 10.1021/ja4045289.
- (17) Connolly, B. M.; Madden, D. G.; Wheatley, A. E. H.; Fairen-Jimenez, D. Shaping the Future of Fuel: Monolithic Metal-Organic Frameworks for High-Density Gas Storage. *J. Am. Chem. Soc.* **2020**, 142 (19), 8541-8549. DOI: 10.1021/jacs.0c00270.
- (18) Hui, W.; Zhou W.; Yildirim T. Methane Sorption in Nanoporous Metal-Organic Frameworks and First Order Phase Transition of Confined Methane. *J. Phys. Chem. C* **2009**, 113 (7), 3029-3035. DOI: 10.1021/jp8103276.
- (19) Tsivion E.; Head-Gordon M. Methane Storage: Molecular Mechanisms Underlying Room-Temperature Adsorption in $\text{Zn}_4\text{O}(\text{BDC})_3$ (MOF-5). *J. Phys. Chem. C* **2017**, 121 (22), 12091-12100. DOI: 10.1021/acs.jpcc.7b04246.
- (20) Li, H.; Eddaoudi, M.; O’Keeffe, M.; Yaghi, O. M. Design and synthesis of an exceptionally stable and highly porous metal-organic framework. *Nature* **1999**, 402, 276-279. DOI: 10.1038/46248.
- (21) Wang, Z. Temperature Dependence of Gas Physisorption Energy: Experimental and Computational Studies of Krypton on Porous Carbon. Ph. D. Thesis, California Institute of Technology, Pasadena, CA, 2023. <https://thesis.library.caltech.edu/15222/>.
- (22) Gibbs, J. W. On the Equilibrium of Heterogeneous Substances. *Trans. Conn. Acad.* 1876, III, 108–248 and 343–524.

- (23) Lemmon, E.; Huber, M.; McLinden, M. *NIST Standard Reference Database 23: Reference Fluid Thermodynamic and Transport Properties-REFPROP, Version 9.1*; National Institute of Standards and Technology, 2013.
<https://www.nist.gov/publications/nist-standard-reference-database-23-reference-fluid-thermodynamic-and-transport>.
- (24) Parilla, P. A.; Gross, K.; Hurst, K.; Gennett, T. Recommended volumetric capacity definitions and protocols for accurate standardized and unambiguous metrics for hydrogen storage materials. *Appl. Phys. A* **2016**, *122*, 201. DOI: 10.1007/s00339-016-9654-1.
- (25) Rouquerol, J.; Llewellyn, P.; Rouquerol, F. Is the Bet Equation Applicable to Microporous Adsorbents? *Studies in Surface Science and Catalysis*; Elsevier 2007; Vol. 160, pp 49–56. DOI: 10.1016/S0167-2991(07)80008-5.
- (26) Bowman Jr., R. C. ; Luo C. H.; Ahn, C. H.; Witham, C. K.; Fultz, B. T. The effect of tin on the degradation of $\text{LaNi}_{5-y}\text{Sn}_y$ metal hydrides during thermal cycling. *J. Alloys Compd.* **1995**, *217* (2), 185-192. DOI: 10.1016/0925-8388(94)01337-3.
- (27) Quine, C. M. REal Adsorption Langmuir Isotherms for Sorption Theory: REALIST. *Github*. <https://github.com/cullenmq/REALIST> (accessed 2025-03-30).
- (28) Willems, T. F.; Rycroft, C. H.; Kazi, M.; Meza, J. C.; Haranczyk, M. Algorithms and tools for high-throughput geometry-based analysis of crystalline porous materials. *Microporous Mesoporous Mat.* **2012**, *149* (1), 134-141, DOI: 10.1016/j.micromeso.2011.08.020.
- (29) Wu, H.; Simmons, J. M.; Liu, Y.; Brown, C. M.; Wang X.; Ma, S.; Peterson, V. K.; Southon, P. D.; Kepert, C. J.; Zhou, H.; et. al. Metal-Organic Frameworks with Exceptionally High Methan Uptake: Where and How is Methane Stored? *Chem. Eur. J.* **2010**, *16* (17), 5205-5214. DOI: 10.1002/chem.200902719.
- (30) He, Y.; Zhou, W.; Qian, G.; Chen, B. Methane storage in metal-organic frameworks. *Chem. Soc. Rev.* **2014**, *43* (16), 5657-5678. DOI: 10.1039/C4CS00032C.
- (31) Chakraborty, A.; Saha, B. B.; Koyama, S.; Ng, K. C. On the Thermodynamic modeling of the isosteric heat of adsorption and comparison with experiments. *Appl. Phys. Lett.* **2006**, *89*, 171901. DOI: 10.1063/1.2360925
- (32) Cao, D. V. ; Sircar, S. Temperature Dependence of the Isosteric Heat of Adsorption. *Adsorption Science & Technology* **2001**, *19* (10), 887-894. DOI: 10.1260/0263617011494646
- (33) Al-Muhtaseb, S. A.; Ritter, J. A. A Statistical Mechanical Perspective on the Temperature Dependence of the Isosteric Heat of Adsorption and Adsorbed Phase Heat Capacity. *J. Phys. Chem. B* **1999**, *103* (38), 8104-8115. DOI: 10.1021/jp990556c

CHAPTER FIVE

CONFINEMENT EFFECTS ON ISOSTERIC HEAT OF
METHANE ADSORPTION ON POROUS CARBONS

Contribution of Authors and Co-Authors

Manuscript in Chapter 5

Author: Dalton Compton

Contributions: Collected adsorption isotherms, analyzed data, produced figures, and wrote the manuscript.

Co-Author: Cullen M. Quine

Contributions: Collected adsorption isotherms, developed data analysis package, and assisted in editing the manuscript.

Co-Author: Emmanuel U. Osuagwu

Contributions: Aided in computational experiments and data analysis, assisted in writing and editing the manuscript.

Co-Author: Xin Shao

Contributions: Aided in computational experiments and data analysis, and editing the manuscript.

Co-Author: Robert Szilagy

Contributions: Aided in computational experiments and data analysis, assisted in writing and editing the manuscript.

Co-Author: Matthew Hill

Contributions: Synthesized Materials and editing the manuscript.

Co-Author: Hirotomo Nishihara

Contributions: Synthesized Materials and editing the manuscript.

Co-Author: Channing C. Ahn

Contributions: aided in interpretation of results and editing the manuscript.

Co-Author: Brent T. Fultz

Contributions: aided in interpretation of results and editing the manuscript.

Co-Author: Nicholas P. Stadie

Contributions: Oversaw experimental design, aided in interpretation of results, and assisted in writing and editing the manuscript.

Manuscript Information

Dalton Compton¹, Cullen Quine², Emmanuel U. Osuagwu¹, Xin Shao³, Robert Szilagyi³, Matthew Hill⁴, Shengqian Ma⁵, Hirotomo Nishihara⁶, Channing C. Ahn², Brent Fultz², Nicholas P. Stadie^{1*}

¹ Department of Chemistry and Biochemistry, Montana State University, Bozeman, Montana, 59717, United States

² W. M. Keck Laboratories, California Institute of Technology, Pasadena, California, 91125, United States

³ Department of Chemistry, University of British Columbia – Okanagan, Kelowna, British Columbia, Canada

⁴ Monash University, Melbourne, Australia

⁵ University of North Texas, Denton, Texas, 76201, United States

⁶ Tohoku University, Sendai, Japan

Status of Manuscript:

- ☒ Prepared for submission to a peer-reviewed journal
- ☐ Officially submitted to a peer-reviewed journal
- ☐ Accepted by a peer-reviewed journal
- ☐ Published in a peer-reviewed journal

Abstract

Densification, storage, and delivery of methane on porous carbonaceous solids are of critical interest for energy applications, but a lack of crystalline materials comprised mainly of carbon prevents simple calculations and understanding of their properties and ultimate upper limits of performance. While gravimetric capacity and volumetric densification factors are two crucial metrics of performance, the thermodynamic property of importance is the isosteric heat of adsorption, a measurable proxy for the methane binding energy. Past results have shown that exclusively microporous carbons with a tailored pore width of ~ 1.2 nm exhibit an increasing isosteric heat upon methane loading, lending exceptionally high adsorption uptake capacity and delivery. Two different hypotheses as to the origin of this effect exist (surface homogeneity vs. pore confinement), but no controlled investigation has been reported to resolve between them. In this work, we present a series of high-pressure methane adsorption studies on five model carbons with locally defined structures and a corresponding new series of computational models to shed atomistic insights on methane–carbon and methane–methane binding interactions. The results show that methane–methane interactions are clearly linked to the presence of three-ring binding sites in optimized confinement environments, permitting a maximum of ~ 3 kJ mol⁻¹ increase in isosteric heat as a function of loading.

Introduction

Methane adsorption has been an intense topic of experimental research as well as computational research over the past few decades due to the rise of importance of natural gas as an economical fuel. Natural gas contains $\sim 95\%$ methane^{1,2} and accounts for $\sim 30\%$ of the energy

used in the United States, with ~40% of that energy used for electric power production and the remaining used for residential and commercial heating; only ~0.2% of that total methane is used for transportation.³ While natural gas is lower in cost, yields higher combustion energy per unit mass, and results in less greenhouse gas emissions per unit energy, its volumetric energy density is significantly lower than liquid hydrocarbons like gasoline and diesel, restricting its applicability as a primary transportation fuel.⁴ For example, compressed natural gas (at 250 bar) and liquified natural gas (at 112 K) exhibit lower heating values (LHVs) of 9.4 and 22.2 MJ L⁻¹, respectively, while gasoline and diesel exhibit far higher LHVs at ambient conditions: 34.2 and 37.3 MJ L⁻¹, respectively. A strategy to increase the energy density of natural gas at ambient conditions is to use a high-pressure tank filled with a high surface area adsorbent that increases the density of fuel while taking up little space itself. The United States Department of Energy (DOE) specifies a target of 263 V/V (9.4 MJ L⁻¹) for adsorbed natural gas at ambient temperature and 65 bar, hence achieving the same density as compressed methane at 250 bar.⁵

Two main classifications of porous materials are of highest interest to achieve the densification of methane needed to meet the DOE target while remaining lightweight enough to avoid a prohibitive gravimetric penalty: high surface area carbons and metal-organic frameworks (MOFs). While porous carbons are derived from abundant feedstocks and can be synthesized by well-established, large-scale methods,⁶ the majority of carbon materials have little or no local ordering to their structure. Control of porous carbon structure is a topic of active research, with several prominent strategies: templating⁷, reticular organic chemistry⁸, polymerization of structural monomers,⁹ and carbonization of structural monomers¹⁰. A small number of these materials exhibit both high surface area and low skeletal density, with an appropriate pore size

for methane storage (~ 10 Å, permitting two CH₄ molecules per pore width, or one CH₄ per surface site)¹¹. Notable materials in this category are zeolite-templated carbon (ZTC)¹² and the porous aromatic framework referred to as PAF-1¹³; both materials exhibit ultrahigh surface area, a pore size of ~ 1.2 nm, and no π -stacking of their aromatic fragments (i.e., all carbon atoms are located at a double-sided, gas-accessible surface). In particular, ZTC has been investigated extensively as a methane storage medium, demonstrating exceptionally high densification factors over compressed methane at ambient temperature.¹⁴⁻²¹ Methane adsorption studies of PAF-1 (and related materials) are fewer but also demonstrate high capacities, though interpenetration of the porous network of PAF-1 is a limiting factor in its deployment for gas storage.^{22,23} On the other hand, MOFs are highly tunable porous materials comprised of metal oxo- or nitrido- nodes precisely connected by organic linkers, permitting a wide range of pore size and extremely high surface area.²⁴ Interestingly, the original MOF (referred to as MOF-5)²⁵ remains a top contender for hydrogen storage owing to its extremely efficient use of space.^{26,27} Determining the number and thermodynamic properties of each binding site in a crystalline MOF is possible by copious methods, especially neutron diffraction²⁸ and computational chemistry²⁹, while experimental modeling of the sites relying exclusively on measured adsorption isotherms is challenging.³⁰ For carbon materials, only the latter is strictly possible, making the determination of thermodynamic properties of methane adsorption on carbon surfaces an important area of research.

The isosteric enthalpy (or “heat”) of adsorption ($q_{st} = -\Delta_{ads}H$) is a commonly reported metric that is a proxy for the average binding energy of an adsorption system. It is offset from the change in energy upon adsorption by the change in the product of Pv :

$$\Delta_{ads}H = \Delta_{ads}U + \Delta_{ads}Pv \quad \text{Eq. 1}$$

where H is (molar) enthalpy, U is (molar) internal energy, P is pressure, and v is (molar) volume. In a simple adsorption system consisting of a collection of identical, disparate binding sites and where the bulk adsorbate fluid is an ideal gas, this simplifies to approximately:

$$\Delta_{ads}H \approx \varepsilon - RT \quad \text{Eq. 2}$$

where ε is the (molar) binding energy at each site, R is the gas constant, and T is the temperature. Hence, the isosteric heat of adsorption is a function of both temperature and pressure, but neither dependence is strong for a simplified homogeneous material. In reality, two effects contribute to a change in isosteric heat with pressure (i.e., with surface site occupancy): binding site heterogeneity and adsorbate–adsorbate interactions between sites. The former effect is present in nearly every material, including porous carbons and MOFs, and results in a decreasing isosteric heat with increasing site occupancy. The latter effect is also present in most adsorption systems, but is usually negligible and, if present, completely masked by the former effect. Materials with a high degree of homogeneity can in principle exhibit an increase in the isosteric heat of adsorption as a function of site occupancy, but few materials exhibit both close enough binding sites and a homogeneous enough distribution of site energies to realize this effect. We previously reported the increasing heat of adsorption of methane on ZTC¹⁴ and subsequently explored the underlying reasons for this effect¹⁵, concluding that homogeneity of binding site energies was the driving property of importance. No MOF has ever been reported to exhibit this quality, owing to the presence of multiple site types in each pore and typically higher binding energies at sites too distant to participate in adsorbate–adsorbate interactions. Combining the effect of increasing isosteric heat with the atomic precision of a MOF might lead to new performance benchmarks

never before achieved, but the guiding principles for how to achieve this effect in either carbons or MOFs is lacking.

While homogeneity of binding site energy is crucial for an increasing isosteric heat of adsorption, it remains an open question as to whether confinement in the optimized pore is also necessary. In other words, does methane need to be a next-site surface neighbor or cross-pore neighbor in order to realize maximum adsorbate–adsorbate interactions and therefore an increasing q_{st} with loading? In this work, we explore the guiding principles for achieving an increasing isosteric heat on porous carbons by focusing on three properties: primary structure, confinement, and homogeneity.

Five different model porous carbons were chosen that have a complementary variety of these properties: a disordered polymeric framework based on para-dichloroxylylene (pDCX), an ordered framework based on tetraphenylmethane (PAF-1), a disordered, activated carbon (MSC-30), a graphene-like material with no microporosity referred to as graphene mesosponge (GMS), and ordered microporous ZTC. The first two materials are a disordered/ordered pair based on a single-ring (phenyl) primary unit, permitting explorations of methane binding on single ring sites under confinement. The latter three materials are based on multi-ring, graphene-like fragments with minimal or no π -stacking, permitting explorations of methane binding on up to three-ring sites under both ordered/disordered conditions as well as under confined/unconfined conditions. High-pressure methane adsorption equilibria were measured on all five materials and analyzed together with computational investigations to understand the roles of different bind site types, relative homogeneity, and confinement in ~ 1 nm pores on the isosteric heat of adsorption. Several guiding principles were discovered, namely that confinement is a requirement for

realizing an increasing isosteric heat of methane adsorption, which will serve to guide future research in adsorptive natural gas storage applications.

Experimental Methods

Materials Synthesis

Five porous carbon materials were obtained as loose powders from commercial suppliers or by chemical synthesis. An extensively characterized^{14,31-39} activated carbon (Maxsorb MSC-30, Kansai Coke & Chemicals Co.) was chosen as a representative disordered porous carbon with high surface area and unspecific structure. Archetypical faujasite-type ZTC was synthesized at Montana State University according to the previously reported method.⁴⁰ GMS was synthesized at Tohoku University according to the previously reported method.⁴¹ PAF-1 was synthesized at North Texas University according to the previously reported method.¹³ Lastly, pDCX was synthesized at Monash University according to the previously reported method.⁴² All materials were degassed under oil-free vacuum ($\leq 10^{-7}$ mbar) at 130 °C for ≥ 12 h prior to analysis. ZTC, GMS, and MSC-30 were black powders, while PAF-1 was chalky white and pDCX was burnt orange in color.

Materials Characterization

Powder X-ray diffraction (XRD) was measured under dry ambient conditions using a benchtop X-ray diffractometer (D2 Phaser, Bruker Corp.) with Cu K $\alpha_{1,2}$ radiation in reflection geometry.

Nitrogen (99.999%) adsorption/desorption uptake was measured using an automated Sieverts apparatus (3Flex, Micromeritics Corp.); the sample was held in a liquid nitrogen bath

(the boiling temperature of N₂ is 75.9 K in Bozeman, Montana). The surface area was estimated using the Brunauer-Emmett-Teller (BET) model, employing the Rouquerol consistency criteria.⁵ The pore size distribution was determined using a non-local density functional theory (NLDFIT) slit pore model (implemented using Micromeritics MicroActive software).

Adsorption Modelling

Prior to modeling, the experimental adsorption equilibria were evaluated for the significance of the conversion between excess and absolute adsorbed amount. In this study, all adsorption isotherms were fitted to a double-site Langmuir model accounting for excess adsorption, using an open-source Python package (REALIST,⁴⁴ v. 0.314). A temperature dependent, global fitting method was employed in all cases, with a T-dependence previously referred to as “-0.5”, as described in past work.³⁰ The root mean squared error (RMSE) was evaluated between the fitted (excess) uptake and the measured uptake along all isotherms, and minimized using Powell’s method. The errors of the fitting parameters were unable to be calculated for all the models and will not be shown until all have been calculated.

Computational Methods

A previously benchmarked level of density functional theory (DFT) was used for all calculations: the MN15 functional with the 6-311++G** basis set.⁴⁵

Results and Discussions

Model System Selection

To investigate the effects of primary carbon structure (i.e., local binding site environments), pore confinement, and binding energy homogeneity on the isosteric heat of

methane adsorption, five model porous carbon materials were selected. Two primary carbon structures were explored which contain distinctly different binding site types: single phenyl ring moieties that contain only one-ring type binding sites and multiring, graphene-like moieties that contain up to 3-ring sites permitting the methane molecules to assume a preferred “three-legged lander” interaction described in previous work⁴⁵. To isolate the effects of one-ring sites, two model materials were selected. The first, pDCX, is a porous polymeric material based on *p*-dichloroxylylene monomeric units (Figure 1a). The lattice structure of pDCX is completely amorphous (Figure 1f) and hence the binding sites are expected to be heterogeneous in nature and centered at a binding energy typical of one-ring interactions. A complementary material is PAF-1, which is characterized by an ordered arrangement of tetraphenylmethane monomeric subunits (Figure 1b, 1f). The methane binding sites in PAF-1 are expected to be narrowly distributed around the same binding energy as pDCX. Both materials exhibit confinement effects (Figure 1g), with pDCX containing an array of pore sizes that serve to further broaden its distribution of binding energies while PAF-1 contains a homogeneous distribution of ~ 15 Å pores.

Three additional materials based on primary carbon structures containing multiring, graphene-like moieties were selected for comparison to the one-ring systems described above. The first, MSC-30, is a well-characterized activated carbon with an exceptionally high surface area of $>3000 \text{ m}^2 \text{ g}^{-1}$, indicating that it is predominantly comprised of double-sided graphene fragments (Figure 1c). Its featureless diffraction pattern (Figure 1f) with only a broad hump centered at $d = 3.3$ Å reveals that minimal π -stacking is present, with no long range ordering, and a wide distribution of pore sizes (Figure 1g). The primary methane interaction on MSC-30 is

expected to be a three-ring “lander”, but with a broad distribution to account for the wide variety of pore sizes. A complementary material is GMS, which is synthesized by methane deposition on the outer surfaces of alumina nanoparticles to ensure that the porosity is exclusively mesoporous (~ 58 Å wide, effectively making it non-porous at supercritical conditions) (Figure 1d).⁴¹

Accordingly, its structure is amorphous with the exception of long-range, in-plane ordering characteristic of graphene (Figure 1f), ensuring copious three-ring binding sites but no effects of confinement (Figure 1g). Hence, GMS is expected to exhibit a narrow binding energy distribution centered at that of a three-ring “lander,” with the additional possibility of exhibiting next-site neighbor methane–methane interactions. Lastly, ZTC is an ordered porous carbon that is synthesized by templating within the pores of a faujasite-type zeolite, and hence consists exclusively of double-sided graphene ribbon-like fragments connected in three dimensions after removing the template (Figure 1e).⁴⁶ The pore-to-pore ordering is confirmed by XRD (Figure 1f) and is consistent with a homogeneous pore size centered at ~ 12 Å (Figure 1g). Hence, the primary methane interaction on ZTC is the three-ring “lander” type, but unlike GMS, the methane adsorbed on ZTC are permitted near-optimal cross-pore methane–methane interactions that could bolster next-site neighbor interactions. The textural properties of all five materials are summarized in Table 1.

Methane Adsorption Uptake

Excess methane adsorption equilibria were measured along eight supercritical isotherms between 238–328 K and up to 10 MPa, as shown in Figure 2. In the near-critical region of any bulk adsorbate fluid, the molar density of the adsorbed phase is similar to that of the bulk fluid, causing the excess adsorption isotherms to reach a maximum and then decrease at high

pressures. The adsorption equilibria were tabulated and globally fitted to a double-site Langmuir equation with a temperature dependence of the Langmuir constant of $T^{-1/2}$:

$$n_e [T, P] = (n_{max} - \rho_g [T, P] \cdot V_{max}) \left((1 - \alpha) \frac{K_1 [T] \cdot P}{1 + K_1 [T] \cdot P} + \alpha \frac{K_2 [T] \cdot P}{1 + K_2 [T] \cdot P} \right) \quad \text{Eq. 3}$$

$$K_i [T] = \frac{A_i}{T^{1/2}} e^{-\frac{E_i}{k_B T}} \quad i = \{1, 2\} \quad \text{Eq. 4}$$

where T is the temperature, P is the pressure of the bulk adsorbate fluid, n_a is the amount adsorbed (in mmol g⁻¹), n_{tot} is the total number of adsorption sites or maximum amount adsorbed (in mmol g⁻¹), α is the fraction of the total sites of type $i = 2$, and K_i are the so-called Langmuir “constants” for each site type. The equation for K_i can be derived in several forms from first principles using statistical mechanics;³⁰ a $T^{-1/2}$ dependence of K_i (i.e., a 2D lattice gas model⁴⁷) was employed for all materials herein. The best-fit parameters are given in Table 2.

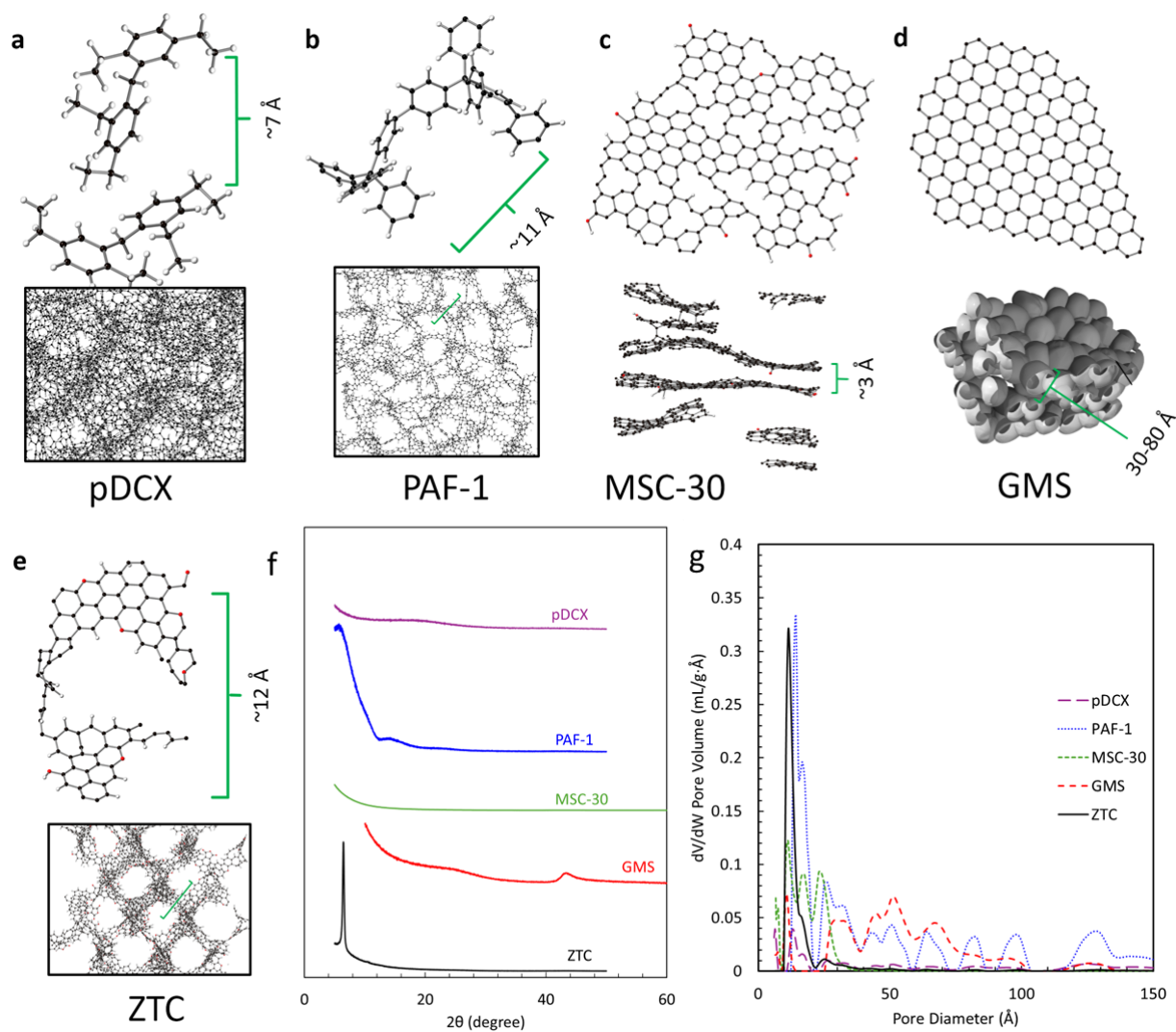


Figure 1. Materials characterization of five model porous materials: pDCX, PAF-1, MSC-30, GMS, and ZTC. (a-e) Primary structural units, (f) XRD patterns, and (g) N₂-accessible pore-size distribution.

Table 1. Textural properties of the five model materials determined via N₂ adsorption at 77 K.

Property	pDCX	PAF-1	MSC-30	GMS	ZTC
V_{tot} (mL g ⁻¹)	0.90	4.93	1.81	2.83	1.58
V_{micro} (mL g ⁻¹)	0.28	1.39	0.05	0.23	1.25
SA_{BET} (m ² g ⁻¹)	911	4955	3193	1706	3340
n_{mono} (mmol g ⁻¹)	11.0	61.2	42.4	20.8	37.4

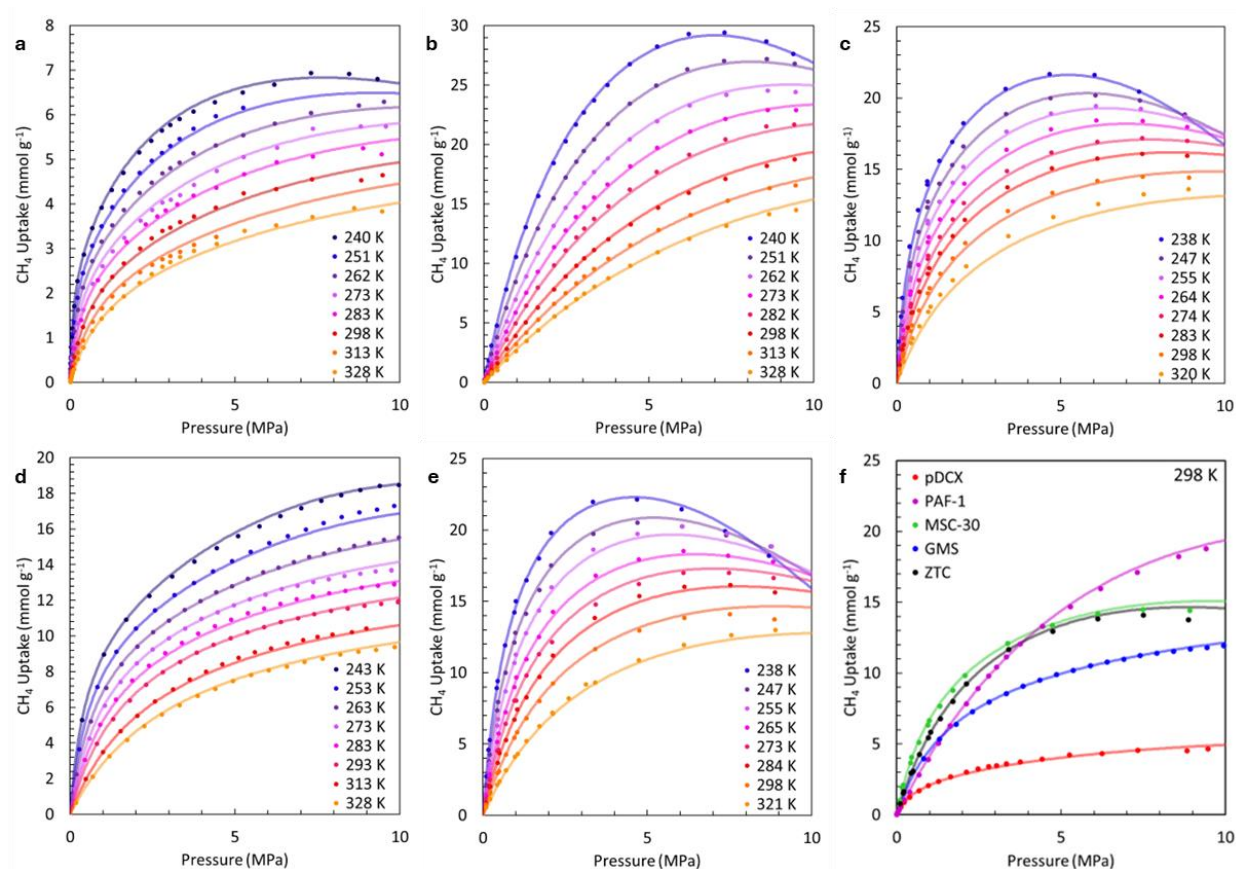


Figure 2. Equilibrium excess uptake (circles) of CH₄ on (a) pDCX, (b) PAF-1, (c) MSC-30, (d) ZTC, and (e) ZTC between 238-328 K up to 10 MPa, fitted by a double-site Langmuir model. (f) Comparison of all materials at 298 K.

Table 2. Best-fit parameters for a double-site Langmuir model fit (with a $T^{-1/2}$ temperature dependence of the Langmuir constant) to the five model materials.

Fitting Parameters	pDCX	PAF-1	MSC-30	GMS	ZTC
n_{\max} (mmol g ⁻¹)	10.1	64.9	41.7	64.1	37.6
V_{\max} (mL g ⁻¹)	0.237	3.04	2.39	1.65	2.25
α	0.766	0.502	0.717	0.832	0.462
A_1 (MPa ⁻¹)	0.0211	0.00213	0.0370	0.0369	0.000887
E_1 (kJ mol ⁻¹)	-18.4	-13.7	-14.4	-13.8	-16.9
A_2 (MPa ⁻¹)	0.00487	0.0499	0.00493	0.000765	0.0489
E_2 (kJ mol ⁻¹)	-13.8	-9.05	-12.8	-13.1	-12.2
RMSE (mmol g ⁻¹)	0.00104	0.00200	0.00338	0.00278	0.00503

The five model porous carbon materials show distinctly different maximum excess capacities, maximum absolute capacities, and characteristic isotherm shapes (which relate to the binding energy distribution). A representative comparison between all five materials at 298 K is shown in Figure 1f. For example, pDCX exhibits the lowest excess uptake capacity, as expected due to its low surface area. The highest excess uptake capacity is exhibited by PAF-1 (29.4 mmol g⁻¹), also as expected due to its extremely high surface area. Hence, excess uptake quantity per gram correlates with framework density as opposed to primary structural unit type (in this case, both one-ring type units): more of the framework of PAF-1 is exposed and available for adsorption than pDCX.

GMS exhibits a unique isotherm shape owing the presence of multilayer stacking. While the double-site Langmuir model used in this work does not strictly account for multilayer stacking, it can be used to treat such adsorption systems by invoking a high value of n_{tot} while

retaining a modest value of V_{max} (where the entire experimental dataset lies at <30% of n_{max}). On the other hand, ZTC and MSC-30 show similar isotherm shapes, both indicating an obvious excess adsorption maximum owing to the existence of a high-density adsorbed phase. These values are also loosely consistent with the three materials' surface areas, though interestingly the 298 K adsorption isotherm for MSC-30 lies entirely above that for MSC-30 despite the former's higher surface area and higher maximum excess uptake at 238 K.

Isosteric Heat of Adsorption

The isosteric enthalpy of adsorption (q_{st} or $-\Delta_{ads}H$) was calculated herein using the general Clapeyron equation as a function of both temperature and pressure (i.e., surface site occupancy) according to:

$$q_{st}[T, P] = -\Delta_{ads}H[T, P] = T \Delta_{ads}S = T \left(\frac{\partial P}{\partial T} \right)_{n_a} \Delta_{ads}v = T \left(\frac{\partial P}{\partial T} \right)_{n_a} (v_a - v_g) \quad \text{Eq. 5}$$

where the partial derivative is determined analytically from Equations 3-4. The bulk fluid molar volume (v_g) is a function of temperature and pressure and is determined by the equation of state.⁴⁸ The adsorbed phase volume (v_a) is also a function of temperature and pressure according to:

$$v_a[T, P] = V_{max} \frac{n_a[T, P]}{n_{tot}} \quad \text{Eq. 5}$$

The isosteric heat of CH₄ adsorption on all five model porous carbon materials is shown as a function of absolute uptake amount (n_a) via the common parameter P in Figure 3. Since the same Langmuir-type model was used in all cases, the magnitude of q_{st} is directly comparable between the five materials. A wide range of Henry's law values between -11.5 and -19.1 kJ mol⁻¹ is observed: the ranking of these values goes as pDCX > MSC-30 \approx GMS \approx ZTC > PAF-1.

Among the three samples with a similar binding energy of ~ 14 kJ mol $^{-1}$, the fine ranking of the Henry's law values is: MSC-30 > GMS > ZTC. However, as previously reported,¹⁴ ZTC exhibits a slight increase in isosteric heat at 243 K as a function of site occupancy, and hence the ranking at intermediate surface site occupancy is much more separated: ZTC > MSC-30 > GMS.

Interestingly, only ZTC shows any effect of increasing isosteric heat as a function of surface site occupancy.

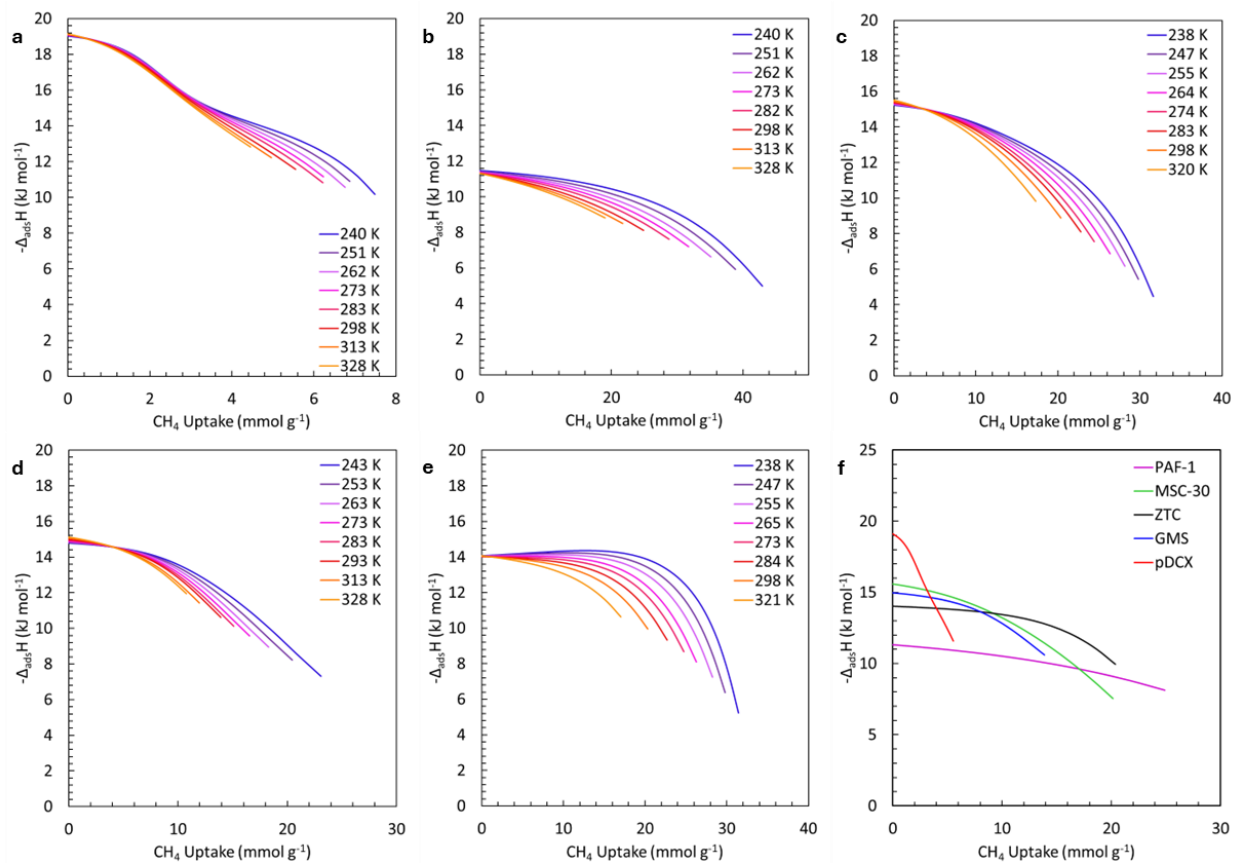


Figure 3. Isosteric enthalpy of CH₄ adsorption on (a) pDCX, (b) PAF-1, (c) MSC-30, (d) GMS, and (e) ZTC between 238-328 K and up to 10 MPa. (f) Comparison of all materials at 298 K.

Binding Site Environments

Previous computational efforts have shown that methane preferentially forms a so-called three-legged “lander” (3L) binding interaction on open carbon surfaces containing at least three six-membered aromatic rings.⁴⁵ The minimal molecular model or “maquette” designed to explore this interaction was methyldiene phenalene (MPh), an aromatic system containing three six-membered rings. In this work, several new metastable interactions were also explored, namely: a two-legged “lander” (2L) interaction, a “head down” or one-legged “lander” (1L) interaction, and an edge interaction referred to as a “clamp” (C). All four interactions were possible to be analyzed on MPh since (metastable) stationary structures could be obtained at the same benchmarked level of density functional theory (DFT) used throughout this work. The basis set superposition error- (BSSE-) corrected ranking of binding energy is in logical order: $3L > 2L > 1L > C$ (Table 3). The same interactions could also be probed on smaller moieties representing materials with smaller primary structural units such as benzene (1L and C only) and naphthalene (2L, 1L, and C), yielding similar values of binding energy. Together, these four interactions represent the main binding interactions possible on the surfaces of the five materials investigated herein, as summarized in Figure 4.

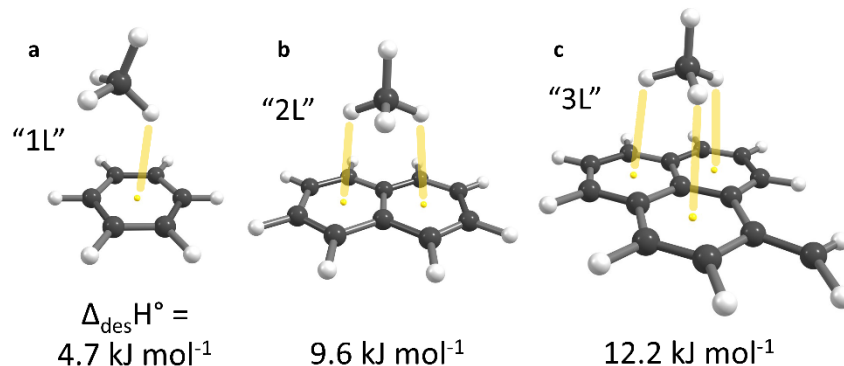


Figure 4. Binding structures and energies of 1L, 2L, and 3L adsorption interactions on flat, open carbon surfaces of increasing ring number: (a) benzene, (b) naphthalene, and (c) methylidene phenalene (MPh), respectively. The level of theory is MN15/6-311++G** and the BSSE- and ZPE-corrected SCF energy difference upon dissociation is indicated ($\Delta_{\text{des}}H^\circ$). Carbon is shown in black, hydrogen in white, and ring centroid interactions (as a guide to the eye) in yellow.

Table 3. Desorption energies (ΔE^{QM}), BSSE-corrected energies ($\Delta E^{\text{QM}*}$), BSSE/ZPE-corrected energies ($\Delta E^{\text{ZPE}*}$), and standard enthalpies ($\Delta_{\text{des}}H^\circ$) for $\text{Adsorbent} \times n\text{CH}_4 \rightarrow \text{Adsorbent} + n\text{CH}_4$ calculated using the MN15/6-311++G** level of theory (in units of kJ mol^{-1}).

Adsorbent	n	Interaction	ΔE^{QM}	$\Delta E^{\text{QM}*}$	ΔE^{ZPE}	$\Delta E^{\text{ZPE}*}$	$\Delta_{\text{des}}H^\circ$
Benzene	1	1L	9.5	8.7	7	6.2	4.7
Naphthalene	1	2L	14.3	11.8	11.1	8.6	9.6
MPh	1	3L	17.2	15.6	13.2	11.6	12.2
MPh	1	2L	14.7	12.6	11.4	9.3	9.9
MPh	1	C	5.5	5.2	2.8	2.4	0.4
2×MPh	1	2L-2L	26.3	21.3	21.7	16.6	21.6
2×MPh	2	3L-MMA-3L	35.5	30.1	27.3	21.8	30.6
DBCh	2	3L-MMS-3L	39.2	33.5	29.5	23.8	28.6

MPh = methylidene phenalene

DBCh = dibenzochrysene

In addition to primary surface interactions, confinement within narrow pore spaces plays a major role in the overall binding energy distribution of a porous material. To approximate the relative effects of such environments, two “sandwich” structures were also investigated to emulate the simplest type of pore shape: the slit pore. Out of the many possible pore widths and many possible combinations of interactions with each wall of the slit pore, the two structures representative of the optimal slit pore environments are shown in Figures 5a-5b. The methane desorption energies are summarized in Table 3. The first, referred to as a “single-width pore,” exhibits a center-to-center pore width of 7 Å and an extremely high binding energy of $\sim 22 \text{ kJ mol}^{-1}$, indicating that porous carbons with narrow pores will exhibit high binding energies and low capacities (owing to the gravimetric cost of requiring two pore wall sites per adsorbate molecule). The strongest single-width pore binding interaction comprises two distinct 2L interactions and is hence referred to as 2L-2L. The second confinement interaction of high interest, referred to as a “double-width pore,” exhibits a center-to-center pore width of 11 Å and a slightly increased binding energy of $\sim 15 \text{ kJ mol}^{-1}$, indicating that porous carbons with optimized pores will exhibit slightly increased binding energies and high capacities. The strongest double-width pore interaction comprises two distinct 3L interactions and a new methane–methane interaction in the center of the pore, referred to as MMA; hence, this entire interaction comprising both methane molecules is termed “3L-MMA-3L”. By subtraction of two 3L interactions, the MMA energy is determined to be $\sim 6 \text{ kJ mol}^{-1}$. For comparison to the strength of a methane–methane interaction on an open surface (i.e., on next-neighbor sites), referred to herein as an MMS interaction, a final model of double methane adsorption was investigated comprising two methane molecules on the same side of the surface of dibenzochrysene (DBCh),

as shown in Figure 5c. The total interaction explored in this model is referred to as 3L-MMS-3L and, by subtraction of two 3L interactions, reveals an approximate MMS energy of ~ 4 kJ mol⁻¹.

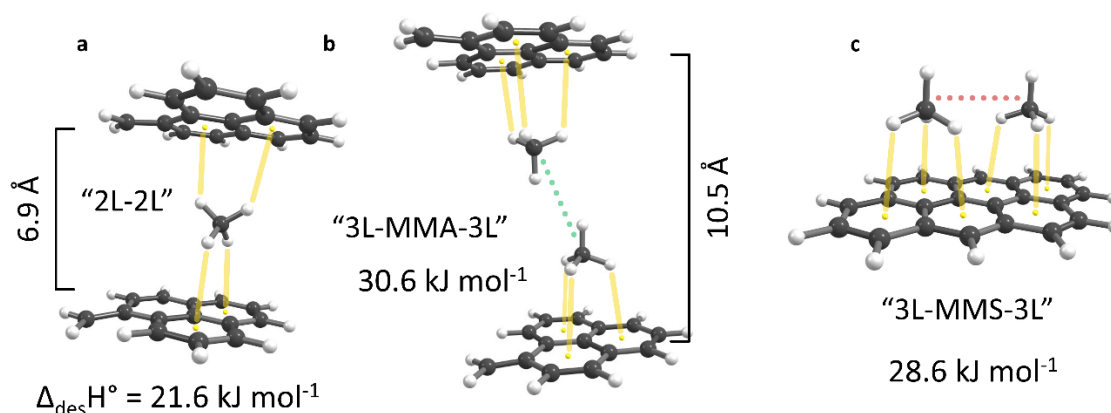


Figure 5. Binding structures and energies of 2L-2L, 3L-MMA-3L, and 3L-MMS-3L adsorption interactions in optimized scenarios: (a) within a single-width slit pore, (b) within a double-width slit pore, and (c) on an open surface, respectively. The level of theory is MN15/6-311++G** and the standard enthalpy difference upon dissociation is indicated ($\Delta_{\text{des}}H^\circ$). Carbon is shown in black, hydrogen in white, ring centroid interactions (as a guide to the eye) in yellow, and methane-methane interactions (as a guide to the eye) in green/red.

Mechanisms of Binding

A carbon material based on one-ring moieties (e.g., pDCX and PAF-1) is restricted to participating in only 1L or C type binding interactions, and hence restricted to significantly lower binding energies than those with two- or multi-ring moieties. A carbon material based on three-ring moieties or larger (e.g., MSC-30, GMS, and ZTC) can participate in any of the primary interactions identified herein (3L, 2L, 1L, and C) but, according to the binding energy, will preferentially participate in 3L interactions (space permitting). This guiding principle of methane storage material design is corroborated by the isosteric heats of adsorption of four of the five model materials measured in this work: PAF-1, MSC-30, GMS, and ZTC (Figure 3). These materials all exhibit a majority of pores of width >10 Å, where the vast majority of methane

binding interactions occur between each methane molecule and a single carbon-based surface site. At low surface site occupancy conditions, these interactions are of 3L type.

The fifth material, pDCX, exhibits a significantly increased isosteric heat of adsorption of $\sim 19 \text{ kJ mol}^{-1}$. The pore-size distribution of pDCX also exhibits a predominance of ultramicropores ($< 10 \text{ \AA}$). Together, this implies that under low surface site occupancy conditions, the majority of methane on pDCX is participating in single-width pore type interactions. While the specific 2L-2L interaction identified in this work is not strictly possible in single-ring pDCX, a similarly strong 1L-1L interaction (with additional participation of nearby polymeric segments) is likely to be accountable for the high isosteric heat measured. Upon continued methane uptake to higher surface site occupancies, lower energy 1L interactions are mixed with single-width pore interactions to contribute a steeply decreasing isosteric heat.

ZTC is unique among the materials investigated herein due to its increasing isosteric heat of adsorption at intermediate adsorption occupancies. This is likely indicative of cooperative methane–methane interactions; at low occupancies, the methane molecules on ZTC participate in disparate 3L interactions but as occupancy increases, 3L-MMA-3L type interactions are possible. The latter interactions consist of up to an extra $\sim 3 \text{ kJ mol}^{-1}$ (where the “per mole” refers to the number of methane molecules) since the MMA contribution is shared between two molecules. The experimental increase in isosteric heat of methane adsorption on ZTC is $\sim 0.5\text{-}1.1 \text{ kJ mol}^{-1}$ at 238 K, indicating that not all methane molecules in the ZTC pore system are able to participate in the optimized MMA-type interaction.

Contrarily, GMS does not exhibit an increasing isosteric heat of adsorption despite its high homogeneity of binding environments and the predominance of 3L interactions on its

surface. This can only be explained by the lower energy of cooperation on neighboring sites (MMS) as opposed to cross-pore type methane–methane interactions (MMA). Indeed, the computational investigations of 3L-MMA-3L and 3L-MMS-3L binding scenarios show that while MMA contributes up to $\sim 3 \text{ kJ mol}^{-1}$ of additional binding energy (on a per-molecule basis), the MMS cooperation is significantly lower ($\sim 2 \text{ kJ mol}^{-1}$), low enough to evade detection at supercritical conditions of relevance to energy storage applications. This is evidence that confinement within 10-12 Å pore widths is a necessary condition for an increasing isosteric heat of adsorption of methane on porous carbon adsorbents.

Conclusions

Methane adsorption was measured on five different model porous carbons at conditions of relevance to adsorption storage applications: between 238-328 K and up to 10 MPa. The experimental adsorption equilibria were globally fitted to a double-site Langmuir model with a $T^{-1/2}$ temperature dependence and the isosteric enthalpy of adsorption was determined using the Clapeyron equation. The results were compared to computational investigations of specific methane–adsorbent interactions to provide atomistic insights into methane binding on a wide range of carbons of relevance to practical applications.

Two key properties of high-performance methane storage were identified: abundant three-ring binding sites and confinement within $\sim 10 \text{ Å}$ pores. Materials comprised solely of one-ring binding sites such as pDCX and PAF-1 do not permit higher energy 3L type binding that is optimal for methane on carbon surfaces. Materials comprised of predominantly mesopores (e.g., GMS) or wide/heterogeneous micropores (e.g., MSC-30) do not permit MMA type cooperative interactions that are optimal for methane storage and especially methane delivery at near-ambient

conditions. On the other hand, ZTC exhibits a homogenous pore network centered at a width of ~ 12 Å and is comprised primarily by graphene ribbon-like struts with multiring environments that can accommodate the 3L geometry of adsorbed methane, making it an ideal material for adsorptive methane storage applications. Future work to prepare higher surface area variants of porous carbons with exclusively three-ring (or larger) structural moieties is warranted.

Associated Content

Acknowledgements

We gratefully acknowledge all those for providing the materials. This work was supported by the U.S. Department of Energy's Office of Energy Efficiency and Renewable Energy (EERE) under the Hydrogen and Fuel Cell Technologies and Vehicle Technologies Offices under Award Number DE-EE0008815.

References

- (1) Faramawy, S.; Zaki, T.; Sakr, A. A-E. Natural gas Origin, composition, and processing: A review. *J. Nat. Gas Sci. Eng.* **2016**, *34*, 34-54. DOI: 10.1016/j.jngse.2016.06.030.
- (2) Kakaee, A-H.; Paykani, A.; Ghajar, M. The influence of fuel composition on the combustion and emission characteristics of natural gas fueled engines. *Renewable Sustainable Energy Rev.* **2014**, *38*, 64-78. DOI: 10.1016/j.rser.2014.05.080.
- (3) *Monthly Energy Review March 2025*; U.S. Energy Information Administration, 2025.
- (4) Casco, M. E.; Martinez-Escandell, M.; Gadea-Ramos, E.; Kaneko, K.; Silvestre-Albero, J.; Rodriguez-Reinoso, F. High-Pressure Methane Storage in Porous Materials: Are Carbon Materials in the Pole Position. *Chem. Mater.* **2015**, *27* (3), 959-964. DOI: 10.1021/cm5042524.
- (5) *MOVE Methane Opportunities for Vehicular Energy*; U.S. Department of Energy. <https://arpa-e.energy.gov/programs-and-initiatives/view-all-programs/move> (accessed 04/14/2025).

- (6) Memetova, A.; Tyagi, I.; Karri, R. R.; Kumar, V.; Tyagi, K.; Suhas; Memetov, N.; Zelenin, A.; Pasko, T.; Gerasimova, A; et. al. Porous carbon-based material as a sustainable alternative for the storage of natural gas (methane) and biogas (biomethane): A review. *Chem. Eng. J.* **2022**, *446* (4), 137373. DOI: 10.1016/j.cej.2022.137373.
- (7) Nishihara, H.; Kyotani, T. Templated Nanocarbons for Energy Storage. *Adv. Mater.* **2012**, *24* (33), 4473-4498. DOI: 10.1002/adma.201201715.
- (8) Waller, P. J.; Gandara, F.; Yaghi, O. M. Chemistry of Covalent Organic Frameworks. *Acc. Chem. Res.* **2015**, *48* (12), 3053-3063. DOI: 10.1021/acs.accounts.5b00369.
- (9) Tian, Y.; Zhu, G. Porous Aromatic Frameworks (PAFs). *Chem. Rev.* **2020**, *120* (16), DOI: 10.1021/acs.chemrev.9b00687.
- (10) Nishihara, H.; Hirota, T.; Matsuura, K.; Ohwada, M.; Hoshino, N.; Akutagawa, T.; Higuchi, T.; Jinnai, H.; Koseki, Y.; Kasai, H.; et al. Synthesis of ordered carbonaceous frameworks from organic crystals. *Nat. Commun.* **2017**, *8*, 109. DOI: 10.1038/s41467-017-00152-z.
- (11) Cracknell, R. F.; Gordon, P.; Gubbins, K. E. Influence of Pore Geometry on the Design of Microporous Materials for Methane Storage. *J. Phys. Chem.* **1993**, *97* (2), 494-499. DOI: 10.1021/j100104a036.
- (12) Nishihara, H.; Kyotani, T. Zeolite-templated carbons – three-dimensional microporous graphene frameworks. *Chem. Commun.* **2018**, *54* (45), 5648-5673. DOI: 10.1039/c8cc01932k.
- (13) Ben, T.; Ren, H.; Ma, S.; Cao, D.; Lan, J.; Jing, X.; Wang, W.; Xu, J. ;Deng, F.; Simmons, J. M.; et al. Targeted Synthesis of a Porous Aromatic Framework with High Stability and Exceptionally High Surface Area. *Angew. Chem. Int. Ed.* **2009**, *48* (50), 9457-9460. DOI: 10.1002/anie.200904637.
- (14) Stadie, N. P.; Murialdo, M.; Ahn, C. C.; Fultz, B. Anomalous Isosteric Enthalpy of Adsorption of Methane on Zeolite-Templated Carbon. *J. Am. Chem. Soc.* **2013**, *135* (3), 990-993. DOI: 10.1021/ja311415m.
- (15) Stadie, N. P.; Murialdo, M.; Ahn, C. C.; Fultz, B. Unusual Entropy of Adsorbed Methane on Zeolite-Templated Carbon. *J. Phys. Chem. C* **2015**, *119* (47), 26409-26421. DOI: 10.1021/acs.jpcc.5b05021.
- (16) Ducrot-Boisgontier, C.; Parmentier, J.; Faour, A.; Patarin, J.; Pirngruber, G. D. FAU-Type Zeolite Nanocasted Carbon Replicas for CO₂ Adsorption and Hydrogen Purification. *Energy Fuels* **2010**, *24*, 3595-3602. DOI: 10.1021/ef/100011q.
- (17) Guan, C.; Su, F.; Zhao, X.S.; Wang. Methane storage in a template-synthesized carbon. *Sep. Purif. Technol.* **2008**, *64* (1), 124-126. DOI: 10.1016/j.seppur.2008.08.007.

- (18) Yong Liang Guana, C; Elkamel, A.; Wang, K. Energy Gas Storage in Template-Synthesized Carbons with Different Porous Structures. *Can. J. Chem. Eng.* **2015**, 93 (3), 527-531. DOI: 10.1002/cjce.22141.
- (19) Antoniou, M. K.; Diamanti, E. K.; Enotiadis, A.; Policichio, A.; Dimos, K.; Ciuchi, F.; Maccallini, E.; Gournis, D.; Agostino, R. G.; Methane storage in zeolite-like carbon materials. *Microporous Mesoporous Mater.* **2014**, 188, 16-22. DOI: 10.1016/j.micromeso.2013.12.030.
- (20) Shi, J.; Li, W.; Li, D. Rapidly reversible adsorption of methane with a high storage capacity on the zeolite templated carbons with glucose as carbon precursors. *Colloids Surf. A* **2015**, 485, 11-17. DOI: https://doi.org/10.1016/j.colsurfa.2015.08.026.
- (21) Stadie, N. P.; Fultz, F.; Ahn, C. C.; Murialdo, M. Nanostructured Carbon Materials for Adsorption of Methane and Other Gases. US9067848, 2015.
- (22) Pei, C., Ben, T., & Qiu, S. Great Prospects for PAF-1 and its derivatives. *Mater. Horiz.* **2015**, 2 (1), 11–21. DOI:10.1039/c4mh00163j.
- (23) Ben, T., Pei, C., Zhang, D., Xu, J., Deng, F., Jing, X., & Qiu, S. Gas storage in porous aromatic frameworks (PAFs). *Energy Environ. Sci.* **2011**, 4 (10), 3991. DOI:10.1039/c1ee01222c.
- (24) Farha, O. K.; Hupp, J. T. Rational Design, Synthesis, Purification, and Activation of Metal-Organic Framework Materials. *Acc. Chem. Res.* **2010**, 43 (8), 1166-1175. DOI:10.1021/ar1000617.
- (25) Li, H.; Eddaoudi, M.; O’Keeffe, M.; Yaghi, O. M. Design and synthesis of an exceptionally stable and highly porous metal-organic framework. *Nature* **1999**, 402, 276-279. DOI: 10.1038/46248.
- (26) Ahmed, A.; Liu, Y.; Purewal, J.; Tran, L. D.; Wong-Foy, A. G.; Veenstra, M.; Matzger, A. J.; Siegel, D. J. Balancing gravimetric and volumetric hydrogen density in MOFs. *Energy Environ. Sci.* **2017**, 10, 2459. DOI: 10.1039/c7ee02477k.
- (27) Samantaray, S. S.; Putnam, S. T.; Stadie, N. P. Volumetrics of Hydrogen Storage by Physical Adsorption. *Inorganics* **2021**, 9 (6), 45. DOI: 10.3390/inorganics9060045.
- (28) Hui, W.; Zhou W.; Yildirim T. Methane Sorption in Nanoporous Metal-Organic Frameworks and First Order Phase Transition of Confined Methane. *J. Phys. Chem. C* **2009**, 113 (7), 3029-3035. DOI: 10.1021/jp8103276.
- (29) Tsivion E.; Head-Gordon M. Methane Storage: Molecular Mechanisms Underlying Room-Temperature Adsorption in Zn₄O(BDC)₃ (MOF-5). *J. Phys. Chem. C* **2017**, 121 (22), 12091-12100. DOI: 10.1021/acs.jpcc.7b04246.

- (30) Compton, D.; Chui, N. C.; Stylianou, K. C.; Stadie, N. P. The Temperature Dependence of the Langmuir Adsorption Model in a Single Site Metal-Organic Framework. *Langmuir* **2025**, ASAP Article. DOI: 10.1021/acs.langmuir.5c00757.
- (31) Nishihara, H.; Hou, P. X.; Li, L. X.; Ito, M.; Uchiyama, M.; Kaburagi, T.; Ikura, A.; Katamura, J.; Kwarada, T.; Mizuuchi, K.; Kyotani, T. High-Pressure Hydrogen Storage in Zeolite-Templated Carbon. *J. Phys. Chem. C* **2009**, *113* (8), 3189-3196. DOI: 10.1021/jp808890x.
- (32) Voskuilen, T. G.; Pourpoint, T. L.; Dailly, A. M. Hydrogen adsorption on microporous materials at ambient temperatures and pressures up to 50 MPa. *Adsorption* **2012**, *18*, DOI: 10.1007/s10450-012-9397-z.
- (33) Stadie, N. P.; Purewal, J. J.; Ahn, C. C.; Fultz, B. Measurements of Hydrogen Spillover in Platinum Doped Superactivated Carbon. *Langmuir* **2010**, *26* (19), 15481-15485. DOI: 10.1021/la9046758.
- (34) Stadie, N. P.; Vajo, J. J.; Cumberland, R. W.; Wilson, A. A.; Ahn, C. C.; Fultz, B. Zeolite-Templated Carbon Materials for High Pressure Hydrogen Storage. *Langmuir* **2012**, *28* (26), 10057-10063. DOI: 10.1021/la302050m.
- (35) Burrell, J.; Bethea, D.; Troub, B. Combination volumetric and gravimetric sorption instrument for high accuracy measurements of methane adsorption. *Rev. Sci. Instrum.* **2017**, *88* (5), 053902. DOI: 10.1063/1.4982889.
- (36) Choi, S.; Alkhabbaz, M. A.; Wang, Y.; Othman, R. M.; Choi, M. Unique thermal contraction of zeolite-templated carbons enabling micropore size tailoring and its effects on methane storage. *Carbon* **2019**, *141*, 143-153. DOI: 10.1016/j.carbon.2018.09.045.
- (37) Beckner, M.; Dailly, A. Hydrogen and methane storage in adsorbent materials for automotive applications. *Int. J. Energy Res.* **2016**, *40*, 91-99. DOI: 10.1002/er.3324.
- (38) Romanos, J.; Dargham, S. A.; Roukos, R.; Pfeifer, P. Properties of adsorbed supercritical methane film in nanopores. *AIP Advances* **2018**, *8* (12), 125011. DOI: 10.1063/1.5074086.
- (39) Zhu, Q. L.; Tsumori, N.; Xu, Q. Sodium hydroxide-assisted growth of uniform Pd nanoparticles on nanoporous carbon MSC-30 for efficient and complete dehydrogenation of formic acid under ambient conditions. *Chem. Sci.* **2014**, *5* (1), 195. DOI: 10.1039/c3sc52448e.
- (40) Taylor, E. E.; Garman, K.; Stadie, N. P. Atomistic Structures of Zeolite-Templated Carbon. *Chem. Mater.* **2020**, *32* (7), 2742-2752. DOI: 10.1021/acs.chemmater.0c00535.

- (41) Nishihara, H.; Simura, T.; Kobayashi, S.; Nomura, K.; Berenguer, R.; Ito, M.; Uchimura M.; Iden, H.; Arihara, K.; Ohma, A.; et al. Oxidation-Resistant and Elastic Mesoporous Carbon with Single-Layer Graphene Walls. *Adv. Funct. Mater.* **2016**, *26* (35), 6418-6427. DOI: 10.1002/adfm.201602459.
- (42) Wood, C. D.; Tan, B.; Trewin, A.; Niu, H.; Bradshaw, D.; Rosseinsky, M. J.; Khimyak, Y. Z.; Campbell, N. L.; Kirk, R.; Stöckel, E. Hydrogen Storage in Microporous Hypercrosslinked Organic Polymer Networks. *Chem. Mater.* **2007**, *19* (8), 2034-2048. DOI: 10.1021/cm070356a.
- (43) Bowman Jr., R. C. ; Luo C. H.; Ahn, C. H.; Witham, C. K.; Fultz, B. T. The effect of tin on the degradation of LaNi₅-ySny metal hydrides during thermal cycling. *J. Alloys Compd.* **1995**, *217* (2), 185-192. DOI: 10.1016/0925-8388(94)01337-3.
- (44) Quine, C. M. REal Adsorption Langmuir Isotherms for Sorption Theory: REALIST. *Github*. <https://github.com/cullenmq/REALIST> (accessed 2025-03-30).
- (45) Rowsey, R.; Taylor, E. E.; Irle, S.; Stadie, N. P.; Szilagyi, R. K. Methane Adsorption on Heteroatom-Modified Maquettes of Porous Carbon Surfaces. *J. Phys. Chem. A* **2021**, *125* (28), 6042-6058. DOI: 10.1021/acs.jpca.0c11284.
- (46) Nishihara, H.; Fujimoto, H.; Itoi, H.; Nomura, K.; Tanaka, H.; Miyahara, M. T.; Bonnaud, P. A.; Miura, T.; Zuzuki, A.; Miyamoto, N.; et al. Graphene-based ordered framework with a diverse range of carbon polygons formed in zeolite nanochannels. *Carbon* **2018**, *129*, 854-862. DOI: 10.1016/j.carbon.2017.12.055.
- (47) Hill, T. L. *An Introduction to Statistical Thermodynamics*; Addison-Wesley, 1960.
- (48) Lemmon, E.; Huber, M.; McLinden, M. *NIST Standard Reference Database 23: Reference Fluid Thermodynamic and Transport Properties-REFPROP, Version 9.1*; National Institute of Standards and Technology, 2013. <https://www.nist.gov/publications/nist-standard-reference-database-23-reference-fluid-thermodynamic-and-transport>.

CHAPTER SIX

CONCLUSIONS

Summary of Discoveries

This dissertation investigates the thermodynamics of the Langmuir adsorption model and the fundamental mechanisms of methane binding on carbonaceous adsorbent materials. The motivation of these studies was to evaluate the limitations of the Langmuir model as a way to deduce physical depictions of the adsorbed phase and quantify the adsorption energy of systems of relevance for energy storage applications. Adsorption has been studied for centuries but there are only a few studies that report on attempting to understand the atomistic picture of an adsorbate molecule physisorbed onto a two-dimensional surface through the modeling alone. This work sheds light on why it is such a difficult task, and what can and cannot be delivered by careful adsorption modeling of experimentally measured adsorption equilibria.

In the first study, we explored hydrogen adsorption on BFF-1, a material that is an ideal single-site adsorbent similar to that envisioned in Langmuir's original model. The goal of this work was to elucidate the temperature dependence of the Langmuir constant directly from the experimental adsorption data. In the second study, we tested the limitations of the Langmuir model to accurately detect binding site energies in a system with detailed, previously established properties: methane adsorption on four distinct site types on MOF-5. Building on the findings of the initial investigations, we discovered the methane adsorption mechanisms and corresponding thermodynamic properties on a series of model porous carbon materials with complex energy landscapes.

Three objectives of this dissertation were presented in Chapter One. In the following discussion, we will critically evaluate the outcomes of these objectives and the resulting discoveries that have led to a new perspective of adsorption modeling, thermodynamics, and guiding principles for methane storage materials design.

Objective 1:

“determine the temperature dependence of the Langmuir constant of the single-site Langmuir model and its effects on the isosteric enthalpy of adsorption.”

Using a systematic approach, we successfully fit an extensive set of hydrogen adsorption equilibria spanning four temperatures to a series of single-site Langmuir models with only 3 loose parameters. In principle, this should have led to one variant of the temperature dependence of the Langmuir constant (and its corresponding variant of the isosteric heat of adsorption) to be revealed as the best fitting. Our first discovery in this work was that the data were able to be fit equally well to any of the variants of the Langmuir model (spanning 6 different treatments of the atomistic picture of the adsorption site). This was very surprising; unfortunately, it was not very helpful for guiding future work in an unambiguous way. Interestingly, the effects of these different variants on the subsequent temperature dependence of the isosteric heat was large, but this too meant that no guidance was provided by our modeling efforts in this property of the adsorption system. Fortunately, one robust guiding principle did emerge: the average temperature isosteric heat of adsorption is almost identical for all methods employed and is hence a model-independent result.

While several of the above discoveries are negative results, they will be meaningful in the adsorption research community. Historically, there have been few reports aiming to develop an analytic, temperature-dependent theory of adsorption and to show how such decisions/models

influence the resulting thermodynamics. Researchers most often pick an adsorption model that adequately fits their adsorption data with little explanation as to how the model is physically suitable to describe the adsorption system. We recommend that researchers be aware of the physical implications of each adsorption model and the biases inherent to the resulting determined properties. While no specific model is found to be better suited in the case explored herein, reporting the average temperature isosteric heat of adsorption instead of the binding energy is one way to alleviate those biases.

In carrying out this work, we also formalized our own understanding of a systematic series of atomistic-level representations of the adsorption system and correlated each depiction to outcomes of the thermodynamic properties. We now better understand that when a free gas molecule interacts with an adsorbent surface, it has the potential to lose or gain degrees of freedom, resulting in the wide variety of temperature dependencies of the single-site Langmuir model. These models are derived using a first-principles statistical mechanic approach and the partition function is constructed based on an individualized treatment of the degrees of freedom (delta function, square potential, or quadratic potential) in each spatial dimension. These models link the pre-exponential factor in the Langmuir “constant” to simple properties of the adsorption site (e.g., site size or harmonic oscillator frequency). This was never formalized in past work and new meaning will be deduced from in-depth studies of these parameters in future work.

Objective 2:

“use the Langmuir model to accurately predict the number of binding site types and corresponding binding energies of a crystalline multi-site material.”

The findings from the study of hydrogen on BFF-1 were then implemented to test the capability of the Langmuir model to resolve the details of a more complex, multi-site adsorption

system. Methane adsorption on MOF-5 is a well-studied adsorption system, both experimentally¹ and computationally², and we aimed to corroborate these findings by measuring and modeling an extensive set of methane adsorption equilibria. We first focused on modeling a set of supercritical adsorption isotherms since the thermodynamic properties at room temperature are most important for applications. Unfortunately, in this study we found that Langmuir modeling (even when constrained with increasingly more “ground truth” information about the system) is effectively unable to accurately determine the binding site energies of methane on MOF-5 using the supercritical adsorption equilibria alone.

Despite the failure to achieve our original objective, two discoveries were made. The first was that by measuring a set of carefully chosen subcritical adsorption equilibria, physical properties of the adsorbent such as the total number of adsorption sites were possible to be effectively modeled, reducing the number of loose parameters in the supercritical adsorption fitting. Secondly, even though the model was unable to accurately capture the binding site energies, the average temperature isosteric heat of adsorption was again revealed to be consistent across all models, affirming our first study that this well-known property is in fact a measurable materials property and is independent of the adsorption model used.

Objective 3:

“use the insights gained above to provide guidelines for methane adsorption on various porous carbons (a system of high interest for practical energy storage applications) with a complex landscape of binding environments.”

Toward this objective, we measured supercritical methane adsorption equilibria on five different model porous carbons and evaluated the thermodynamics of each system by resting mainly on the isosteric heat determined at near the average temperature of the study: 298 K. In

previous work,³ an increasing isosteric heat of adsorption was detected on zeolite-templated carbon but the cause of this was not well understood. It was clear that surface homogeneity and methane-methane interactions were needed to achieve an increasing isosteric heat, but the role of confinement within the pores was not known. It was determined by comparison of ZTC to a material with high homogeneity but no confinement that confinement indeed plays an important role in achieving an increasing isosteric heat of adsorption.

In addition to that discovery, the different binding environments available to methane on porous carbon surfaces were atomistically investigated using computational guidance (and through collaboration with Prof. Robert Szilagyi). From the experimental and computational results, it is now clear that three-ring binding environments are crucial to the design of porous carbons for methane storage. Furthermore, developing new carbon materials with both three-ring or larger binding sites and pore sizes centered around ~ 7 Å and ~ 10.5 Å could lead to an even larger increase in isosteric heat of adsorption, and possibly higher capacities (in the larger pore case).

Future Work

Through this scientific exploration, we have uncovered new approaches and insights to adsorption modeling and derived guiding principles for the design of materials with high performance methane binding environments. But like any good adventure, the ending leaves us with more questions and a deeper desire to pursue new avenues of research. Some new suggested avenues will be highlighted in the following sections.

Interactions/Cooperativity in the Langmuir Model

The Langmuir adsorption model is rooted in a simple picture of adsorption that can describe the macroscopic properties of many adsorption systems, but will never provide a universal physical depiction of real-world systems. Several modifications to the modeling approach used herein can be implemented to obtain better quality depictions. The first is using fugacity instead of pressure as the independent variable in adsorption modeling. Fugacity accounts for the gas-gas interactions in the bulk fluid and changes the shape of the adsorption isotherm accordingly. We recommend that future researchers use fugacity more often, a modification that is already implemented in the current version of Realist³.

Secondly, the models used herein do not account for any interactions within the adsorbed phase. In our third study, we found that there are attractive interactions in the adsorbed phase on ZTC but continued to use a simple model of adsorption that ignored true cooperativity. We suggest addressing this issue in future work and developing a new Langmuir adsorption model that accounts for and quantifies these cooperative interactions. Lastly, accounting for adsorbent flexibility is a key need for future modeling efforts of methane and other modestly interacting gases on the surface of soft microporous materials.

Error Analysis of the Fitting Parameters

The adsorption literature is filled with adsorption modeling and the resulting fitting parameters, but adsorption scientists rarely report or investigate the intrinsic error from the fitting models on these fitting parameters. All fitting methods have some errors associated with the parameters and scientists should be able to report these. Scientists are aware of this and are therefore hesitant to report modeled parameters as a hard truth, but a better understanding of the

errors assists in quantifying the amount of confidence a model can provide. The isosteric heat of adsorption, for example, is generally taken to have an error of at least $\sim \pm 1$ kJ mol⁻¹, a level of precision that is supported by calorimetry and computational results as well. Future modifications of the fitting package used herein (REALIST³) should report these errors to bolster their subsequent analysis.

Schwartzite as a Methane Storage Material

Based on the experimental and computational results from the third study, the optimal methane storage material would have both confinement effects within its pores and a homogeneous binding surface comprising three-ring binding sites. Schwartzite are a class of carbon-based porous materials characterized by a negatively curved geometry with no edges (and hence exclusively three-ring type binding sites). Future work to prepare a schwartzite with ~ 10.5 Å pores should be undertaken for methane storage applications. Unfortunately, such materials are still only theoretical and have not been synthesized yet. The most promising synthetic route at the moment is to use a minimal surface scaffold and template it using an atomistically thin layer of carbon.⁴ Computational studies of methane storage in schwartzite should also be performed to guide the experimental work.

References

- (1) Hui, W.; Zhou W.; Yildirim T. Methane Sorption in Nanoporous Metal-Organic Frameworks and First Order Phase Transition of Confined Methane. *J. Phys. Chem. C* **2009**, *113* (7), 3029-3035. DOI: 10.1021/jp8103276.
- (2) Tsivion E.; Head-Gordon M. Methane Storage: Molecular Mechanisms Underlying Room-Temperature Adsorption in Zn₄O(BDC)₃ (MOF-5). *J. Phys. Chem. C* **2017**, *121* (22), 12091-12100. DOI: 10.1021/acs.jpcc.7b04246.

- (3) Quine, C. M. REal Adsorption Langmuir Isotherms for Sorption Theory: REALIST. *Github*. <https://github.com/cullenmq/REALIST> (accessed 2025-03-30).
- (4) Taylor, E. E.; Garman, K.; Stadie, N. P. Atomistic Structures of Zeolite-Templated Carbon. *Chem. Mater.* **2020**, 32 (7), 2742-2752. DOI: 10.1021/acs.chemmater.0c00535.

REFERENCES CITED

- Quine, C. M. REal Adsorption Langmuir Isotherms for Sorption Theory: REALIST. *Github*. <https://github.com/cullenmq/REALIST> (accessed 2025-03-30).
- Tollefson, J. IPCC Climate Report: Earth Is Warmer Than It's Been in 125,000 Years. *Nature* **2021**, 596 (7871), 171–172.
- Our World in Data. *Energy consumption by source, World*, 2024. <https://ourworldindata.org/grapher/energy-consumption-by-source-and-country> (accessed 2025-03-01).
- Our World in Data. *Cars, planes, trains: where do CO2 emissions from transport come from?*, 2020 <https://ourworldindata.org/co2-emissions-from-transport> (accessed 2025-03-01).
- IPCC wraps up its most in-depth assessment of climate change. CarbonBrief 2023. <https://www.carbonbrief.org/qa-ipcc-wraps-up-its-most-in-depth-assessment-of-climate-change/> (accessed 2025-03-01).
- Demirbas, A. Effects of Moisture and Hydrogen Content on the Heating Value of Fuels. *Energy Sources, Part A* **2007**, 29 (7), 649-655. DOI: 10.1080/009083190957801.
- NIST Chemistry WebBook; National Institute of Standards and Technology. <https://webbook.nist.gov/chemistry/> (accessed 04/19/25).
- Xie, Z.; Jin, Q.; Su, G.; Lu, W. A Review of Hydrogen Storage and Transportation: Progresses and Challenges. *Energies* **2024**, 17 (16), 4070. DOI: 10.3390/en17164070.
- Doosan Mobility. *Hydrogen Tank*. <https://www.doosanmobility.com/en/products/hydrogen-tank> (accessed 2024-11-18).
- Hydrogen decarbonization pathways A life-cycle assessment*; Hydrogen Council, 2021. https://hydrogencouncil.com/wp-content/uploads/2021/01/Hydrogen-Council-Report_Decarbonization-Pathways_Part-1-Lifecycle-Assessment.pdf.
- Lemmon, E.; Huber, M.; McLinden, M. *NIST Standard Reference Database 23: Reference Fluid Thermodynamic and Transport Properties-REFPROP, Version 9.1*; National Institute of Standards and Technology, 2013. <https://www.nist.gov/publications/nist-standard-reference-database-23-reference-fluid-thermodynamic-and-transport>.
- Stadie, N. P. Synthesis and Thermodynamic Studies of Physisorptive Energy Storage Materials. Ph.D. Dissertation, California Institute of Technology, Pasadena CA, 2013. <http://thesis.library.caltech.edu/7198/>.

Mayyas, A.; Wei, M.; Levis, G. Hydrogen as a long-term, large-scale energy storage solution when coupled with renewable energy sources or grids with dynamic electricity pricing schemes. *Int. J. Hydrogen Energy* **2020**, *45* (33), 16311-16325. DOI: 10.1016/j.ijhydene.2020.04.163.

Rusman, N.A.A.; Dahari, M. A review on the current progress of metal hydrides material for solid-state hydrogen storage applications. *Int. J. Hydrogen Energy* **2016**, *41* (28), 12108-12126. DOI: 10.1016/j.ijhydene.2016.05.244.

Panella, B.; Hirscher, M.; Roth, S. Hydrogen adsorption in different carbon nanostructures. *Carbon* **2005**, *43* (10), 2209-2214. DOI: 10.1016/j.carbon.2005.03.037.

Klontzas, E.; Tylanakis, E.; Froudakis, G. E. Designing 3D COFs with Enhanced Hydrogen Storage Capacity. *Nano Lett.* **2010**, *10* (2), 452-454. DOI:10.1021/nl903068a.

Ahmed, A.; Liu, Y.; Purewal, J.; Tran, L. D.; Wong-Foy, A. G.; Veenstra, M.; Matzger, A. J.; Siegel, D. J. Balancing gravimetric and volumetric hydrogen density in MOFs. *Energy Environ. Sci.* **2017**, *11*, 2459-2471. DOI: 10.1039/C7EE02477K.

Ahmed, A.; Seth, S.; Purewal, J.; Wong-Foy, A. G.; Veenstra, M.; Matzger, A. J.; Siegel, D. J. Exceptional hydrogen storage achieved by screening nearly half a million metal-organic frameworks. *Nat. Commun.* **2019**, *10*, 1568. DOI: 10.1038/s41467-019-09365-w.

Kapelewski, M. T.; Runcevski, T.; Tarver, J. D.; Jiang, H. Z. H.; Hurst, K. E.; Parilla, P. A.; Ayala, A.; Gennett, T.; FitzGerald, S. A.; Brown, C. M.; et al. Record Hydrogen Storage Capacity in the Metal-Organic Framework Ni₂(m-dobdc) at Near-Ambient Temperatures. *Chem. Mater.* **2018**, *30* (22), 8179-8189. DOI: 10.1021/acs.chemmater.8b03276.

Peng, Y.; Krungleviciute, V.; Eryazici, I.; Hupp, J. T.; Farha, O. K.; Yildirim, T. Methane Storage in Metal-Organic Frameworks: Current Records, Surprise Findings, and Challenges. *J. Am. Chem. Soc.* **2013**, *135* (32), 11887-11894. DOI: 10.1021/ja4045289.

Tian, T.; Zeng, Z.; Vulpe, D.; Casco, M. E.; Divitini, G.; Midgley, P. A.; Silvestre-Albero, J.; Tan, J.-C.; Moghadam, P. Z.; Fairen-Jimenez, D. A sol-gel monolithic metal-organic framework with enhanced methane uptake. *Nature Mater.* **2018**, *17*, 174-179. DOI: 10.1038/nmat5050.

Barghi, S. H.; Tsotsis, T. T.; Sahimi, M. Chemisorption, physisorption and hysteresis during hydrogen storage in carbon nanotubes. *Int. J. Hydrogen Energy* **2014**, *39*, 1390-1397. DOI: 10.1016/j.ijhydene.2013.10.163.

Dabrowski, A. Adsorption – from theory to practice. *Adv. Colloid Interface Sci* **2001**, *93*, 135-224. DOI: 10.1016/S0001-8686(00)00082-8.

Alberti, L. B. *L'architettura*; Padua, Firenze, Italy, 1483/1485.

Langmuir, I. The Constitution and Fundamental Properties of Solids and Liquids. Part I. Solids. *J. Am. Chem. Soc.* **1916**, *38* (11), 2221–2295. DOI: 10.1021/ja02268a002.

Langmuir, I. The Constitution and Fundamental Properties of Solids and Liquids. Part II. Liquids. *J. Am. Chem. Soc.* **1917**, 39 (9), 1848-1906. DOI: 10.1021/ja02254a006.

Langmuir, I. The Adsorption of Gases on Plane Surfaces of Glass, Mica and Platinum. *J. Am. Chem. Soc.* **1918**, 40 (9), 1361–1403. DOI: 10.1021/ja02242a004.

Swenson, H.; Stadie, N. P. Langmuir's Theory of Adsorption: A Centennial Review. *Langmuir* **2019**, 35 (16), 5409-5426. DOI: 10.1021/acs.langmuir.9b00154.

Callen, H. B. *Thermodynamics and Introduction to Thermostatistics*, Second ed; John Wiley & Sons: New York, NY, 1985.

Quine, C. M. Tunability of Gas Adsorption Enthalpies in Carbonaceous Materials for Energy-Related Applications, Ph.D. Dissertation, California Institute of Technology, 2023. <https://thesis.library.caltech.edu/15222/>.

Freundlich, H. *Kapillarchemie: eine Darstellung der Chemie der Kolloide und verwandter Gebiete*; Akademische Verlagsgesellschaft, 1909.

Do, D. D. *Adsorption Analysis: Equilibria and Kinetics*, Imperial College Press, 1998.

Tzabar, N.; ter Brake, H. J. M. Adsorption isotherms and Sips models of nitrogen, methane, ethane, and propane on commercial activated carbons and polyvinylidene chloride. *Adsorption* **2016**, 22, 901-914. DOI: 10.1007/s1045-0169794-9.

Hill, A. V. The possible Effects of the Aggregation of the Molecules of Haemoglobin on Its Dissociation Curves. *J. Physiol.* **1910**, 40, 4-7.

Zhu, Z.; Parker, S. T.; Forse, A. C.; Lee, JH.; Siegelman, R. L.; Milner, P. J.; Tsai, H.; Ye, M.; Xiong, S.; Paley, M. V., et. al. Cooperative Carbon Dioxide Capture in Diamine-Appended Magnesium-Olsalazine Frameworks. *J. Am. Chem. Soc.* **2023**, 145 (31), 17151-17163. DOI: 10.1021/jacs.3c03870.

Gesztelyi, R.; Zsuga, J.; Kemeny-Beke, A.; Varga, B.; Juhasz, B.; Tosaki, A. The Hill equation and the origin of quantitative pharmacology. *Arch. Hist. Exact Sci.* **2012**, 66, 427-438. DOI: 10.1007/s00407-012-0098-5.

Josiah Willard Gibbs. On the equilibrium of heterogeneous substances. *Am. J. Sci. Arts* **1878**, s3-16 (96), 441-458. DOI: 10.2475/ajs.s3-16.96.441.

Parilla, P. A.; Gross, K.; Hurst, K.; Gennett, T. Recommended volumetric capacity definitions and protocols for accurate standardized and unambiguous metrics for hydrogen storage materials. *Appl. Phys. A* **2016**, 122, 201. DOI: 10.1007/s00339-016-9654-1.

Stadie, N. P. Synthesis and Thermodynamic Studies of Physisorptive Energy Storage Materials. Ph. D. Dissertation, California Institute of Technology, Pasadena, CA, 2012. <https://thesis.library.caltech.edu/7198/>.

Bell, I. H.; Wronski, J.; Quoilin, J.; Lemort, V. Pure and Pseudo-pure Fluid Thermophysical Property Evaluation and the Open-Source Thermophysical Property Library CoolProp. *Ind. Eng. Chem. Res.* **2014**, 53 (6), 2498-2508. DOI: 10.1021/ie4033999.

Lemmon, E.; Huber, M.; McLinden, M. *NIST Standard Reference Database 23: Reference Fluid Thermodynamic and Transport Properties-REFPROP, Version 9.1*; National Institute of Standards and Technology, 2013. <https://www.nist.gov/publications/nist-standard-reference-database-23-reference-fluid-thermodynamic-and-transport>.

Brunauer, S.; Emmett, P. H.; Teller, E. Adsorption of Gases in Multimolecular Layers. *J. Am. Chem. Soc.* **1938**, 60 (2), 309-319. DOI: 10.1021/ja01269a023.

Rouquerol, J.; Llewellyn, P.; Rouquerol, F. Is the BET Equation Applicable to Microporous Adsorbents? *Studies in Surface Science and Catalysis*; Elsevier, 2007; Vol. 160, pp 49–56. [https://doi.org/10.1016/S0167-2991\(07\)80008-5](https://doi.org/10.1016/S0167-2991(07)80008-5)

Langmuir, I. The Constitution and Fundamental Properties of Solids and Liquids. Part I. Solids. *J. Am. Chem. Soc.* 1916, 38 (11), 2221–2295. <https://doi.org/10.1021/ja02268a002>

Langmuir, I. The Constitution and Fundamental Properties of Solids and Liquids. II. Liquids. *J. Am. Chem. Soc.* 1917, 39 (9), 1848-1906. <https://doi.org/10.1021/ja02254a006>

Langmuir, I. The Adsorption of Gases on Plane Surfaces of Glass, Mica and Platinum. *J. Am. Chem. Soc.* 1918, 40 (9), 1361–1403. <https://doi.org/10.1021/ja02242a004>

Brunauer, S.; Emmett, P. H.; Teller, E. Adsorption of Gases in Multimolecular Layers. *J. Am. Chem. Soc.* 1938, 60 (2), 309–319. <https://doi.org/10.1021/ja01269a023>

Swenson, H.; Stadie, N. P. Langmuir's Theory of Adsorption: A Centennial Review. *Langmuir* 2019, 35 (16), 5409–5426. <https://doi.org/10.1021/acs.langmuir.9b00154>

Hill, T. L. *An Introduction to Statistical Thermodynamics*; Addison-Wesley, 1960.

Stadie, N. P. Synthesis and Thermodynamic Studies of Physisorptive Energy Storage Materials, California Institute of Technology, 2012. <https://doi.org/10.7907/ZK3P-CV60>

Savara, A. Standard States for Adsorption on Solid Surfaces: 2D Gases, Surface Liquids, and Langmuir Adsorbates. *J. Phys. Chem. C* 2013, 117 (30), 15710–15715. <https://doi.org/10.1021/jp404398z>

Wang, Z. Temperature Dependence of Gas Physisorption Energy: Experimental and Computational Studies of Krypton on Porous Carbon, PhD thesis, California Institute of Technology, 2023. <https://thesis.library.caltech.edu/15181/>

Quine, C. M. Tunability of Gas Adsorption Enthalpies in Carbonaceous Materials for Energy-Related Applications, California Institute of Technology, 2023.
<https://thesis.library.caltech.edu/15222/>

Gibbs, J. W. On the Equilibrium of Heterogeneous Substances. *Trans. Conn. Acad.* 1876, III, 108–248 and 343–524.

Callen, H. Thermodynamics and an Introduction to Thermostatistics, Second.; John Wiley & Sons, 1985.

Stylianou, K. C.; Warren, J. E.; Chong S. Y.; Rabone, J.; Bacsá, J.; Bradshaw, D.; Rosseinsky, M. J. CO₂ selectivity of a 1D microporous adenine-based metal-organic framework synthesized in water. *Chem. Commun.*, 2011, 47, 3389–3392. <https://doi.org/10.1039/c0cc05559j>

Rouquerol, J.; Llewellyn, P.; Rouquerol, F. Is the BET Equation Applicable to Microporous Adsorbents? *Studies in Surface Science and Catalysis*; Elsevier, 2007; Vol. 160, pp 49–56.
[https://doi.org/10.1016/S0167-2991\(07\)80008-5](https://doi.org/10.1016/S0167-2991(07)80008-5)

Banerjee, D., Simon, C., Plonka, A. *et al.* Metal-organic framework with optimally selective xenon adsorption and separation. *Nat. Commun.* **7**, ncomms11831 (2016).
<https://doi.org/10.1038/ncomms11831>

Will, F. G. Hydrogen Adsorption on Platinum Single Crystal Electrodes. *J. Electrochem. Soc.* 1965, 112 (4), 451. <https://doi.org/10.1149/1.2423567>

Chiu, N. C.; Compton, D.; Gładysiak, A.; Simrod, S.; Khivantsev, K.; Woo, T. K.; Stadie, N. P.; Stylianou, K. C. Hydrogen Adsorption in Ultramicroporous Metal–Organic Frameworks Featuring Silent Open Metal Sites. *ACS Appl. Mater. Interfaces* 2023, acsami.3c12139.
<https://doi.org/10.1021/acsami.3c12139>

Quine, C. M. REal Adsorption Langmuir Isotherms for Sorption Theory: REALIST. *Github*.
<https://github.com/cullenmq/REALIST> (accessed 2025-03-30).

R. Rowsey, E. E. Taylor, R. W. Hinson, D. Compton, N. P. Stadie, R. K. Szilagyi, Does Boron or Nitrogen Substitution Affect Hydrogen Physisorption on Open Carbon Surfaces? *Phys. Chem. Chem. Phys.*, 24, 28121–28126 (2022)

Mertens, F. O. Determination of Absolute Adsorption in Highly Ordered Porous Media. *Surf. Sci.* 2009, 603 (10–12), 1979–1984. <https://doi.org/10.1016/j.susc.2008.10.054>

Stadie, N. P.; Murialdo, M.; Ahn, C. C.; Fultz, B. Anomalous Isosteric Enthalpy of Adsorption of Methane on Zeolite-Templated Carbon. *J. Am. Chem. Soc.* 2013, 135 (3), 990–993.
<https://doi.org/10.1021/ja311415m>

Stylianou, K. C.; Warren, J. E.; Chong S. Y.; Rabone, J.; Bacsá, J.; Bradshaw, D.; Rosseinsky, M. J. “CO₂ Selectivity of a 1D Microporous Adenine-Based Metal-Organic Framework Synthesized in Water.” *Chem. Commun.*, 2011, 47, 3389–3392. <https://doi.org/10.1039/c0cc05559j>

Wang, Z. “Temperature Dependence of Gas Physisorption Energy: Experimental and Computational Studies of Krypton on Porous Carbon.” PhD thesis, California Institute of Technology, 2023. <https://thesis.library.caltech.edu/15181/> (see section 2.4, “Surface Dynamics”)

Langmuir, I. The Constitution and Fundamental Properties of Solids and Liquids. Part I. Solids. *J. Am. Chem. Soc.* **1916**, 38 (11), 2221–2295. DOI: 10.1021/ja02268a002.

Langmuir, I. The Constitution and Fundamental Properties of Solids and Liquids. Part II. Liquids. *J. Chem. Soc.* **1917**, 184 (5), 721. DOI: 10.1021/ja02254a006.

Langmuir, I. The Adsorption of Gases on Plane Surfaces of Glass, Mica and Platinum. *J. Am. Chem. Soc.* **1918**, 40 (9), 1361–1403. DOI: 10.1021/ja02242a004.

Swenson, H. Stadie, N. P. Langmuir’s Theory of Adsorption: A Centennial Review. *Langmuir* **2019**, 35 (16), 5409–5426. DOI: 10.1021/acs.langmuir.9b00154.

Brunauer, S.; Emmett, P. H.; Teller, E. Adsorption of Gases in Multimolecular Layers. *J. Am. Chem. Soc.* **1938**, 60 (2), 309–319. DOI: 10.1021/ja01269a023.

Compton, D.; Chui, N. C.; Stylianou, K. C.; Stadie, N. P. The Temperature Dependence of the Langmuir Adsorption Model in a Single Site Metal-Organic Framework. *Langmuir* **2025**, accepted.

Purewal, J.; Liu, D.; Sudik, A.; Veenstra, M.; Yang, J.; Maurer, S.; Müller, U.; Siegel, D. J. Improved Hydrogen Storage and Thermal Conductivity in High Density MOF-5 Composites. *J. Phys. Chem. C* **2012**, 116 (38), 20199–20212. DOI: 10.1021/jp305524f.

Stadie, N. P. Synthesis and Thermodynamic Studies of Physisorptive Energy Storage Materials. Ph. D. Dissertation, California Institute of Technology, Pasadena, CA, 2012. <https://thesis.library.caltech.edu/7198/>.

Stadie, N. P.; Murialdo, M.; Ahn, C. C.; Fultz, B. Anomalous Isosteric Enthalpy of Adsorption of Methane on Zeolite-Templated Carbon. *J. Am. Chem. Soc.* **2013**, 135 (3), 990–993. DOI: 10.1021/ja311415m.

Stadie, N. P.; Murialdo, M.; Ahn, C. C.; Fultz, B. Unusual Entropy of Adsorbed Methane on Zeolite-Templated Carbon. *J. Phys. Chem. C* **2015**, 119 (47), 26409–26421. DOI: 10.1021/acs.jpcc.5b05021.

Quine, C. M.; Taylor, E. E.; Compton, D.; Gabe, A.; Nishihara, H.; Strange, N. A.; Ahn, C. C.; Fultz, B. T.; Stadie, N. P. Record Methane Storage and Delivery from Ultrasoft Ordered Microporous Carbon Monoliths with Tunable Porosity. **2025**.

Farha, O. K.; Hupp, J. T. Rational Design, Synthesis, Purification, and Activation of Metal-Organic Framework Materials. *Acc. Chem. Res.* **2010**, 43 (8), 1166–1175.

Eddaoudi, M.; Kim, J.; Rosi, N.; Vodak, D.; Wachter, J.; O’Keeffe, M.; Yaghi, O. M. Systematic Design of Pore Size and Functionality in Isoreticular MOFs and Their Application in Methane Storage. *Science* **2002**, *295* (5554), 469–472. DOI: 10.1126/science.1067208.

Casco, M. E.; Martinez-Escandell, M.; Gadea-Ramos, E.; Kaneko, K.; Silvestre-Albero, J.; Rodriguez-Reinoso, F. High-Pressure Methane Storage in Porous Materials: Are Carbon Materials in the Pole Position? *Chem. Mat* **2015**, *27* (3), 959–964. DOI: 10.1021/cm5042524.

Tian, T.; Zeng, Z.; Vulpe, D.; Casco, M. E.; Divitini, G.; Midgley, P. A.; Silvestre-Albero, J.; Tan, J.C.; Moghadam, P. Z.; et. al. A sol-gel monolithic metal-organic framework with enhanced methane uptake. *Nat. Mater* **2018**, *17* (2), 174–179. DOI: 10.1038/nmat5050.

Peng, Y.; Krungleviciute, V.; Eryazici, I.; Hupp, J. T.; Farha, O. K.; Yildirim, T. Methane Storage in Metal-Organic Frameworks: Current Records, Surprise Findings, and Challenges. *J. Am. Chem. Soc.* **2013**, *135* (32), 11887–11894. DOI: 10.1021/ja4045289.

Connolly, B. M.; Madden, D. G.; Wheatley, A. E. H.; Fairen-Jimenez, D. Shaping the Future of Fuel: Monolithic Metal-Organic Frameworks for High-Density Gas Storage. *J. Am. Chem. Soc.* **2020**, *142* (19), 8541–8549. DOI: 10.1021/jacs.0c00270.

Hui, W.; Zhou W.; Yildirim T. Methane Sorption in Nanoporous Metal-Organic Frameworks and First Order Phase Transition of Confined Methane. *J. Phys. Chem. C* **2009**, *113* (7), 3029–3035. DOI: 10.1021/jp8103276.

Tsivion E.; Head-Gordon M. Methane Storage: Molecular Mechanisms Underlying Room-Temperature Adsorption in $\text{Zn}_4\text{O}(\text{BDC})_3$ (MOF-5). *J. Phys. Chem. C* **2017**, *121* (22), 12091–12100. DOI: 10.1021/acs.jpcc.7b04246.

Li, H.; Eddaoudi, M.; O’Keeffe, M.; Yaghi, O. M. Design and synthesis of an exceptionally stable and highly porous metal-organic framework. *Nature* **1999**, *402*, 276–279. DOI: 10.1038/46248.

Wang, Z. Temperature Dependence of Gas Physisorption Energy: Experimental and Computational Studies of Krypton on Porous Carbon. Ph. D. Thesis, California Institute of Technology, Pasadena, CA, 2023. <https://thesis.library.caltech.edu/15222/>.

Gibbs, J. W. On the Equilibrium of Heterogeneous Substances. *Trans. Conn. Acad.* 1876, III, 108–248 and 343–524.

Lemmon, E.; Huber, M.; McLinden, M. *NIST Standard Reference Database 23: Reference Fluid Thermodynamic and Transport Properties-REFPROP, Version 9.1*; National Institute of Standards and Technology, 2013. <https://www.nist.gov/publications/nist-standard-reference-database-23-reference-fluid-thermodynamic-and-transport>.

Parilla, P. A.; Gross, K.; Hurst, K.; Gennett, T. Recommended volumetric capacity definitions and protocols for accurate standardized and unambiguous metrics for hydrogen storage materials. *Appl. Phys. A* **2016**, *122*, 201. DOI: 10.1007/s00339-016-9654-1.

Rouquerol, J.; Llewellyn, P.; Rouquerol, F. Is the Bet Equation Applicable to Microporous Adsorbents? *Studies in Surface Science and Catalysis*; Elsevier 2007; Vol. 160, pp 49–56. DOI: 10.1016/S0167-2991(07)80008-5.

Bowman Jr., R. C. ; Luo C. H.; Ahn, C. H.; Witham, C. K.; Fultz, B. T. The effect of tin on the degradation of $\text{LaNi}_{5-y}\text{Sn}_y$ metal hydrides during thermal cycling. *J. Alloys Compd.* **1995**, *217* (2), 185-192. DOI: 10.1016/0925-8388(94)01337-3.

Quine, C. M. REal Adsorption Langmuir Isotherms for Sorption Theory: REALIST. *Github*. <https://github.com/cullenmq/REALIST> (accessed 2025-03-30).

Willems, T. F.; Rycroft, C. H.; Kazi, M.; Meza, J. C.; Haranczyk, M. Algorithms and tools for high-throughput geometry-based analysis of crystalline porous materials. *Microporous Mesoporous Mat.* **2012**, *149* (1), 134-141, DOI: 10.1016/j.micromeso.2011.08.020.

Wu, H.; Simmons, J. M.; Liu, Y.; Brown, C. M.; Wang X.; Ma, S.; Peterson, V. K.; Southon, P. D.; Kepert, C. J.; Zhou, H.; et. al. Metal-Organic Frameworks with Exceptionally High Methan Uptake: Where and How is Methane Stored? *Chem. Eur. J.* **2010**, *16* (17), 5205-5214. DOI: 10.1002/chem.200902719.

He, Y.; Zhou, W.; Qian, G.; Chen, B. Methane storage in metal-organic frameworks. *Chem. Soc. Rev.* **2014**, *43* (16), 5657-5678. DOI: 10.1039/C4CS00032C.

Chakraborty, A.; Saha, B. B.; Koyama, S.; Ng, K. C. On the Thermodynamic modeling of the isosteric heat of adsorption and comparison with experiments. *Appl. Phys. Lett.* **2006**, *89*, 171901. DOI: 10.1063/1.2360925

Cao, D. V. ; Sircar, S. Temperature Dependence of the Isosteric Heat of Adsorption. *Adsorption Science & Technology* **2001**, *19* (10), 887-894. DOI: 10.1260/0263617011494646

Al-Muhtaseb, S. A.; Ritter, J. A. A Statistical Mechanical Perspective on the Temperature Dependence of the Isosteric Heat of Adsorption and Adsorbed Phase Heat Capacity. *J. Phys. Chem. B* **1999**, *103* (38), 8104-8115. DOI: 10.1021/jp990556c

Faramawy, S.; Zaki, T.; Sakr, A. A-E. Natural gas Origin, composition, and processing: A review. *J. Nat. Gas Sci. Eng.* **2016**, *34*, 34-54. DOI: 10.1016/j.jngse.2016.06.030.

Kakaee, A-H.; Paykani, A.; Ghajar, M. The influence of fuel composition on the combustion and emission characteristics of natural gas fueled engines. *Renewable Sustainable Energy Rev.* **2014**, *38*, 64-78. DOI: 10.1016/j.rser.2014.05.080.

Monthly Energy Review March 2025; U.S. Energy Information Administration, 2025.

Casco, M. E.; Martinez-Escandell, M.; Gadea-Ramos, E.; Kaneko, K.; Silvestre-Albero, J.; Rodriguez-Reinoso, F. High-Pressure Methane Storage in Porous Materials: Are Carbon Materials in the Pole Position. *Chem. Mater.* **2015**, *27* (3), 959-964. DOI: 10.1021/cm5042524.

MOVE Methane Opportunities for Vehicular Energy; U.S. Department of Energy. <https://arpa-e.energy.gov/programs-and-initiatives/view-all-programs/move> (accessed 04/14/2025).

Memetova, A.; Tyagi, I.; Karri, R. R.; Kumar, V.; Tyagi, K.; Suhas; Memetov, N.; Zelenin, A.; Pasko, T.; Gerasimova, A; et. al. Porous carbon-based material as a sustainable alternative for the storage of natural gas (methane) and biogas (biomethane): A review. *Chem. Eng. J.* **2022**, *446* (4), 137373. DOI: 10.1016/j.cej.2022.137373.

Nishihara, H.,; Kyotani, T. Templated Nanocarbons for Energy Storage. *Adv. Mater.* **2012**, *24* (33), 4473-4498. DOI: 10.1002/adma.201201715.

Waller, P. J.; Gandara, F.; Yaghi, O. M. Chemistry of Covalent Organic Frameworks. *Acc. Chem. Res.* **2015**, *48* (12), 3053-3063. DOI: 10.1021/acs.accounts.5b00369.

Tian, Y.; Zhu, G. Porous Aromatic Frameworks (PAFs). *Chem. Rev.* **2020**, *120* (16), DOI: 10.1021/acs.chemrev.9b00687.

Nishihara, H.; Hirota, T.; Matsuura, K.; Ohwada, M.; Hoshino, N.; Akutagawa, T.; Higuchi, T.; Jinnai, H.; Koseki, Y.; Kasai, H.; et al. Synthesis of ordered carbonaceous frameworks from organic crystals. *Nat. Commun.* **2017**, *8*, 109. DOI: 10.1038/s41467-017-00152-z.

Cracknell, R. F.; Gordon, P.; Gubbins, K. E. Influence of Pore Geometry on the Design of Microporous Materials for Methane Storage. *J. Phys. Chem.* **1993**, *97* (2), 494-499. DOI: 10.1021/j100104a036.

Nishihara, H.; Kyotani, T. Zeolite-templated carbons – three-dimensional microporous graphene frameworks. *Chem. Commun.* **2018**, *54* (45), 5648-5673. DOI: 10.1039/c8cc01932k.

Ben, T.; Ren, H.; Ma, S.; Cao, D.; Lan, J.; Jing, X.; Wang, W.; Xu, J. ;Deng, F.; Simmons, J. M.; et al. Targeted Synthesis of a Porous Aromatic Framework with High Stability and Exceptionally High Surface Area. *Angew. Chem. Int. Ed.* **2009**, *48* (50), 9457-9460. DOI: 10.1002/anie.200904637.

Stadie, N. P.; Murialdo, M.; Ahn, C. C.; Fultz, B. Anomalous Isosteric Enthalpy of Adsorption of Methane on Zeolite-Templated Carbon. *J. Am. Chem. Soc.* **2013**, *135* (3), 990-993. DOI: 10.1021/ja311415m.

Stadie, N. P.; Murialdo, M.; Ahn, C. C.; Fultz, B. Unusual Entropy of Adsorbed Methane on Zeolite-Templated Carbon. *J. Phys. Chem. C* **2015**, *119* (47), 26409-26421. DOI: 10.1021/acs.jpcc.5b05021.

Ducrot-Boisgontier, C.; Parmentier, J.; Faour, A.; Patarin, J.; Pirngruber, G. D. FAU-Type Zeolite Nanocasted Carbon Replicas for CO₂ Adsorption and Hydrogen Purification. *Energy Fuels* **2010**, *24*, 3595-3602. DOI: 10.1021/ef100011q.

Guan, C.; Su, F.; Zhao, X.S.; Wang. Methane storage in a template-synthesized carbon. *Sep. Purif. Technol.* **2008**, *64* (1), 124-126. DOI: 10.1016/j.seppur.2008.08.007.

Yong Liang Guana, C; Elkamel, A.; Wang, K. Energy Gas Storage in Template-Synthesized Carbons with Different Porous Structures. *Can. J. Chem. Eng.* **2015**, *93* (3), 527-531. DOI: 10.1002/cjce.22141.

Antoniou, M. K.; Diamanti, E. K.; Enotiadis, A.; Policichio, A.; Dimos, K.; Ciuchi, F.; Maccallini, E.; Gournis, D.; Agostino, R. G.; Methane storage in zeolite-like carbon materials. *Microporous Mesoporous Mater.* **2014**, *188*, 16-22. DOI: 10.1016/j.micromeso.2013.12.030.

Shi, J.; Li, W.; Li, D. Rapidly reversible adsorption of methane with a high storage capacity on the zeolite templated carbons with glucose as carbon precursors. *Colloids Surf. A* **2015**, *485*, 11-17. DOI: https://doi.org/10.1016/j.colsurfa.2015.08.026.

Stadie, N. P.; Fultz, F.; Ahn, C. C.; Murialdo, M. Nanostructured Carbon Materials for Adsorption of Methane and Other Gases. US9067848, 2015.

Pei, C., Ben, T., & Qiu, S. Great Prospects for PAF-1 and its derivatives. *Mater. Horiz.* **2015**, *2* (1), 11-21. DOI:10.1039/c4mh00163j.

Ben, T., Pei, C., Zhang, D., Xu, J., Deng, F., Jing, X., & Qiu, S. Gas storage in porous aromatic frameworks (PAFs). *Energy Environ. Sci.* **2011**, *4* (10), 3991. DOI:10.1039/c1ee01222c.

Farha, O. K.; Hupp, J. T. Rational Design, Synthesis, Purification, and Activation of Metal-Organic Framework Materials. *Acc. Chem. Res.* **2010**, *43* (8), 1166-1175. DOI:10.1021/ar1000617.

Li, H.; Eddaoudi, M.; O'Keeffe, M.; Yaghi, O. M. Design and synthesis of an exceptionally stable and highly porous metal-organic framework. *Nature* **1999**, *402*, 276-279. DOI: 10.1038/46248.

Ahmed, A.; Liu, Y.; Purewal, J.; Tran, L. D.; Wong-Foy, A. G.; Veenstra, M.; Matzger, A. J.; Siegel, D. J. Balancing gravimetric and volumetric hydrogen density in MOFs. *Energy Environ. Sci.* **2017**, *10*, 2459. DOI: 10.1039/c7ee02477k.

Samantaray, S. S.; Putnam, S. T.; Stadie, N. P. Volumetrics of Hydrogen Storage by Physical Adsorption. *Inorganics* **2021**, *9* (6), 45. DOI: 10.3390/inorganics9060045.

Hui, W.; Zhou W.; Yildirim T. Methane Sorption in Nanoporous Metal-Organic Frameworks and First Order Phase Transition of Confined Methane. *J. Phys. Chem. C* **2009**, *113* (7), 3029-3035. DOI: 10.1021/jp8103276.

- Tsivion E.; Head-Gordon M. Methane Storage: Molecular Mechanisms Underlying Room-Temperature Adsorption in $\text{Zn}_4\text{O}(\text{BDC})_3$ (MOF-5). *J. Phys. Chem. C* **2017**, *121* (22), 12091-12100. DOI: 10.1021/acs.jpcc.7b04246.
- Compton, D.; Chui, N. C.; Stylianou, K. C.; Stadie, N. P. The Temperature Dependence of the Langmuir Adsorption Model in a Single Site Metal-Organic Framework. *Langmuir* **2025**, ASAP Article. DOI: 10.1021/acs.langmuir.5c00757.
- Nishihara, H.; Hou, P. X.; Li, L. X.; Ito, M.; Uchiyama, M.; Kaburagi, T.; Ikura, A.; Katamura, J.; Kawarada, T.; Mizuuchi, K.; Kyotani, T. High-Pressure Hydrogen Storage in Zeolite-Templated Carbon. *J. Phys. Chem. C* **2009**, *113* (8), 3189-3196. DOI: 10.1021/jp808890x.
- Voskuilen, T. G.; Pourpoint, T. L.; Dailly, A. M. Hydrogen adsorption on microporous materials at ambient temperatures and pressures up to 50 MPa. *Adsorption* **2012**, *18*, DOI: 10.1007/s10450-012-9397-z.
- Stadie, N. P.; Purewal, J. J.; Ahn, C. C.; Fultz, B. Measurements of Hydrogen Spillover in Platinum Doped Superactivated Carbon. *Langmuir* **2010**, *26* (19), 15481-15485. DOI: 10.1021/la9046758.
- Stadie, N. P.; Vajo, J. J.; Cumberland, R. W.; Wilson, A. A.; Ahn, C. C.; Fultz, B. Zeolite-Templated Carbon Materials for High Pressure Hydrogen Storage. *Langmuir* **2012**, *28* (26), 10057-10063. DOI: 10.1021/la302050m.
- Burrell, J.; Bethea, D.; Troub, B. Combination volumetric and gravimetric sorption instrument for high accuracy measurements of methane adsorption. *Rev. Sci. Instrum.* **2017**, *88* (5), 053902. DOI: 10.1063/1.4982889.
- Choi, S.; Alkhabbaz, M. A.; Wang, Y.; Othman, R. M.; Choi, M. Unique thermal contraction of zeolite-templated carbons enabling micropore size tailoring and its effects on methane storage. *Carbon* **2019**, *141*, 143-153. DOI: 10.1016/j.carbon.2018.09.045.
- Beckner, M.; Dailly, A. Hydrogen and methane storage in adsorbent materials for automotive applications. *Int. J. Energy Res.* **2016**, *40*, 91-99. DOI: 10.1002/er.3324.
- Romanos, J.; Dargham, S. A.; Roukos, R.; Pfeifer, P. Properties of adsorbed supercritical methane film in nanopores. *AIP Advances* **2018**, *8* (12), 125011. DOI: 10.1063/1.5074086.
- Zhu, Q. L.; Tsumori, N.; Xu, Q. Sodium hydroxide-assisted growth of uniform Pd nanoparticles on nanoporous carbon MSC-30 for efficient and complete dehydrogenation of formic acid under ambient conditions. *Chem. Sci.* **2014**, *5* (1), 195. DOI: 10.1039/c3sc52448e.
- Taylor, E. E.; Garman, K.; Stadie, N. P. Atomistic Structures of Zeolite-Templated Carbon. *Chem. Mater.* **2020**, *32* (7), 2742-2752. DOI: 10.1021/acs.chemmater.0c00535.

Nishihara, H.; Simura, T.; Kobayashi, S.; Nomura, K.; Berenguer, R.; Ito, M.; Uchimura M.; Iden, H.; Arihara, K.; Ohma, A.; et al. Oxidation-Resistant and Elastic Mesoporous Carbon with Single-Layer Graphene Walls. *Adv. Funct. Mater.* **2016**, *26* (35), 6418-6427. DOI: 10.1002/adfm.201602459.

Wood, C. D.; Tan, B.; Trewin, A.; Niu, H.; Bradshaw, D.; Rosseinsky, M. J.; Khimyak, Y. Z.; Campbell, N. L.; Kirk, R.; Stöckel, E. Hydrogen Storage in Microporous Hypercrosslinked Organic Polymer Networks. *Chem. Mater.* **2007**, *19* (8), 2034-2048. DOI: 10.1021/cm070356a.

Bowman Jr., R. C. ; Luo C. H.; Ahn, C. H.; Witham, C. K.; Fultz, B. T. The effect of tin on the degradation of LaNi₅-ySny metal hydrides during thermal cycling. *J. Alloys Compd.* **1995**, *217* (2), 185-192. DOI: 10.1016/0925-8388(94)01337-3.

Quine, C. M. REal Adsorption Langmuir Isotherms for Sorption Theory: REALIST. *Github*. <https://github.com/cullenmq/REALIST> (accessed 2025-03-30).

Rowsey, R.; Taylor, E. E.; Irle, S.; Stadie, N. P.; Szilagyi, R. K. Methane Adsorption on Heteroatom-Modified Maquettes of Porous Carbon Surfaces. *J. Phys. Chem. A* **2021**, *125* (28), 6042-6058. DOI: 10.1021/acs.jpca.0c11284.

Nishihara, H.; Fujimoto, H.; Itoi, H.; Nomura, K.; Tanaka, H.; Miyahara, M. T.; Bonnaud, P. A.; Miura, T.; Zuzuki, A.; Miyamoto, N.; et al. Graphene-based ordered framework with a diverse range of carbon polygons formed in zeolite nanochannels. *Carbon* **2018**, *129*, 854-862. DOI: 10.1016/j.carbon.2017.12.055.

Hill, T. L. An Introduction to Statistical Thermodynamics; Addison-Wesley, 1960.

Lemmon, E.; Huber, M.; McLinden, M. *NIST Standard Reference Database 23: Reference Fluid Thermodynamic and Transport Properties-REFPROP, Version 9.1*; National Institute of Standards and Technology, 2013. <https://www.nist.gov/publications/nist-standard-reference-database-23-reference-fluid-thermodynamic-and-transport>.

Hui, W.; Zhou W.; Yildirim T. Methane Sorption in Nanoporous Metal-Organic Frameworks and First Order Phase Transition of Confined Methane. *J. Phys. Chem. C* **2009**, *113* (7), 3029-3035. DOI: 10.1021/jp8103276.

Tsivion E.; Head-Gordon M. Methane Storage: Molecular Mechanisms Underlying Room-Temperature Adsorption in Zn₄O(BDC)₃ (MOF-5). *J. Phys. Chem. C* **2017**, *121* (22), 12091-12100. DOI: 10.1021/acs.jpcc.7b04246.

Quine, C. M. REal Adsorption Langmuir Isotherms for Sorption Theory: REALIST. *Github*. <https://github.com/cullenmq/REALIST> (accessed 2025-03-30).

Taylor, E. E.; Garman, K.; Stadie, N. P. Atomistic Structures of Zeolite-Templated Carbon. *Chem. Mater.* **2020**, *32* (7), 2742-2752. DOI: 10.1021/acs.chemmater.0c00535.